学位論文

Investigation of Quantum Critical Phenomena in Quasi-one-dimensional Magnets by Low-temperature Magnetization and Specific-heat Measurements

(極低温磁化・比熱測定で探る擬一次元磁性体の量子臨界現象)

平成28年12月博士（理学）申請

東京大学大学院理学系研究科
物理学専攻

河野　洋平

Abstract

This dissertation presents an experimental study of quantum critical phenomena at magnetic-field-induced quantum critical points (QCPs) in three (quasi-)one-dimensional (1D) quantum magnets by means of dc magnetization and specific-heat measurements at low temperatures. This dissertation covers three related topics (Chapters 3-5), as well as the background theory behind the experimental results (Chapter 1).

Experimental details used in the present work are described in Chapter 2. Dc magnetization measurements were performed by a Faraday-force technique. After an explanation of the principle of the method, an attempt to improve the sensitivity of the measurements, which was essential for the present work, is described. Specific-heat measurements were performed by a standard quasi-adiabatic heat-pulse method and a relaxation method.

In Chapter 3, the quantum criticality of the magnetization of $Cu(C_4H_4N_2)(NO_3)_2$, or CuPzN for short, near the saturation field $H_s \sim 14\,\mathrm{T}$ is discussed on the basis of the phenomenological theory for 1D free fermion gas. In our previous study, we proved that CuPzN is a practically perfect 1D spin-1/2 Heisenberg antiferromagnet by comparison of our magnetization data at the base temperature of 80 mK with numerical calculations and the phenomenological theory. In this dissertation, we improve the cooling efficiency of the samples in the dilution refrigerator and achieve magnetization measurements at the lowest temperature of 39 mK, which is comparable to the energy scale of the interchain interactions of CuPzN $J' \sim 0.046\,\mathrm{K}$. Much better agreement of the magnetization curve with well-known Bethe ansatz calculations at 0 K is obtained at 39 mK, implying that the interchain interactions are irrelevant near H_s even at this temperature. Applying a universal relation derived from 1D free fermion theory, all the magnetization curve near H_s in the temperature range from 39 mK to 350 mK are well scaled into a single curve. A small deviation of the curve from the theoretical prediction would be attributed to an effect of the repulsive interaction between the fermions. These facts confirm the strong one dimensionality of CuPzN and establishes the universality of the phenomenological theory for 1D free fermion gas near H_s in real magnets.

Chapters 4 and 5 deal with the critical exponent ν of the 3D ordering temperature near the critical field H_c, $T \propto |H_c(T) - H_c(0)|^{\nu}$. The compounds we focused on are spin-1/2 ferromagnetic-leg (FM-leg) ladders, in which leg interactions J_{leg} are ferromagnetic and rung interactions J_{rung} are antiferromagnetic. These new types of ladder compounds have been synthesized recently. We precisely determine the phase boundaries of two spin-1/2 FM-leg ladder compounds, 3-Br-4-F-V [3-(3-bromo-4-fluorophenyl)-1,5-diphenylverdazyl] and 3-I-V [3-(3-iodophenyl)-1,5-diphenylverdazyl], which consist of verdazyl-radical-based molecules, from temperature dependences of the magnetization ($M(T)$) and the specific heat ($C(T)$). The obtained critical exponents ν are discussed in the light of Bose-Einstein condensation

(BEC) universality and quasi-one dimensionality.

3-Br-4-F-V is a strong-rung type ($|J_{\rm rung}/J_{\rm leg}| > 1$) FM-leg ladder and has two field-induced QCPs: the lower critical field $H_{c1} \sim 5\,{\rm T}$, where a spin gap is destroyed, and the saturation field $H_{c2} \sim 9\,{\rm T}$. We demonstrate that a crossover temperature can be determined from the broad peaks and dips in $M(T)$, and it moves in proportion to the magnetic field near the QCPs. This behavior could arise from the quasi-one dimensionality of 3-Br-4-F-V. A systematic change of the 3D ordering temperatures T_c is defined from anomalies in the temperature derivative of $\chi(T) = M(T)/H$, $d\chi(T)/dT$, and $C(T)$. Anomalies in $d(T\chi(T))/dT$ are also discussed to confirm that the difference of the definitions of T_c does not affect the critical exponent ν. The critical exponents ν obtained from a temperature-window technique are in good agreement with the three-dimensional (3D) BEC universality, $\nu = 2/3$, near both of the QCPs in the limit $T \to 0$. No sample dependence is observed for the critical exponents. These results have proven that the verdazyl-radical-based FM-leg ladders are promising as a new model system to study BEC physics.

By contrast, 3-I-V is a strong-leg type ($|J_{\rm rung}/J_{\rm leg}| < 1$) FM-leg ladder antiferromagnet ($T_{\rm N} = 1.4$ K) and has only one field-induced QCP, the saturation field $H_c \sim 5.5\,{\rm T}$. In a preceding study, a nontrivial phase was reported to exist near H_{c2} on the basis of the magnetization ($M(H)$) and the specific heat ($C(H)$) measurements. We firstly reexamine this nontrivial phase near H_{c2}. The second-order field derivative of $M(H)$, d^2M/d^2H, shows a peak indicating the saturation and a shoulder-like anomaly, but $C(H)$ shows only a single sharp peak, different from the previous report. We consider that the broad peak of $C(H)$ in the previous data stemmed not from double phase boundary but from a collapse of the sharp peak due to sample inhomogeneity. The 3D ordering phase boundary is defined from cusp-like anomalies in $\chi(T)$ and peaks in $C(T)$. Anomalies in $d(T\chi(T))/dT$ and $d\chi(T)/dT$ are also discussed to check whether the difference of the definitions of T_c would affect the critical exponent ν. The critical exponent ν obtained from a sliding-window technique shows the nontrivial critical exponent $\nu = 1$, different from the conventional 3D BEC exponent $\nu = 2/3$, as slightly moving away from the QCP. The $\nu = 1$ region is common to all the definitions of T_c. The nontrivial critical exponent could be attributed to the 1D nature of the strong-leg-type ferromagnetic-leg ladder and the frustrations of the intra- and inter-ladder interactions.

The difference of the critical exponents in the FM-leg ladder compounds derived from low dimensionality and frustration would provide novel insight into BEC physics beyond the conventional 3D BEC universality in other quasi-1D quantum magnets.

Contents

Chapter 1

Introduction

1.1 Introduction of Quantum Critical Phenomenon

Quantum criticality has been an attractive concept in condensed matter physics because it provides various types of universal behavior of observables in the vicinity of the phase transitions in quantum magnets. When a phase transition is induced by external parameters, e.g., magnetic field, pressure, etc. at *zero temperature* and is *second order* or continuous, it is called a quantum phase transition (QPT). Then, the point at which QPT occurs is a quantum critical point (QCP) [1]. At a QCP, quantum fluctuation is a main cause of the anomalous behavior of observables such as specific heat, magnetic susceptibility, and correlation function; it is therefore referred to as quantum critical phenomenon. Those observables show, for example, characteristic power laws in the temperature dependences near a QCP.

Quantum fluctuation is brought about by the fact that quantum-mechanical operators are not commutative, being different from classical ones. For example, let us consider the spin state in which nearest-neighbor spins are anti-parallel along z axis as shown in Fig. 1.1. This state, called Néel state, is a classical ground state (GS) of two-dimensional (2D) square-lattice antiferromagnets [2]. When a local Heisenberg (isotropic) Hamiltonian, which describes the antiferromagnetic (AFM) interaction ($J > 0$) between a and b site, is defined as

$$J\boldsymbol{S}_a \cdot \boldsymbol{S}_b = S_a^z S_b^z + \frac{1}{2}\left(S_a^+ S_b^- + S_a^- S_b^+\right), \tag{1.1}$$

operation of $S_a^- S_b^+$ to the GS generates a mixture of the spin state as indicated by blue arrows in Figure 1.1. This means that the Néel state is no longer a true GS because of quantum fluctuation.

1.2 Quantum Critical Phenomenon in One-dimensional Quantum Spin Systems

1.2.1 Spin-1/2 One-dimensional Heisenberg Antiferromagnet

One-dimensional (1D) quantum spin system is one of remarkable examples in which strong quantum fluctuations manifest themselves. As a typical model Hamiltonian, we consider a

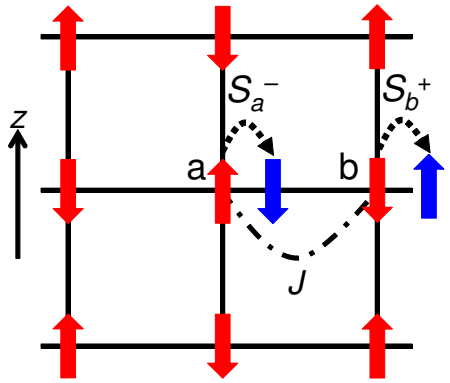

Figure 1.1: Schematic picture of a Néel state on a 2D square-lattice antiferromagnet.

spin-1/2 1D Heisenberg antiferromagnet in a magnetic field

$$H = J\sum_i \boldsymbol{S}_i \cdot \boldsymbol{S}_{i+1} - h\sum_i S_i^z, \tag{1.2}$$

where $J > 0$ is an antiferromagnetic coupling constant, $\boldsymbol{S}_i$ is a spin operator, and h is a normalized magnetic field along z axis, $h = g\mu_{\rm B}H$ (g is a g-factor along z axis, and $\mu_{\rm B}$ is the Bohr magneton) [3]. Applying the Jordan-Wigner transformation

$$S_i^+ \rightarrow c_i^\dagger e^{i\pi\sum_{j=-\infty}^{i-1} c_j^\dagger c_j} \tag{1.3}$$
$$S_i^z = c_i^\dagger c_i - 1/2 \tag{1.4}$$

and a canonical transformation

$$c_i \rightarrow (-1)^i c_i \tag{1.5}$$

to the Hamiltonian (1.2), it can be rewritten as

$$H = -\frac{J}{2}\sum_i [c_{i+1}^\dagger c_i + \text{h.c.}] + J\sum_i (c_{i+1}^\dagger c_{i+1} - \frac{1}{2})(c_i^\dagger c_i - \frac{1}{2}) - h\sum_i (c_i^\dagger c_i - \frac{1}{2}), \tag{1.6}$$

where $c_i^\dagger$ and c_i are creation and annihilation operators of fermion, respectively. Eq. (1.6) means that the spin-1/2 1D Heisenberg antiferromagnet can be described as spinless fermions with a repulsive interaction J. In this picture, the magnetic field h acts as a chemical potential, and the magnetization $m = \langle S_i^z \rangle$ is the particle number of fermions $\langle n_i \rangle = \langle c_i^\dagger c_i \rangle$.

1.2.2 Tomonaga-Luttinger Liquid

Generally speaking, quantum many-body problem is difficult to be solved, but 1D systems are known to be exactly solved in many cases using so-called Bethe ansatz [4–7]. In the case of Eq. (1.6), the GS has no degeneracy and no magnetic ordering, known as a Tomonaga-Luttinger liquid (TLL) [3, 8, 9]. A spin correlation function of the GS is described as

$$\langle S^\alpha(r) S^\alpha(0) \rangle \rightarrow (-1)^r \frac{1}{r} \log^{1/2}(r) \quad (r \rightarrow \infty,\ \alpha = x,\ y,\ z), \tag{1.7}$$

that is, it indicates a power-law decay and a logarithmic dependence for the large distance r. This implies that the GS by itself is a quantum critical state. An elementary excitation from the GS is called spinon, and the excitation in the 1D case is always a pair of spinons and non-local. Therefore, it forms a continuous spectrum as is shown in Fig. 1.2 [10]

$$v_s \sin q \leq \omega \leq 2v_s \sin \frac{q}{2}, \tag{1.8}$$

where $v_s = \pi J/2$ is a spinon velocity. These properties of the TLL reflects the strong quantum effect of the 1D quantum spin system, and TLL can be seen in many kinds of 1D systems [2, 3].

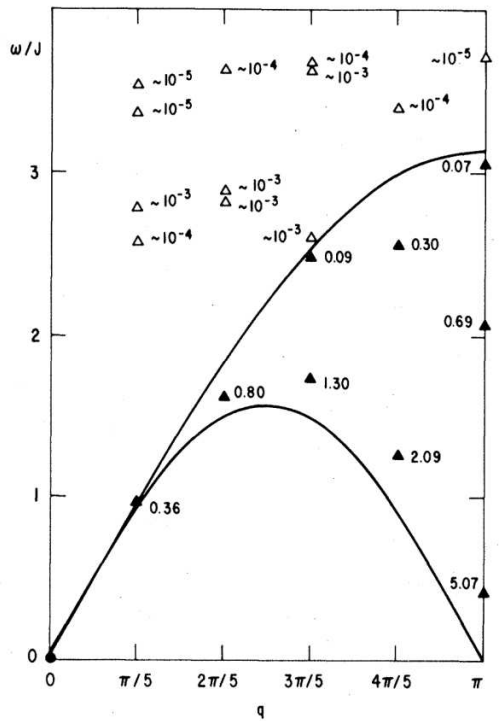

Figure 1.2: Two spinon continuum (the region between two solid lines). Closed symbols mean singlet ground states, and open symbols mean triplet excitations calculated on a system size $N = 10$ [10]

1.2.3 Field-induced Quantum Phase Transition in a Spin-1/2 1D Heisenberg Antiferromagnet

In a finite magnetic field, the GS of the Hamiltonian (1.2) remains to be a TLL until the saturation field $H_s = 2J/g\mu_{\rm B}$ [3, 9]. Above H_s, all spins are polarized along the magnetic field, i.e., the GS is a field-induced ferromagnetic state. When the field-induced ferromagnetic state is a vacuum, an elementary excitation slightly below H_s ($h \lesssim h_s$) is considered as a $S_z = -1$ magnon as shown in Fig. 1.3.

This magnon is a so-called hard-core boson, only one particle of which can exist on the same site. In the vicinity of H_s, dilute hard-core bosons can be mapped onto free fermion gas with a chemical potential $\mu = h_s - h$ [11, 12]. Using Fermi distribution function $f(x) = 1/[1 + e^{\beta(x-\mu)}]$ and assuming the dispersion $\epsilon \sim \hbar^2 k^2/2m$, the magnetization M near H_s can thus be described as

$$\frac{M}{L} = \frac{M_s}{L} + \sqrt{\frac{2m}{\pi^2\hbar^2\beta}} \int_0^\infty \frac{dt}{e^{t^2-\beta(h_s-h)}+1}, \tag{1.9}$$

where L is a system size, $M_s = L/2$ is the saturation magnetization, m is an effective mass of the magnons, and $\beta = 1/k_{\mathrm{B}}T$ [13, 14]. Eq. (1.9) implies a power-law of the temperature dependence of the magnetization $M \sim T^{1/2}$ at $h = h_s$. In this point of view, $H = H_s$ can be regarded as a field-induced QCP in a spin-1/2 1D Heisenberg antiferromagnet.

In our previous paper [15], we have reported that temperature dependence of the magnetization at the saturation field H_s ($\sim$14 T) on $Cu(C_4H_4N_2)(NO_3)_2$, or CuPzN for short, is in excellent accordance with Eq. (1.9) down to the lowest temperature of 80 mK. Then we claimed that CuPzN is a practically perfect one-dimensional spin-1/2 Heisenberg antiferromagnet.

In this dissertation, we perform the magnetization measurements of CuPzN at the lowest temperature of 39 mK as described in Chapter 3. The temperature is comparable to the energy scale of the interchain interactions $J' \sim 0.046$ K, estimated by the zero-field muon-spin-relaxation experiment [16], so that an effect of J' near H_s can be discussed. We also discuss scaling behavior of the magnetization curve of CuPzN near H_s at several temperatures, which is derived from Eq. (1.9).

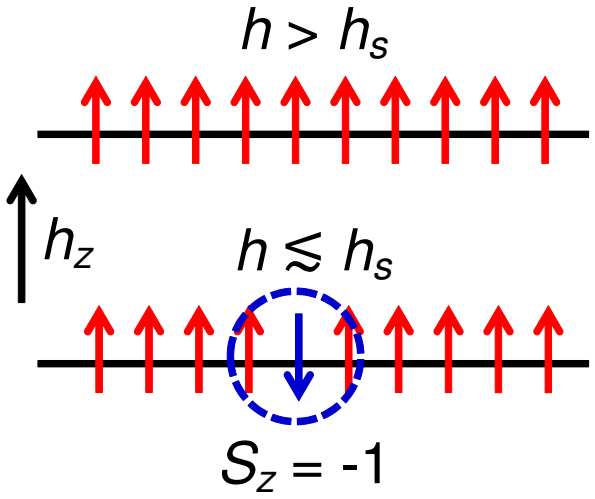

Figure 1.3: Magnon excitation from the field-induced ferromagnetic state.

1.3 Bose-Einstein Condensation in Quasi-1D Quantum Magnets

1.3.1 Correspondence of Quantum Spins to Bosons in Higher Dimension

In a real magnet, spin couplings are more or less three dimensional (3D). Unlike the case of 1D, quantum spins in 3D cannot necessarily be written by fermions with the Jordan-Wigner transformation since Eq. (1.3) is non-local, i.e., it depends on the path of spin sites. In 1956, Matsubara and Matsuda [17] introduced a transformation between $S = 1/2$ spins and hard-core bosons

$$S_i^+ = b_i^\dagger,\ S_i^- = b_i,\ S_i^z = b_i^\dagger b_i - 1/2, \tag{1.10}$$

where $b_i^\dagger$ and b_i, respectively, are creation and annihilation operators of boson (Matsubara-Matsuda transformation), in order to support Bose-Einstein condensation (BEC) theories of liquid ^{4}He. The Matsubara-Matsuda transformation (1.10) is local, so that it can be applied to many kinds of quantum spin systems even in higher dimension. This theory has then provided a way to understand a field-induced QPT of quantum magnets in the light of BEC of such bosons.

1.3.2 General Properties of a BEC QCP in Quantum Magnets

For the realization of a BEC in quantum magnets—it is often called as "a BEC of magnons", spin systems are needed to consist of two-level states. Uniaxial [U(1)] symmetry of the spin Hamiltonian is also required in order to satisfy a number conservation of bosons, i.e., the longitudinal magnetization $M_z = \langle S_i^z \rangle$ should commute with the spin Hamiltonian [18, 19]. A promising realization of this situation is a weakly-coupled spin-1/2 dimer system [18–20]. Spin-1/2 dimer is an antiferromagnetically coupled pair of spins, and the ground state is a spin singlet $|s\rangle = (|\uparrow\downarrow\rangle - |\downarrow\uparrow\rangle)/\sqrt{2}$ with a zero-field spin gap. In a magnetic field, spin-triplet states of each dimer are split by the Zeeman effect as is shown in Fig. 1.4. The lowest branch $|t^+\rangle$ degenerates into the spin singlet state at the critical field $h = h_c$, which depends on the antiferromagnetic coupling, and then the spin gap is destroyed. At $h \gtrsim h_c$, the low-energy excitation in the two-level spin states $|s\rangle$ and $|t^+\rangle$ is a $S_z = 1$ magnon, which can be considered as a hard-core boson introduced in Eq. (1.10). In a similar manner, many of spin systems with two-level spin states are associated with hard-core bosons.

Under these conditions, a spontaneous breaking of the U(1) symmetry at a field-induced QCP becomes a BEC QCP. Generally, the BEC QCP can be observed at a QPT from a spin gapped or saturated state to a 3D XY-like AFM ordering state [18]. Then, the longitudinal magnetization $\langle S_i^z \rangle$ and the ordered moment $\langle m_x \pm i m_y \rangle$ corresponds to a total number of bosons and condensed bosons, respectively, and can be controlled by the magnetic field H that acts as a chemical potential μ. At the 3D BEC QCP, the phase boundary $H_c(T)$ in the limit of zero temperature has been predicted to show the power-law dependence

$$T \propto |H_{\rm c}(T) - H_{\rm c}(0)|^\nu\,, \tag{1.11}$$

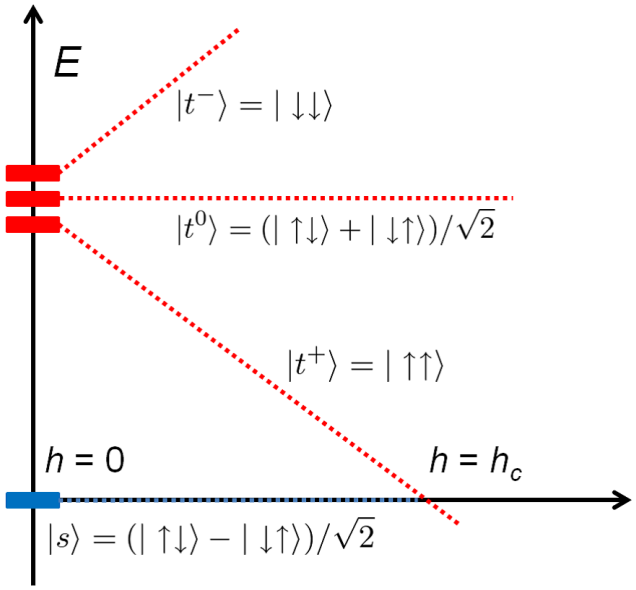

Figure 1.4: Magnetic-field dependence of the energy of spin singlet and triplet states on a spin-1/2 dimer.

where $H_c(0) = H_c$ is a critical magnetic field and $\nu = 2/3$ is a critical exponent at three dimension [21–24].

Of course there always exist U(1) symmetry-breaking interactions such as Dzyaloshinskii-Moriya interactions [25] in a real magnet, so that the concept of a BEC of magnons is an approximation. However, as reviewed by Zapf *et al.* [18], critical properties of the field-induced QCPs in a lot of real quantum magnets can be understood by the 3D BEC universality because such interactions in many cases become relevant only at very low temperatures. The spin-1/2 coupled dimer compound $TlCuCl_3$ has been one of the most frequently referred materials in the light of the 3D BEC universality [21, 26, 27]. A 3D ordering phase boundary near the lower critical field H_{c1} was determined from magnetization measurements as shown in Fig. 1.5(a), and it has been claimed that the critical exponent ϕ (ϕ corresponds to $1/\nu$) approaches the value $\phi = 3/2$ as reducing the maximum temperature of the power-law fitting range to $\sim$ 2 K (Fig. 1.5(b)) [26, 27]. The spin-1/2 coupled dimer $BaCuSi_2O_6$ is also a remarkable example for the 3D BEC universality [28, 29]. A temperature-window technique (detail of this technique will be described in Chapter 4, Section 4.3.4) was applied to a H-T phase diagram near H_{c1} determined from several experiments (Fig. 1.6(a)). The obtained critical exponent ν approaches the value $\nu = 2/3$ as reducing the maximum temperature of the power-law fitting range to 0.61 K, supported by quantum Monte-Calro simulations (Fig. 1.6(a)) [28]. As indicated by these examples, the temperature range for the power-law fitting is important to obtain a reasonable critical exponent, which has also been predicted by the numerical simulations for 3D BEC in quantum magnets [22, 23].

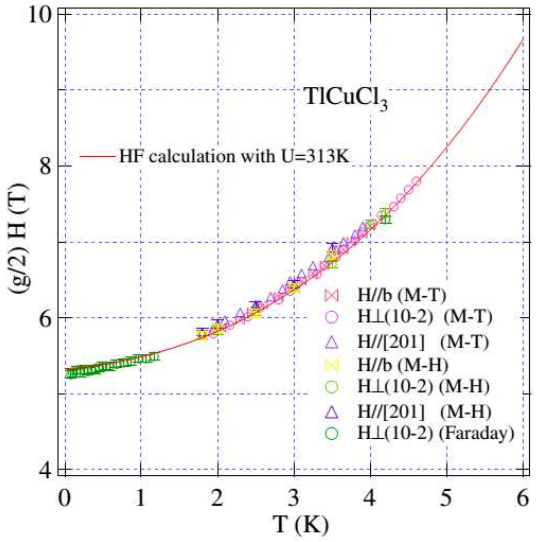

(a) H-T phase diagram of $TlCuCl_3$ determined from several magnetization measurements. Solid curve shows a result of Hartree-Fock calculation.

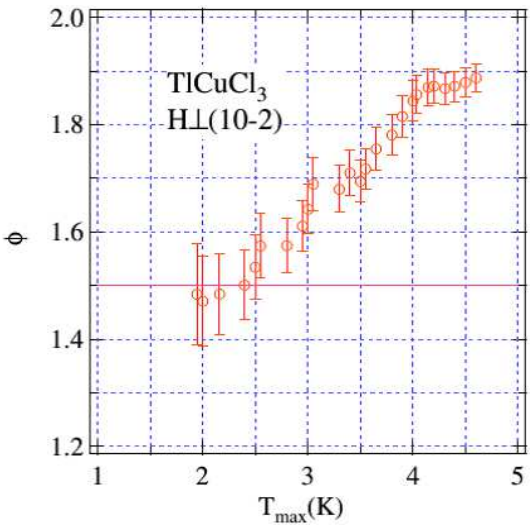

(b) The critical exponent ϕ obtained from the fitting of the power-law function $|H_{c1}(T) - H_{c1}(0)| \propto T^{\phi}$ with the phase boundary in Fig. 1.5(a). The fitting has been performed in the temperature range between 77 mK and $T_{\max}$, with reducing $T_{\max}$.

Figure 1.5: Quantum criticality of the H-T phase diagram near the lower critical field H_{c1} in the spin-1/2 coupled dimer $TlCuCl_3$ [27].

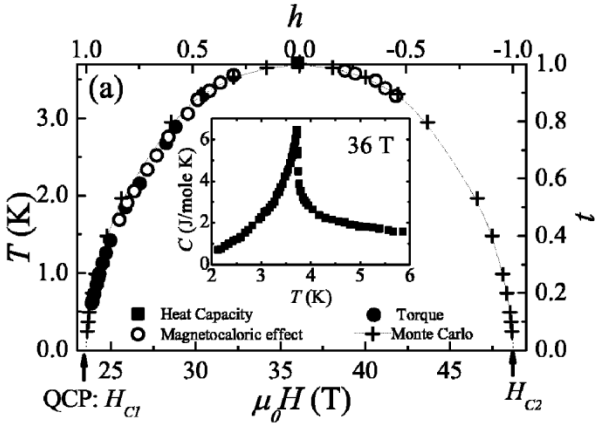

(a) H-T phase diagram of $BaCuSi_2O_6$ determined from several measurements and quantum Monte-Calro simulations.

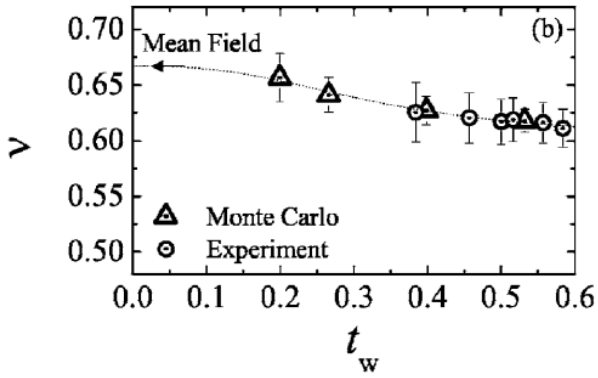

(b) The critical exponent ν obtained from the temperature-window technique for power-law fitting with the phase boundary near H_{c1} in Fig. 1.6(a). ν is the same exponent as defined in Eq. (1.11). $t_{\rm w}$ is the maximum temperature of the fitting range scaled by 3.7 K.

Figure 1.6: Quantum criticality of the H-T phase diagram near the lower critical field H_{c1} in the spin-1/2 coupled dimer $BaCuSi_2O_6$ [28].

1.3.3 Effect of Low Dimensionality and Frustration beyond the 3D BEC Universality

To investigate novel BEC physics beyond the conventional 3D BEC universality in a real magnet, the effects of low dimensionality as well as a frustration in spin couplings have attracted much attention. For example, a "dimensional reduction" of the critical exponent ν has been observed on the spin-1/2 coupled dimer $BaCuSi_2O_6$; there exists a crossover from $\nu = 2/3$ to 1 as the lower QCP, $H_{c1}(0)$, is approached [29]. As a possible cause of the crossover, it has been proposed that a geometrical frustration cancels out the inter-layer AFM interactions between the square-lattice planes consisting of spin dimers, so that the system effectively becomes quasi-two dimensional near the QCP [29–32]. Another interesting example, which is related to the materials treated in this dissertation, is the theoretical study for quasi-one-dimensional ferromagnets with weak AFM couplings; a crossover of the critical exponent ν from $\nu = 2/3$ to 1 is predicted to occur as *moving away* from the saturation [33], being the opposite to the above example. There are several other examples in which the deviation of the critical exponent from the conventional 3D BEC universality could be attributed to low dimensionality and frustration [34–36].

1.3.4 Field-induced QCPs in a Spin-1/2 Two-leg Ladder

Among quasi-low-dimensional quantum magnets, we now focus on a spin-1/2 two-leg ladder as a quasi-1D magnet. The Hamiltonian of the system, in the simplest form, can be expressed as

$$\begin{aligned} \mathcal{H} &= J_{\rm leg} \sum_{i,\alpha} \boldsymbol{S_{i,\alpha}} \cdot \boldsymbol{S_{i+1,\alpha}} + J_{\rm rung} \sum_{i} \boldsymbol{S_{i,1}} \cdot \boldsymbol{S_{i,2}} \\ &\quad -g\mu_B H \sum_{i,\alpha} S^z_{i,\alpha}, \end{aligned} \tag{1.12}$$

where $J_{\rm leg}$ is the interaction along each leg ($\alpha = 1, 2$), $J_{\rm rung}$ is the rung interaction between the legs. The most frequently studied case is "AFM-AFM" ($J_{\rm leg}$, $J_{\rm rung} > 0$), to which the compounds $(Cu_7H_{10}N)_2CuBr_2$ (DIMPY) [37, 38] and $(Cu_5H_{12}N)_2CuBr_4$ (BPCB) [39, 40] correspond. In this case, the ground state is a singlet state ($S = 0$), and there always exists a spin gap [41]. With increasing the magnetic field, the lowest branch of triplet states ($S_z = 1$) degenerates into the singlet state at H_{c1}, and $S_z = 1$ bosons (triplons) are excited, analogous to a spin dimer in Fig. 1.4. Consequently, a TLL state (Section 1.2.2) appears in the gapless phase between H_{c1} and H_{c2} due to the one dimensionality [3, 42]. If there exist 3D interactions between the ladders—as usual in real magnets, the triplons can condense into the 3D BEC state [42]. Typical H-T phase diagram of the spin ladder is shown in Fig. 1.7. For example, in DIMPY, the temperature dependence of the magnetization near H_{c1} has shown a broad minimum indicating a crossover to low-temperature TLL region above its 3D ordering temperature [37] (Fig. 1.8(a) and Fig. 1.8(b)). Such minimum in (quasi-)1D gapped spin systems has been predicted theoretically [14, 43]. The 3D ordering temperature of DIMPY has been discussed from a viewpoint of 3D BEC, but only a few data points were compared with the power law $T \propto (H_{\rm c1}(T) - H_{\rm c1}(0))^{2/3}$ [38] (Fig. 1.8(c)).

Typically, a spin ladder compound which has critical fields easily accessible by a static magnetic field has a low 3D ordering temperature less than a hundred millikelvin, e.g.,

BPCB [40], so that it it difficult to extract the critical exponent of the phase boundary. Thus, there could exist few experimental tests for the 3D BEC exponent in spin ladder compounds. The critical exponents of the 3D ordering phase boundary in spin ladder compounds near both of the critical fields, H_{c1} and H_{c2}, have remained to be examined.

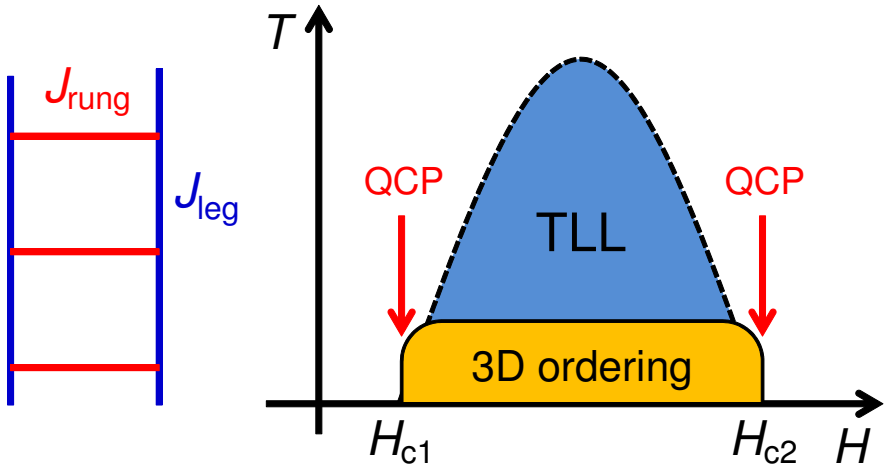

Figure 1.7: Left: schematic picture of a two-leg ladder. Right: schematic picture of typical H-T phase diagram of a spin-1/2 two-leg ladder. Dashed and solid lines denote a crossover and a phase transition, respectively.

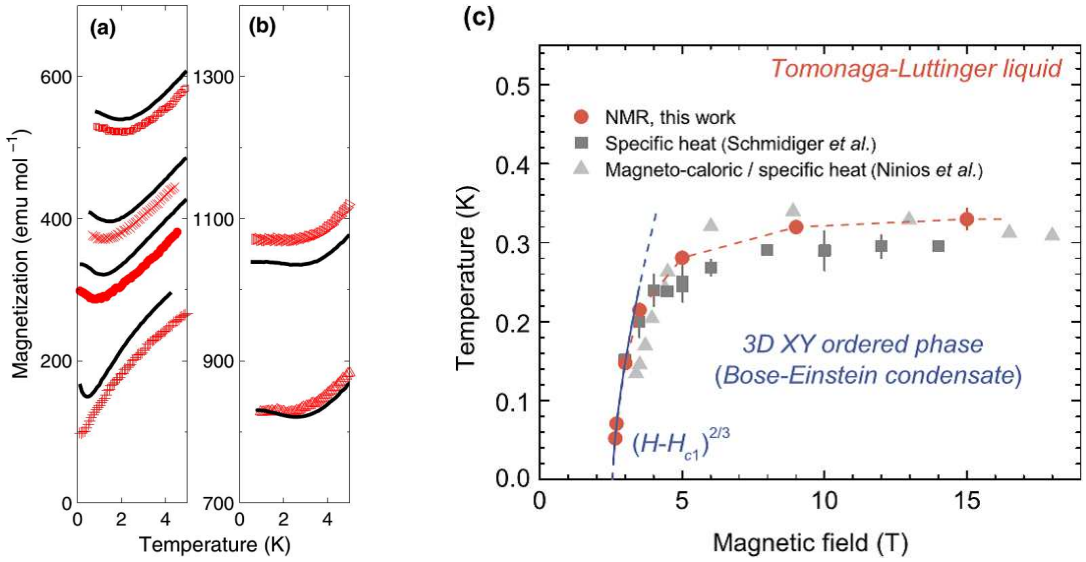

Figure 1.8: Left [(a) and (b)]: temperature dependence of the magnetization of DIMPY [37]. Solid lines are quantum Monte Carlo simulations for an $S = 1/2$ two-leg ladder. (a) 3 T, 4 T, 4.5 T, and 5.5 T, (b) 7.5 T and 9 T from bottom to top. Right [(c)]: 3D ordering phase boundary of DIMPY determined from several measurements [38]. Solid line is fitting of the boundary near H_{c1} with the power law $T \propto (H_{c1}(T) - H_{c1}(0))^{2/3}$.

1.3.5 Investigation of BEC Universality in Spin-1/2 Ferromagnetic-leg Ladder Compounds

Recently, spin-1/2 ferromagnetic-leg (FM-leg) ladders ($J_{\rm leg} < 0$, $J_{\rm rung} > 0$) have been synthesized for the first time, using verdazyl radical molecules [44]. A verdazyl radical carries an $S = 1/2$ quantum spin, and spin couplings between molecules are typically isotropic [44]. Theoretically, FM-leg ladders with an isotropic leg interaction have a spin gap, which stems from the rung-singlet state [45–47], and the ground state between H_{c1} and H_{c2} has been predicted to be a TLL [48] as well as the "AFM-AFM" case (Fig. 1.9). A 3D BEC state is thus expected to be induced in the intermediate field range by weak 3D interactions, so that the phase diagram would be similar to Fig. 1.7. An advantage of the FM-leg ladders over the AFM-AFM ones is that they provide more opportunities to access the upper QCP at H_{c2}; because H_{c2} is insensitive to FM interactions [33], the FM-leg case gives smaller H_{c2} when the intraladder couplings are of the same order of magnitude. However, there exist few studies for an effect of weak 3D interactions and the field-induced QCPs in the FM-leg ladders because of a lack of model compounds.

The three FM-leg ladders synthesized to date [44], 3-Cl-4-F-V [3-(3-chloro-4-fluorophenyl)-1,5-diphenylverdazyl] [49], 3-Br-4-F-V [3-(3-bromo-4-fluorophenyl)-1,5-diphenylverdazyl] [50], and 3-I-V [3-(3-iodophenyl)-1,5-diphenylverdazyl] [51], have shown a variety of H-T phase diagrams different from Fig. 1.7. It could be attributed to the differences of intra- and inter-ladder couplings and their frustration, but detailed properties of the ordering phases remain to be clarified.

In this dissertation, we investigate the critical exponent ν of the phase boundaries on two of the FM-leg ladder compounds, 3-Br-4-F-V (Chapter 4) and 3-I-V (Chapter 5). Previous studies for these compounds are described in each chapter. The obtained critical exponents are discussed in the light of BEC universality introduced as above and quasi-one dimensionality.

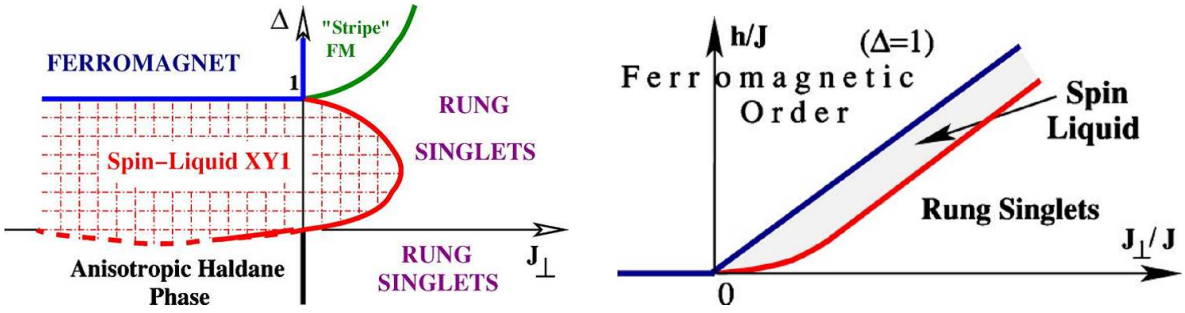

Figure 1.9: Theoretical phase diagrams for a spin-1/2 FM-leg ladder [48]. Left: phase diagram of the ground state with intraleg exchange anisotropy Δ and isotropic rung interaction $J_\perp$. The FM-leg case described in the text corresponds to $\Delta = 1$ and $J_\perp > 0$. Right: phase diagram for a spin-1/2 FM-leg ladder with $\Delta = 1$ and $J_\perp > 0$ in a uniform magnetic field. Solid lines denote second order phase transitions. Spin Liquid indicates TLL region.

Chapter 2

Experimental Methods

2.1 Dc Magnetization Measurements

2.1.1 "Capacitance-Faraday method"

Dc magnetization measurements in this thesis were performed by means of "Capacitance-Faraday method". When a specimen of magnetization $\boldsymbol{M}$ is placed in an inhomogeneous magnetic field $\boldsymbol{H}$, it will experience a force

$$\boldsymbol{F} = (\boldsymbol{M} \cdot \nabla)\boldsymbol{H}. \tag{2.1}$$

We can get the magnetization $\boldsymbol{M}$ of the specimen by measuring this force, and this method has been known as ''Faraday method''. In Sakakibara lab at ISSP, the inhomogeneous magnetic field $\boldsymbol{H}$ is generated by a specially-designed superconducting magnet that has gradient coils in addition to a main solenoid coil, and the force $\boldsymbol{F}$ is detected by a transducer made of a parallel-plate capacitor. Hereafter, we refer to this method as ''capacitance-Faraday method''.

Figure 2.1 shows a schematic picture of the superconducting magnet adopted in the capacitance-Faraday method; the main coil applies a uniform magnetic field to the specimen, and the gradient coils, which consist of two series-oppositely wound coils, generate a field gradient at the sample position. As shown in the right side of Fig. 2.1, the sum of the magnetic field from each of the gradient coils, H_{grad}, is canceled out at the center of the main coil ($z = 0$), but the field gradient $G = d_z H_{grad}|_{z=0}$ is maximized. This configuration enables us to control the main magnetic field H_{main} and its gradient G independently, by using two independent power supplies. When a specimen is placed at the center $z = 0$, it will thus be subject to a force

$$F = MG, \tag{2.2}$$

assuming that the longitudinal magnetization of the specimen $M_z \sim |\boldsymbol{M}| = M$ is sufficiently larger than the transverse component M_{xy} [52].

Figure 2.2 shows the capacitive transducer, which transforms the force F into a variation of the capacitance C. The magnetometer has two electrodes; fixed electrode is isolated from the other part, and a movable electrode is attached at the bottom of a pole brace hung by the crossed wires so that it can move vertically in proportion to an applied force. The device

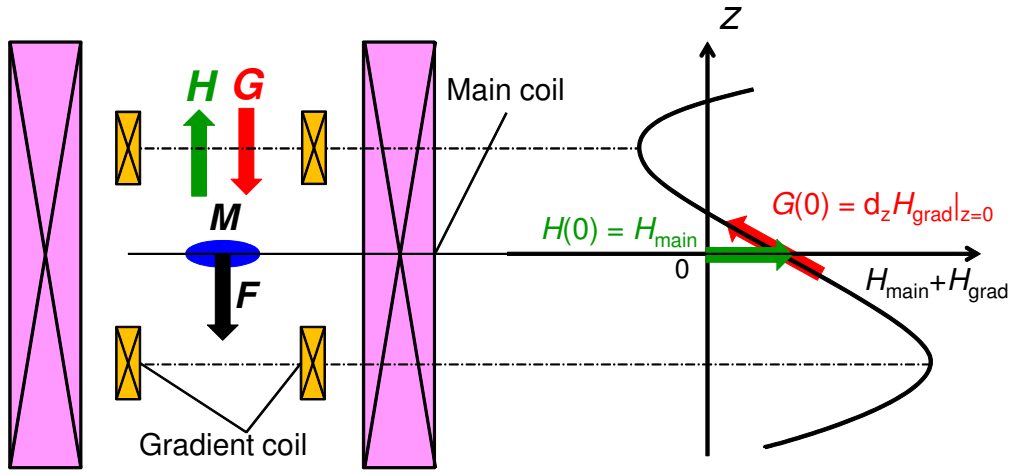

Figure 2.1: Schematic picture of a superconducting magnet used in the capacitance-Faraday method. H_{main} is the magnetic field from the main coil and H_{grad} is that from the gradient coil.

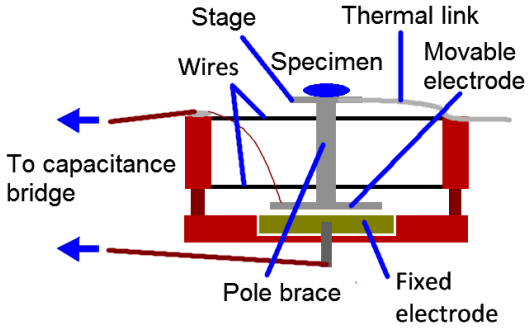

(a) Schematic picture of a capacitive transducer in section.

(b) The capacitive transducer using in magnetization measurements of CuPzN (Chapter 3).

Figure 2.2: The transducer for the capacitance-Faraday method.

thus works as a kind of balance. A specimen is mounted on the top of the pole brace and thermally linked by silver foil with a refrigerator.

Magnetization measurements by the capacitance-Faraday method are done by the following two steps.

(i) Measure the capacitance with no gradient field, $C(G = 0, H, T)$ (Fig. 2.3(a)(i)). It includes the force components other than the magnetization (2.2), such as the gravitational weight and a magnetic torque of the specimen.

(ii) Measure the capacitance with a finite gradient field, $C(G \neq 0, H, T)$ (Fig. 2.3(a)(ii)). The magnetic force (Eq. (2.2)), which is proportional to a change in the capacitor gap d,

can be detected as a change in C. Note that the output also includes the magnetization of the movable electrode.

Using these measured data, a change of the gap Δd, which depends on the magnetization of the specimen M and the movable-electrode background M_{back}, can be expressed as

$$\Delta d = \varepsilon_0 S \left(\frac{1}{C(G=0,H,T)} - \frac{1}{C(G\neq 0,H,T)} \right), \tag{2.3}$$

where ε_0 is the permittivity of vacuum, and S is the area of the movable electrode. When the spring constant of the wires is defined as k, equilibrium of the forces yields

$$(M + M_{\rm back})G = k\Delta d. \tag{2.4}$$

As a result, the magnetization of the specimen can be calculated from

$$M = \frac{\varepsilon_0 k S}{G} \left(\frac{1}{C(G=0,H,T)} - \frac{1}{C(G\neq 0,H,T)} \right) - M_{\rm back}. \tag{2.5}$$

$M_{\rm back}$ can be obtained by an independent blank measurement. The spring constant k, which is of order 1×10^5 dyn/cm, is estimated by a dc bias method; an application of a dc bias voltage of $V_{\rm b} = 40-50$ V induces an electrostatic force $C^2V_{\rm b}^2/(2\epsilon_0 S)$ to the capacitor electrodes, and the gap changes. Further calibration of the magnetization value can be done by comparing the measured data at a certain temperature, e.g., the liquid-helium temperature 4.2 K, with those obtained by a reference magnetometer such as MPMS, a commercial superconducting quantum interference device (SQUID) magnetometer. Fig. 2.3(b) shows examples of the raw capacitance data obtained by this method ($G = 5$ T/m) (Chapter 3).

Compared with the usual dc-magnetization-measurement method using SQUID, this method is more suitable for low-temperature measurements since the capacitance measurement produces no heat. Moreover, the capacitance measurement is unaffected by a magnetic

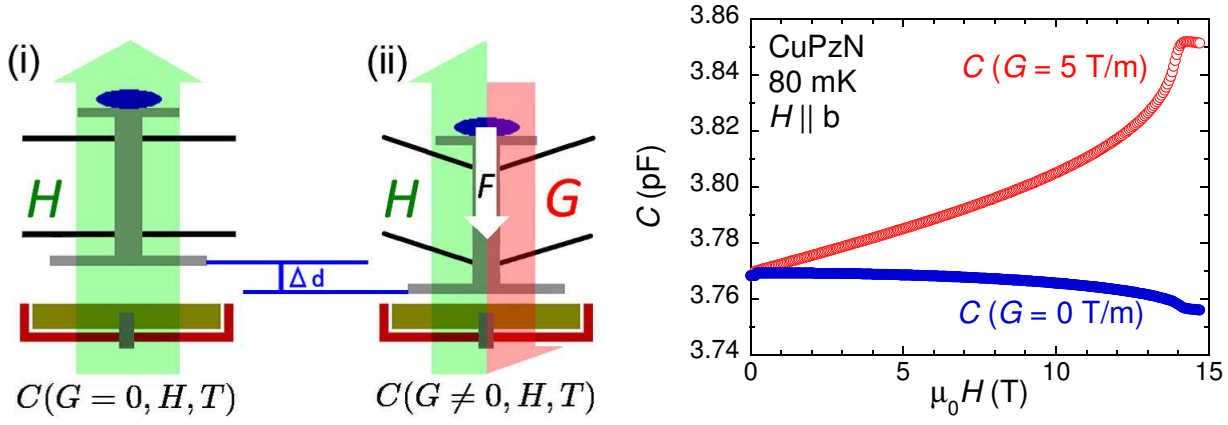

(a) Variation of the gap of electrodes in the capacitance transducer with (i) zero and (ii) a finite gradient of the magnetic field.

(b) Raw capacitance data of CuPzN at 80 mK (Chapter 3).

Figure 2.3: Procedure for the capacitance-Faraday method.

field, so that high-sensitive magnetization measurements can be done even at very high fields. In fact, the $M(H)$ measurements at 39 mK in 14.5 T has been achieved on CuPzN in this dissertation (Chapter 3).

2.1.2 Characteristics of the Capacitance Transducers and Development of a New Capacitor for Quantum Magnets

We compare characteristics of two types of the capacitance transducers used mainly in our laboratory and a new capacitor made for the measurement of quantum magnets with small magnetization values.

Stycast Type

The Stycast-type capacitor has a movable electrode made from a silver-spattered quartz plate (7 mm diameter and 14 mg mass) and a pole brace made from Stycast1266 [53]. These materials are all diamagnetic and almost free from a magnetic impurity. It gives a simple background $M_{\rm back}/H \sim -1 \times 10^{-8}$ emu, almost independent of the temperature as shown in Fig. 2.4(a). The Stycast-type capacitor is thus suitable for measurements of samples with relatively large magnetization values. If one needs to detect a magnetization change of order 10^{-4} emu in a field of 10 T, using this type of a capacitor is inappropriate because the diamagnetic background is 10 times larger.

Aluminum Type

The aluminum-type capacitor has a pole brace made from aluminum doped with a small amount of silicon, instead of Stycast1266 [54]. Since aluminum (Al) is Pauli paramagnetic, it can compensate the diamagnetic component from other stuffs of the magnetometer, to

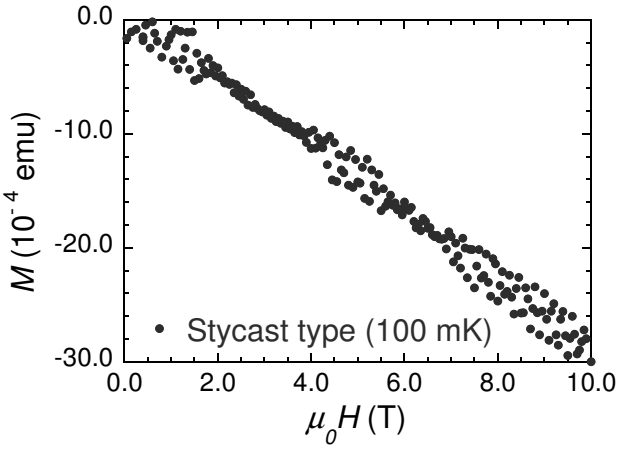

(a) Background $M_{\rm back}$ of the Stycast-type capacitor at 100 mK.

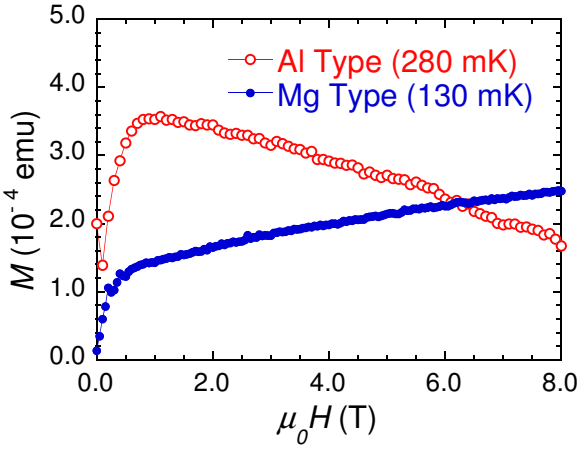

(b) Background $M_{\rm back}$ of the Al-type capacitor at 280 mK (open symbols) and Mg-type capacitor at 130 mK (closed symbols).

Figure 2.4: Magnetic-field dependence of background of the capacitors.

the value as low as $M_{\rm back}/H \sim 1 \times 10^{-9}$ emu. Thus, the Al-type capacitor can be used for a specimen with much smaller magnetization. On the other hand, since ^{27}Al has a relatively large nuclear magnetic moment ($M_{\rm nuc} = +3.6415\mu_N$ per atom [55]) in addition to some amount of magnetic impurities, $M_{\rm back}$ includes a component that is temperature dependent. In addition, Al shows superconductivity below ∼1 K, although its effect is limited only to very low fields below 100 Oe. Typical background $M_{\rm back}$ data are shown in Fig. 2.4(b) and Fig. 2.6.

Magnesium Type —The New Capacitor—

In order to overcome two issues of the Al type—nuclear magnetic moment and superconductivity, I have developed a new capacitance transducer using magnesium (Mg) metal which is also Pauli paramagnetic. ^{25}Mg also has a nuclear magnetic moment ($M_{\rm nuc} = -0.85545\mu_N$ per atom [55]), but its natural abundance ratio is only 10%, much less than that of ^{27}Al (100% [55]). Moreover, Mg does not show superconductivity. These features of Mg can thus solve the problems with Al.

In this new capacitor, Mg of 6N purity is used as a sample stage to compensate diamagnetic components of a movable electrode and a pole brace made from Stycast1266 (Fig. 2.5). In order to suppress unfavorable de Haas-van Alphen oscillations, a small amount (2 %) of Al is melted into Mg ingot (a snapshot of the obtained alloy is shown in the inset of Fig. 2.5(b)). As can be seen in Fig. 2.4(b), this new Mg-type capacitor has smaller magnetic impurity component than the Al type, and its linear component is positive and small at above the fields where the impurity component is saturated. In Fig. 2.6, the temperature dependence of the magnetization in a field of 5 T for the Al type and Mg type are compared. The upturn at low temperatures arising from the nuclear component is suppressed in the background of the Mg type. We confirmed that the Mg-type capacitor actually achieves a substantial improvement of the sensitivity over the previous types of the capacitors.

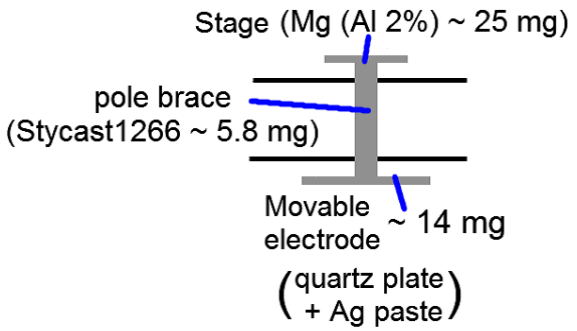

(a) Schematic picture of the movable part of the Mg-type capacitor.

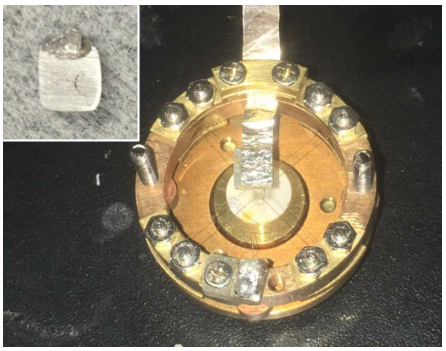

(b) Snapshot of the Mg-type capacitor. Inset: Mg-Al alloy used as the stage of the capacitor.

Figure 2.5: Structure of the Mg-type capacitor.

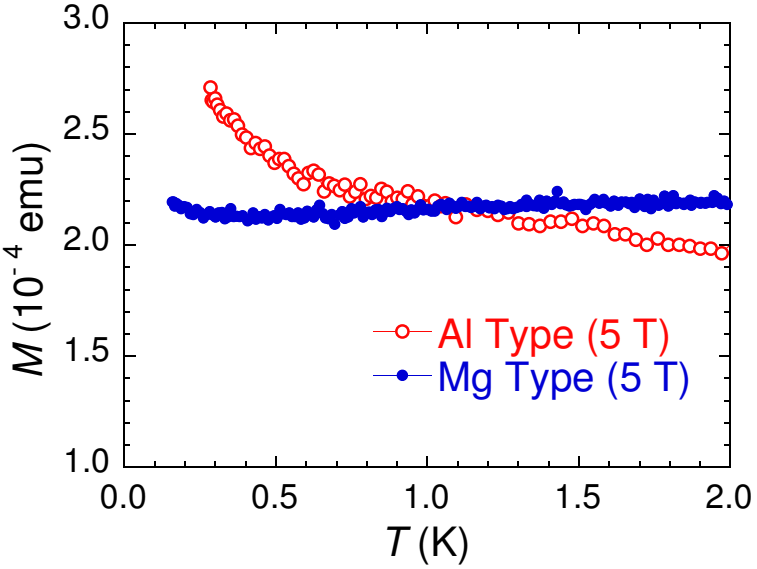

Figure 2.6: Temperature dependence of the background $M_{\rm back}$ of the Al-type capacitor (open symbols) and Mg-type capacitor (closed symbols) at 5 T.

2.2 Specific-heat Measurements

Specific-heat measurements in this thesis were mainly performed by means of the standard quasi-adiabatic heat-pulse method, or by the relaxation method [56]. Fig. 2.7 shows the schematic picture of the specific-heat measurements. Sample system contains a specimen and an addenda that consists of a stage, heater (resistivity: R_h), and thermometer. The system is connected to a thermal bath by a weakly-coupled thermal link (thermal resistivity: $R_{\rm T} = 1/\kappa$). The bath temperature $T = T_0$ is controlled to be constant by a bath heater and a refrigerator. The specific heat C of the sample system contains that from the addenda $C_{\rm add}$, but fortunately in the present measurements, $C_{\rm add}$ is small enough compared with that of the specimen, and did not affect the definitions of transition temperatures discussed in the chapters below.

Specific heat C is defined from an increase of the temperature δT when a heat $\delta' Q$ is quasi-statically given to a system,

$$C = \lim_{\delta T \to 0} \frac{\delta' Q}{\delta T}. \tag{2.6}$$

Therefore, the simplest and precise form of the specific-heat measurement is an adiabatic method in which $C = \Delta Q/\Delta T$ is measured from the increase of the temperature ΔT with application of a heat ΔQ on a thermally-isolated system ($R_{\rm T} = \infty$). However, a perfectly adiabatic condition is generally hard to be achieved in a lab, especially at low temperatures.

Let us consider that the sample system in Fig. 2.7 is weakly coupled with the thermal bath, i.e., the thermal conductivity κ is finite. When $P(t)$ is the heat transferred to the system per unit time, the heat equation can be written as

$$P(t) - \kappa \left[T(t) - T_0 \right] = C \frac{dT}{dt}, \tag{2.7}$$

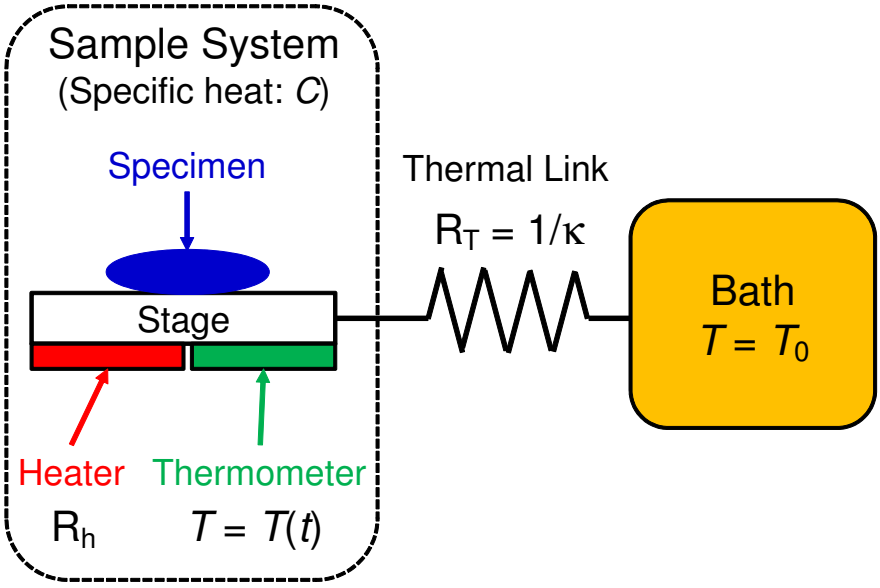

Figure 2.7: Schematic picture of setting of the specific-heat measurements (see text).

where $T(t)$ and T_0 are the sample and the bath temperature, respectively, assuming that C and κ are constants within a narrow temperature window of interest. When $P(t)$ is a constant P_0, it turns out that $dT/dt \to 0$ as $t \to \infty$, so that the heat resistivity $1/\kappa$ can be estimated from

$$\kappa = \frac{P_0}{T(\infty) - T_0}, \tag{2.8}$$

where $T(\infty)$ is the saturation temperature. Considering the initial condition $T(0) = T_0$ and Eq. (2.8), the sample temperature of heating process $T_{\rm heat}(t)$ can be derived from Eq. (2.7) as

$$T_{\rm heat}(t) = T(\infty) - [T(\infty) - T_0] \exp(-t/\tau), \tag{2.9}$$

where the thermal-relaxation time $\tau = C/\kappa$.

A quasi-adiabatic heat-pulse method is performed as described below. When a dc current I_0 is applied to the heater $R_{\rm h}$ in an interval $0 \le t \le t_0$ (heat pulse), the heat $P_0 = I^2 R_{\rm h}$ per unit time is given to the sample system as shown in the lower panel of Fig. 2.8 ($\Delta Q = P_0 t_0$), and the sample temperature increases as illustrated by the solid line in the upper panel of Fig. 2.8. From Eq. (2.9), the increase of the temperature ΔT from $T = T_0$ at $t = t_0$ can be described as

$$\Delta T = [T(\infty) - T_0][1 - \exp(-t_0/\tau)]. \tag{2.10}$$

After $t = t_0$, the sample temperature in the cooling process $T_{\rm cool}(t)$ is

$$T_{\rm cool}(t) = T_0 + \Delta T \exp[-(t - t_0)/\tau], \tag{2.11}$$

which is derived from Eq. (2.7) with the conditions, $P = 0$, $T_{\rm cool}(t_0) = T_0 + \Delta T$, and $T_{\rm cool}(\infty) = T_0$. The integration of both sides of Eq. (2.7) in $0 \le t \le t_0$ yields

$$\int_0^{t_0} \{P(t) - \kappa [T_{\rm heat}(t) - T_0]\}\, dt = C \int_0^{t_0} \frac{dT}{dt} dt, \tag{2.12}$$

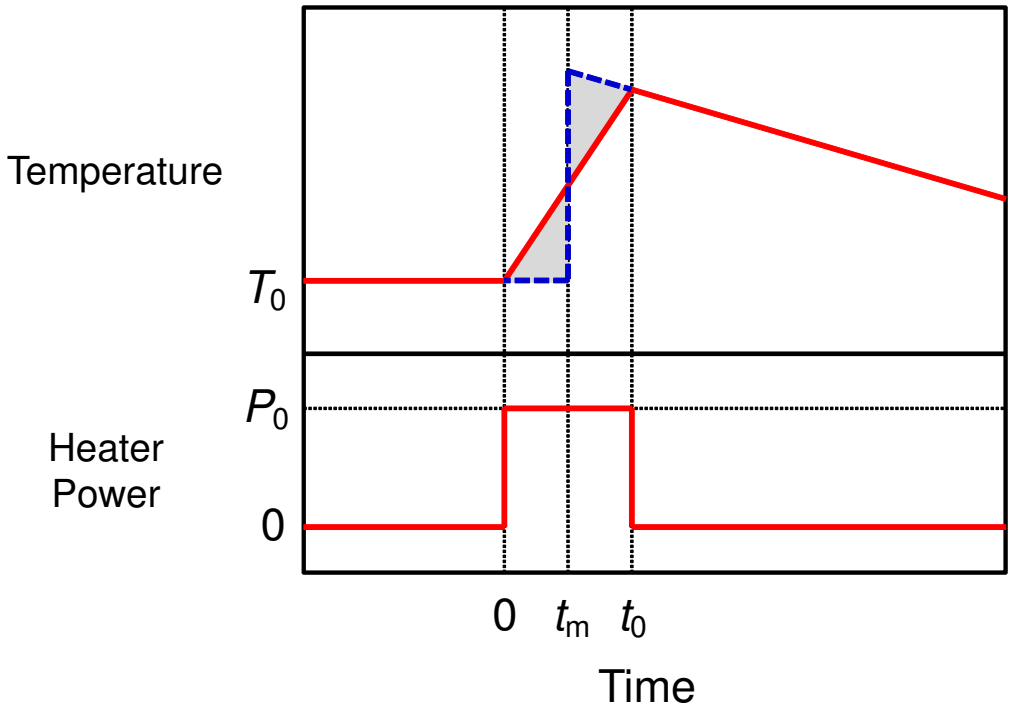

Figure 2.8: Time dependence of the sample temperature $T(t)$ (upper panel) varies with the heat pulse P_0 in $0 \leq t \leq t_0$ from the heater (lower panel) (see text).

so that the specific heat C can be given as

$$C = \frac{P_0 t_0}{\Delta T} \frac{\tau}{t_0} [1 - \exp(-t_0/\tau)]. \tag{2.13}$$

If the thermal isolation of the sample system is not well enough, the simple adiabatic form, $C = P_0 t_0 / \Delta T = \Delta Q / \Delta T$, would thus overestimate the specific heat C. However, in the quasi-adiabatic method, re-definition of ΔT enables us to apply the adiabatic form even to this case.

As one can seen in the left side of Eq. (2.12), C is determined from the area enclosed by $T(t) = T_0$, $T(t) = T_{\rm heat}(t)$, and $t = t_0$ (see Fig. 2.8). Therefore, when the time $t = t_{\rm m}$ is defined as the area enclosed by $T(t) = T_0$, $T(t) = T_{\rm heat}(t)$, and $t = t_m$ is equal to the one enclosed by $T(t) = T_{\rm cool}(t)$, $T(t) = T_{\rm heat}(t)$, and $t = t_m$ (denoted by shadow areas), the instantaneous heating process at $t = t_{\rm m}$ as illustrated by the dashed line yields the same specific heat determined from Eq. (2.13) (solid line). Using $t = t_m$, the specific heat C can be re-defined as

$$C = \frac{P_0 t_0}{\Delta T'} = \frac{P_0 t_0}{\Delta T \exp[-(t_{\rm m} - t_0)/\tau]}, \tag{2.14}$$

where $\Delta T' = T_{\rm cool}(t_{\rm m}) - T_0$. If t_0 is short enough compared with τ, $t_{\rm m}$ can be approximated as $t_{\rm m} \sim t_0/2$. Thus, the quasi-adiabatic method enables us to estimate C precisely from Eq. (2.14) because $\Delta T'$ can be determined from the extrapolation of the cooling curve $T(t) = T_{\rm cool}(t)$ into $t = t_m$.

When C is small and the relaxation time τ becomes as short as a few seconds, the extrapolation of the cooling curve often fails. In this case, a relaxation method is available. Since the relaxation time τ can be estimated from the fittings of heating (cooling) curve with Eq. (2.9) (Eq. (2.11)) and the thermal resistivity $1/\kappa$ can be estimated from Eq. (2.8) in heating process, C can be calculated from the relation $C = \kappa\tau$ in Eq. (2.9). Sensitivity of the relaxation method may be a bit worse than that of the quasi-adiabatic method because it contains the multiple fitting process.

2.3 Thermometer

As thermometers for the magnetization measurements, and for the bath and addenda of the specific-heat measurements, we have used ruthenium-oxide thermometers (Model RO-600, Scientific Instruments, Inc.). We calibrated these sensors by a calibrated ruthenium-oxide thermometer (Type RuOx-B, Entropy, Inc.) from 30 mK to 7 K in zero magnetic field. In a magnetic field, a universal batch-calibration curve for Model RO-600 has been applied, which allows one to calibrate the thermometers with a temperature error of less than $\pm 1.6\%$ from 36 mK to 4.2 K in a field up to 16 T [57].

Chapter 3

Quantum Criticality and Scaling of Magnetization in the Spin-1/2 1D Heisenberg Antiferromagnet CuPzN

3.1 Introduction

3.1.1 Previous Studies of CuPzN

CuPzN has chains of $S = 1/2$ Cu^{2+} which run along the crystallographic $\boldsymbol{a}$ axis [58, 59] as one can see in Fig. 3.1. It has a relatively small intra-chain coupling of $J = 10.3\,\mathrm{K}$ and a corresponding H_s of about 14 T [59]. A zero-field muon-spin-relaxation experiment has detected three-dimensional (3D) magnetic ordering at $T_N = 0.107\,\mathrm{K}$, and the interchain coupling constant J' has been estimated to be 0.046 K [16]. Consistent with such a small J' relative to J, no anomaly indicative of the ordering has been found in the specific heat and the magneti-

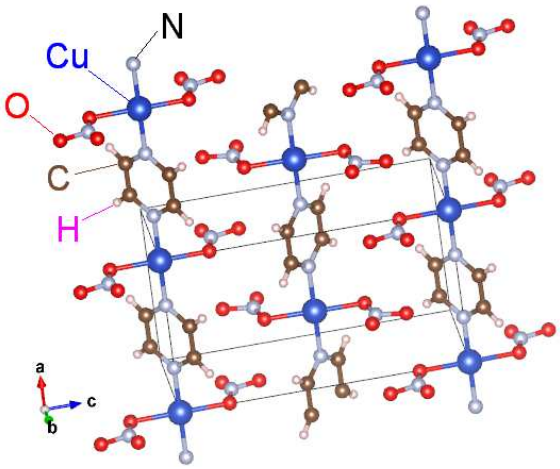

Figure 3.1: Crystal structure of CuPzN. Spin-1/2 chains of Cu^{2+} run along the crystallographic $\boldsymbol{a}$ axis.

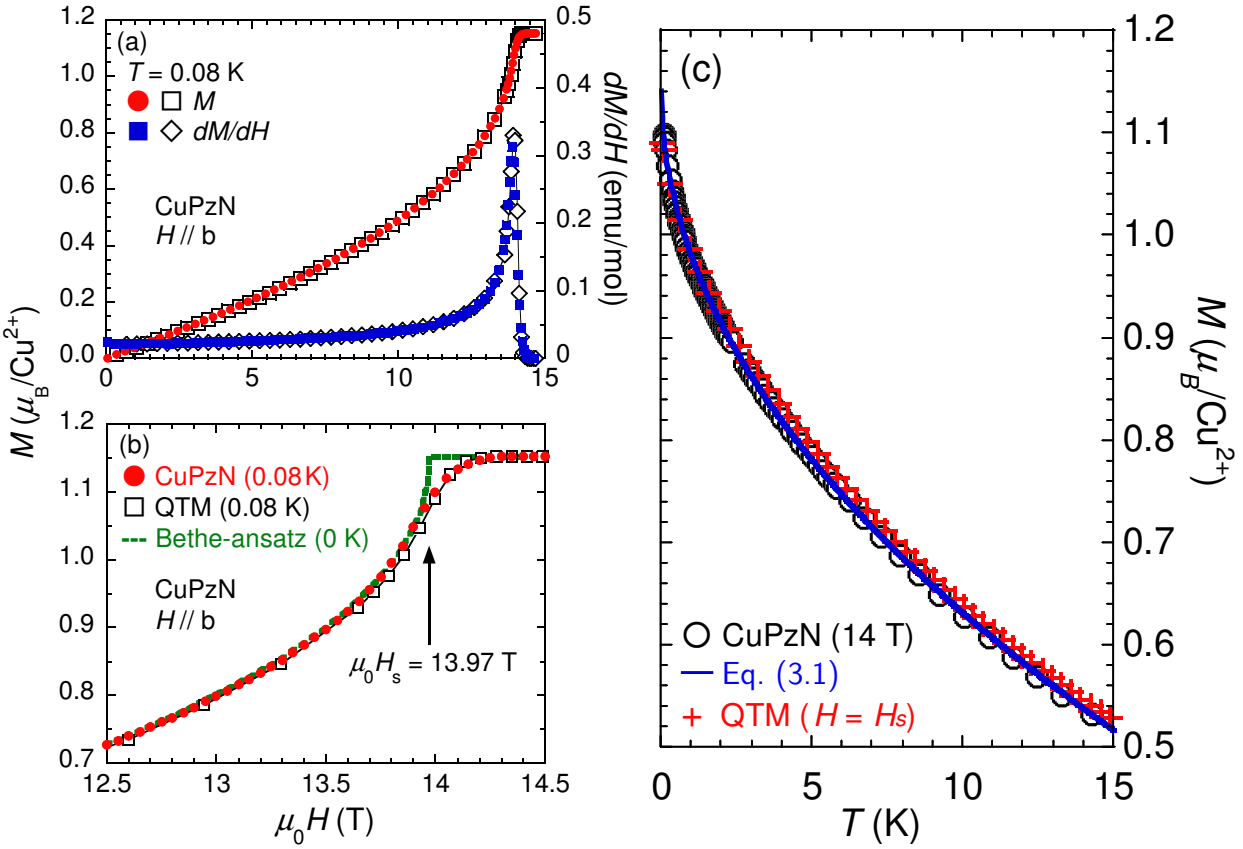

Figure 3.2: Previous results of the magnetization measurements of CuPzN (preprint version of our previous paper [15]). (a) Field dependence of the magnetization M (solid circles) and the differential susceptibility dM/dH (solid squares) at 0.08 K, along with the result of exact QTM calculations for the 1D spin-1/2 HAF at 0.08 K (open symbols). (b) Enlarged plot near $H_s = 13.97$ T. The dashed line is a Bethe-anzatz result for $T = 0$. In both panels, thin solid lines are guides to the eye. (c) Comparison of M at 14 T with the result of a QTM calculation for a 1D spin-1/2 HAF at H_s (crosses). The solid line is the best fit of Eq. (3.1) with the coefficient A as a fitting parameter. Obtained parameter $A = 0.230(1)$ is in good agreement with the given A in the text.

zation down to 0.05 K, well below T_N [60]. Because of these properties, CuPzN has provided an ideal field for experimental tests of a spin-1/2 1D Heisenberg antiferromagnet.

In our previous paper [15], we demonstrated that our magnetization data of CuPzN at the base temperature of 80 mK are well reproduced by the exact calculation of the spin-1/2 1D Heisenberg model employing the quantum transfer-matrix (QTM) method [61, 62], using the parameters, $J = 10.8(1)$ K and $g = 2.30(1)$ (Fig. 3.2(a), (b)). Moreover, we have proved for the first time that the observed quantum critical temperature dependence of the magnetization at the saturation field $H_s = 13.97$ T is actually be described by the phenomenological relation

$$M_s - M = Ag\mu_B\sqrt{k_BT/J}\ (h = h_s), \tag{3.1}$$

where $A = 0.241\,32$ (Fig. 3.2(c)). This expression can be derived from the free fermion

description Eq. (1.9) [14]

$$\frac{M}{L} = \frac{M_s}{L} + \sqrt{\frac{2m}{\pi^2\hbar^2\beta}} \int_0^\infty \frac{dt}{e^{t^2-\beta(h_s-h)}+1} \tag{3.2}$$

(re-shown, see Chapter 1, Section 1.2.3, p. 3), with $m = \hbar^2/J$. These findings demonstrate that CuPzN is a practically perfect one-dimensional spin-1/2 Heisenberg antiferromagnet.

3.1.2 Motivation of the Present Study

It may be surprising that the magnetization of the results of CuPzN follows the 1D theory down to such a low temperature since one expects that the interchain coupling J' would affect the behavior of the magnetization. For example, the modified Bethe-ansatz results incorporating interchain couplings by a mean-field approximation predicts a rounding of the magnetization curve near the saturation field [63]. If it is applied in the case of CuPzN, it could raise the saturation field H_s by about $4J'/(g\mu_B) = 0.12\,\mathrm{T}$ and cause M to become rounded over a certain field interval, of a comparable size, below the raised H_s. In the previous paper, we have attributed the absence of the additional rounding of the magnetization curve to the competition between the antiferromagnetic and ferromagnetic J', and their geometrical frustration, predicted by first-principles calculations of exchange interactions [64].

However, our previous measurements have been performed only at the base temperature of 80 mK, which is a bit higher than the energy scale of the interchain interactions $J' \sim 0.046\,\mathrm{K}$, estimated by the zero-field muon-spin-relaxation experiment [16]. Thus, in this dissertation we plan to examine whether the one dimensionality of CuPzN would persist even at temperatures comparable to J'.

3.2 Experimental

Our present dc magnetization measurements were performed on a part of the single-crystal sample of CuPzN used in the previous measurements (Fig. 3.3), by means of the capacitance-Faraday method with the Stycast-type capacitor. Magnetic fields were applied parallel to the $\boldsymbol{b}$ axis as the same direction with the previous measurements. The magnetization value was calibrated by the previous result of the saturated magnetization, $M_s = 1.15\,\mu_B$ [15].

In order to achieve the temperatures comparable to J' of 0.046 K, we used a ^{3}He-^{4}He dilution refrigerator which has a higher cooling power (kelvinox®100, 100 μW at 100 mK, Oxford Instruments) than the one used in the previous measurements (kelvinox®25, 25 μW at 100 mK, Oxford Instruments). Copper (5N purity, $\phi 0.5\,\mathrm{wire} \times 15$) and silver (4N purity, $\phi 0.3\,\mathrm{wire} \times 15$) wires had firstly been used as thermal link between the mixture pot of the refrigerator and the capacitor. However, as shown in Fig. 3.4, it took about 10^5 seconds (~ 28 hours) to cool down the sample from 0.1 K to 0.05 K at a field of 12.5 T (open symbols). This is not practical for high magnetic-field measurements considering the boiling off of liquid helium used as cryogen.

For improvement of the cooling efficiency, the silver wires were annealed for about 3 hours at $\sim 650\,^\circ\mathrm{C}$ in $\sim 10^{-4}$ mbar air since annealing can generally increase thermal conductivity of metals (see, for example, Ref. 65). In the improved configuration, we used only such annealed

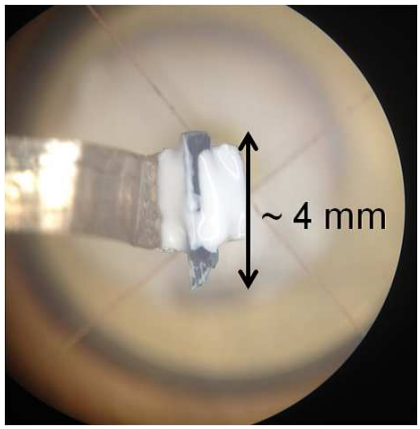

Figure 3.3: Single crystal of CuPzN used in the present measurements. The white paste is a non-magnetic thermal compound used for fixing the sample.

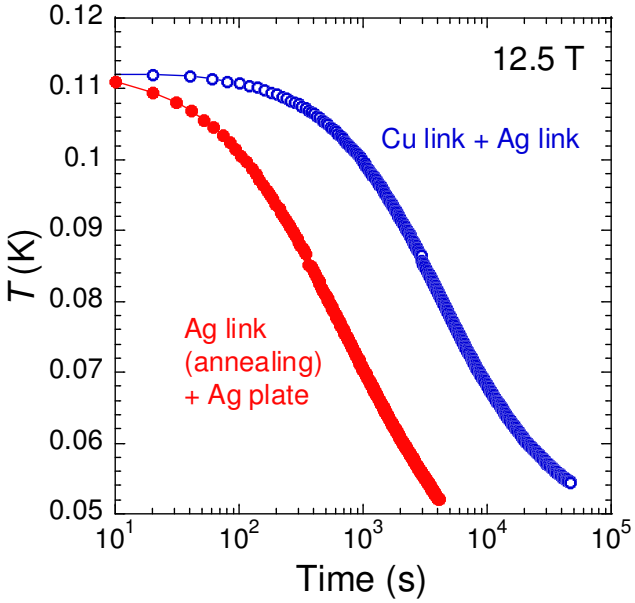

Figure 3.4: Sample cooling process from 0.1 K to 0.05 K at 12.5 T (see text).

silver wires ($\phi 0.3\,\text{wire} \times 30$) as the thermal link and replaced a copper attachment between the thermal link and the magnetometer with a silver one, in order to avoid a relatively large nuclear specific heat of copper in a high magnetic field. Owing to these improvements, we succeeded in reducing the cooling time to less than one tenth of the time before the improvements (Fig. 3.4, closed symbols), and could reach the lowest temperature of 39 mK.

3.3 Results and Discussion

3.3.1 Magnetization Curves and Differential Susceptibility near the Saturation Field

Figure 3.5 shows the magnetization curves near the saturation field $H_s = 13.97\,\text{T}$ at several temperatures between 39 mK and 359 mK, along with the well-known exact Bethe-ansatz curve at $T = 0$ [7] recomputed in our previous paper [15]. In this temperature region, the deviation of the experimental curves from the Bethe-ansatz curve is mainly from the rounding near H_s. At below 80 mK, the base temperature in our previous measurements, the agreement of the present magnetization data with the Bethe-ansatz curve is the better, the lower the temperature is.

This tendency is more obvious in the differential susceptibility dM/dH as shown in Fig. 3.6. The peak height near H_s is increasing with decreasing the temperature. At the lowest temperature, 39 mK, dM/dH is in excellent accordance with the Bethe-ansatz curve at below H_s. These facts imply that the inter-chain interactions are irrelevant even at 39 mK, which is close to the energy scale of the interchain interactions $J' \sim 0.046\,\text{K}$ estimated by the zero-field muon-spin-relaxation experiment [16].

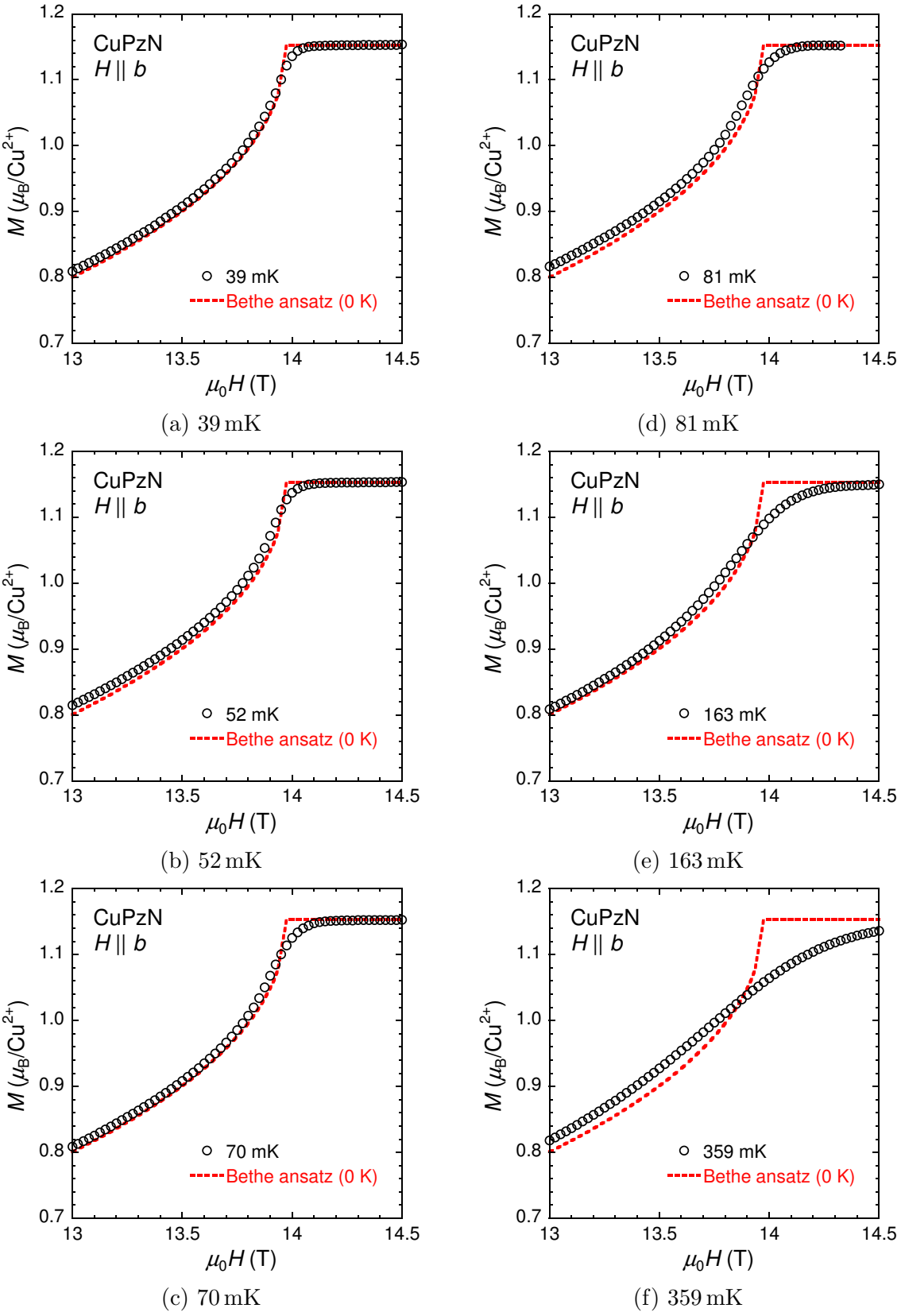

Figure 3.5: Magnetization curves near the saturation field H_s at several temperatures. Dashed line is a Bethe-ansatz result for $T = 0$.

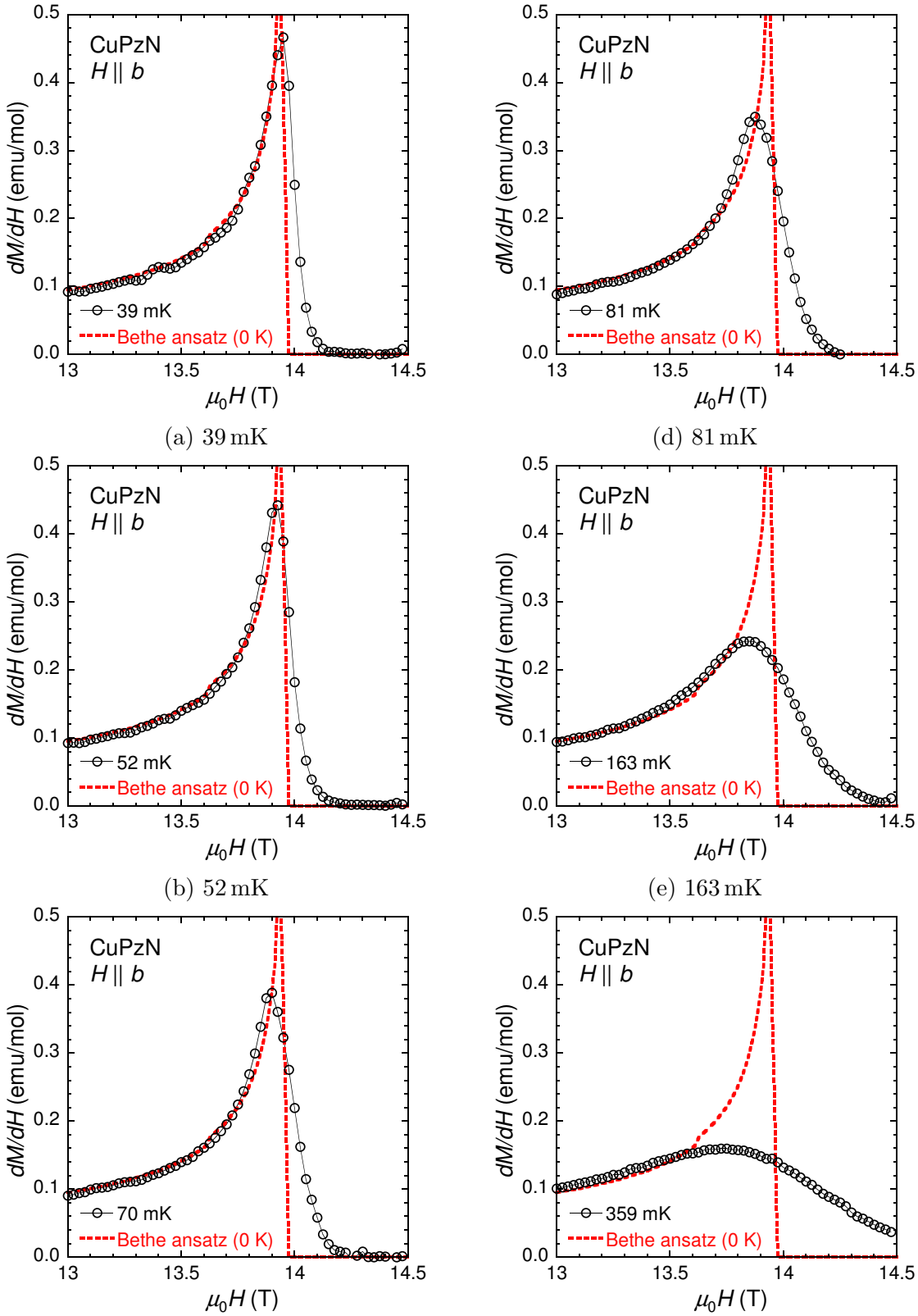

(a) 39 mK (d) 81 mK

(b) 52 mK (e) 163 mK

(c) 70 mK (f) 359 mK

Figure 3.6: Differential susceptibility dM/dH near the saturation field H_s at several temperatures. Solid lines are guide to the eye. Dashed curve is a Bethe-ansatz result for $T = 0$.

3.3.2 Re-examination of the Quantum Criticality at the Saturation Field

In our previous paper [15], the temperature dependence of the magnetization at 14 T was compared with Eq. (3.1). Although the field was a bit higher than the value, $H_s = 13.97$ T, determined from the comparison of the magnetization curve at 80 mK with the QTM calculations, a power-law fit of $(M_s - M)/H \propto T^{\beta}$ with the data yielded the value, $\beta = 0.48(1)$, consistent with Eq. (3.1). In the present study, we performed the same measurements at 13.97 T down to 60 mK as shown in Fig. 3.7 along with the previous data at 14 T. The power-law fit with the present data yields $\beta = 0.4894(2)$, which is in better accordance with Eq. (3.1). This fact supports that the quantum criticality of CuPzN at the saturation field excellently agrees with the 1D theory.

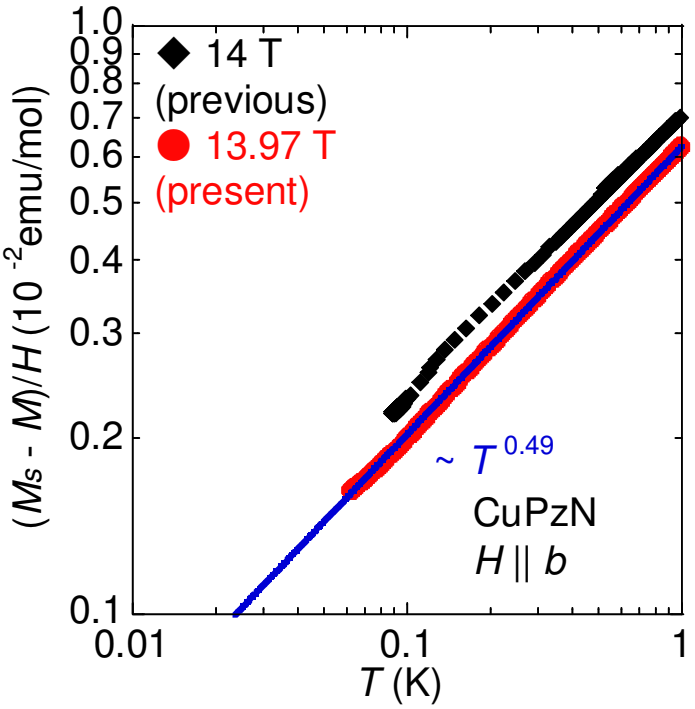

Figure 3.7: Log-log plot of $(M_s - M)/H$ near H_s as a function of temperature below 1 K. Circles are the present data at 13.97 T. Diamonds are the previous data at 14 T, reported in Ref. 15. The best fit of a power law, $(M_s - M)/H \propto T^{\beta}$, to the 13.97 T data yields $\beta = 0.4894(2)$ (solid line).

3.3.3 Scaling of Magnetization Curves near the Saturation Field

The free fermion description of the magnetization Eq. (3.2) can be transformed as

$$1 - (1 - M/M_s)/\sqrt{2k_BT/J} = 1 - 2N(x), \tag{3.3}$$

$$N(x) = \frac{1}{\pi}\int_0^{\infty} \frac{dk}{e^{k^2 - x} + 1}, \tag{3.4}$$

$$x = g\mu_B(H - H_s)/k_BT. \tag{3.5}$$

This equation means that the left side of Eq. (3.3) can be described as a function of x, $f(x) = 1 - 2N(x)$, without adjustable parameters, i.e., magnetization curves in different temperatures and magnetic fields can be scaled into a single curve as a function of x if the 1D free fermion approximation is valid. Analogous scaling has been reported in the magnetization curves of the spin-1/2 antiferromagnetic ladder $(Cu_5H_{12}N)_2CuBr_4$ (BPCB) [39] and the temperature dependence of the magnetization of CuPzN extracted from our previous paper by another group [66]. This scaling would be a criterion of one dimensionality. In the case of CuPzN, we have $M_s = 1.15\,\mu_B$, $H_s = 13.97\,\mathrm{T}$, $J = 10.8\,\mathrm{K}$, and $g = 2.30$.

Figure 3.8(a) shows the left side of Eq. (3.3) calculated from each curve of Fig. 3.5 as a function of $x = g\mu_B(H - H_s)/k_BT$, along with the function $f(x) = 1 - 2N(x)$. All the obtained curves are in good accordance with $f(x)$ near the saturation field ($x = 0$), but the deviation from $f(x)$ increases with decreasing x. A cause of this deviation is probably that the free fermion description would become inappropriate at lower fields because of an effect of the repulsive interaction between the fermions [14]. Nevertheless, all the experimental curves are well scaled even in this parameter range. Indeed, a modification of $N(x)$ to $0.9N(x)$ can reproduce the scaled curves remarkably well (Fig. 3.8(b)). If this modification is attributed to a change of the effective mass m by the effect of the repulsive interaction between the fermions, it corresponds to $m \rightarrow 1.2\,m$. Although theoretical supports are needed for this assumption, this scaling behavior can reinforce the fact that CuPzN is a practically perfect one-dimensional spin-1/2 Heisenberg antiferromagnet and establish the universality of the 1D fermion description Eq. (3.2).

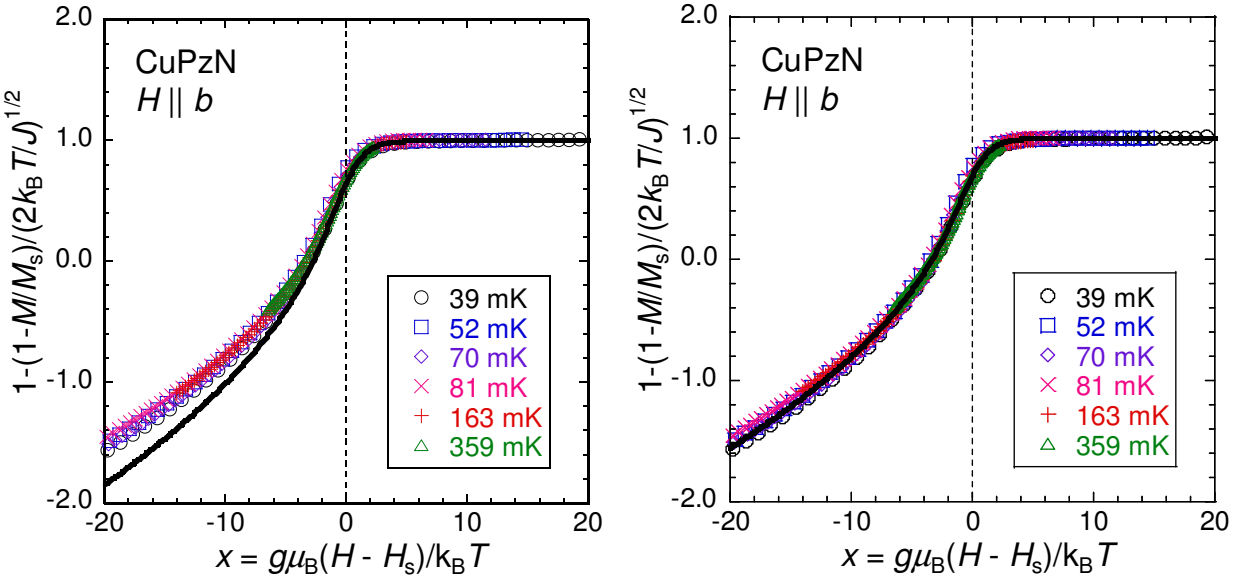

(a) Left side of Eq. (3.3) calculated from each curve of Fig. 3.5 as functions of $x = g\mu_B(H - H_s)/k_BT$. Solid line is a function $f(x) = 1 - 2N(x)$.

(b) The same experimental data in (a) along with the rescaling result of the function $f(x)$ (solid line, see text).

Figure 3.8: Scaling of magnetization curves near the saturation field $H_s = 13.97\,\mathrm{T}$.

3.4 Summary

We performed dc magnetization measurements of CuPzN near $H_s = 13.97\,\mathrm{T}$ down to 39 mK, which is lower than the lowest temperature of 80 mK in our previous measurements and is comparable with the energy scale of the interchain interactions $J' \sim 0.046\,\mathrm{K}$. The agreement of the magnetization curve with the Bethe-ansatz result becomes increasingly better as the temperature decreases, so that no effect of the interchain interaction can be observed even at 39 mK. Moreover, all the magnetization curves near H_s are well scaled by a universal curve derived from the 1D free fermion description of a spin-1/2 1D Heisenberg antiferromagnet near the saturation field. These facts re-emphasize the strong one dimensionality of CuPzN and establish that the 1D free fermion description is applicable to real 1D magnets in rather wide parameter ranges.

Chapter 4

Three-dimensional Bose-Einstein Condensation in the Spin-1/2 Ferromagnetic-leg Ladder 3-Br-4-F-V

4.1 Introduction

4.1.1 Previous Studies of 3-Br-4-F-V

In the molecular-based crystal 3-Br-4-F-V ($C_{20}N_4H_{15}BrF$), each molecule includes a verdazyl radical, which carries an $S = 1/2$ quantum spin (the left of Fig. 4.1). The molecules are stacked along $\boldsymbol{a}$ axis and form a spin ladder (the right of Fig. 4.1) [50]. The *ab initio* MO calculations have revealed that the spin ladder is of FM-leg type ($J_{\rm rung} > 0$, $J_{\rm leg} < 0$). This and the two other verdazyl-radical-based crystals (3-Cl-4-F-V, 3-I-V) are the first experimental realization of the FM-leg ladders [44].

The coupling constants have been estimated to be $J_{\rm rung} = 12.5\,{\rm K}$ and $J_{\rm leg} = -8.3\,{\rm K}$ ($|J_{\rm rung}/J_{\rm leg}| \sim 1.5$) by comparison of the magnetization curves with QMC calculations for an $S = 1/2$ FM-leg ladder [44] (Fig. 4.2(a)). A spin gap exists at below the lower critical field $H_{\rm c1} \sim 5\,{\rm T}$, and the saturation field is $H_{\rm c2} \sim 9\,{\rm T}$. In the magnetic field range between $H_{\rm c1}$ and $H_{\rm c2}$, 3-Br-4-F-V exhibits a 3D ordering due to inter-ladder couplings below $\sim$0.6 K as indicated by the temperature derivative of $\chi = M/H$ (Fig. 4.2(c)) and the magnetic specific heat $C_{\rm mag}$ (Fig. 4.3(a)) [50]. As revealed by nuclear magnetic resonance (NMR) measurements, the 3D ordering phase is incommensurate. On the other hand, the temperature dependence of χ itself shows a broad maximum or minimum (Fig. 4.2(b)), which could be attributed to a crossover to a low-temperature TLL state as described in Chapter 1, Section 1.3.4. However, in reality, most of the anticipated TLL region is replaced by a partial ordering phase as indicated by the specific-heat and NMR measurements [50] (Fig. 4.3(b)).

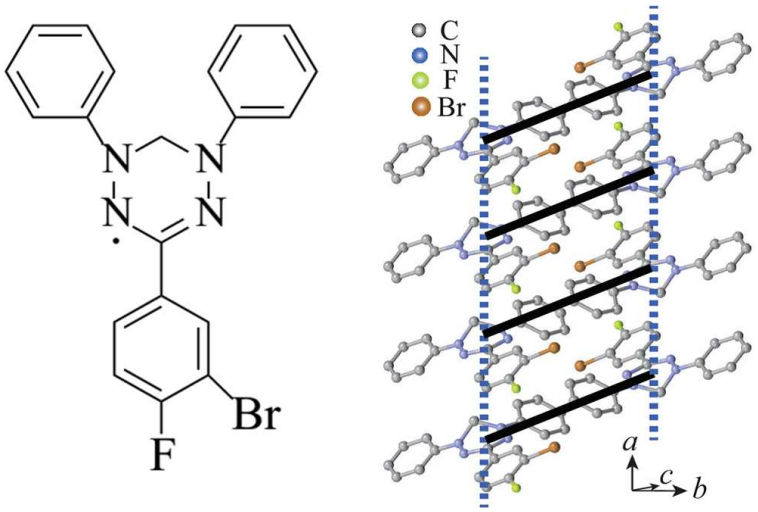

Figure 4.1: Left: structural formula of 3-Br-4-F-V [50]. Right: a part of crystal structures of 3-Br-4-F-V forming a two-leg ladder [50].

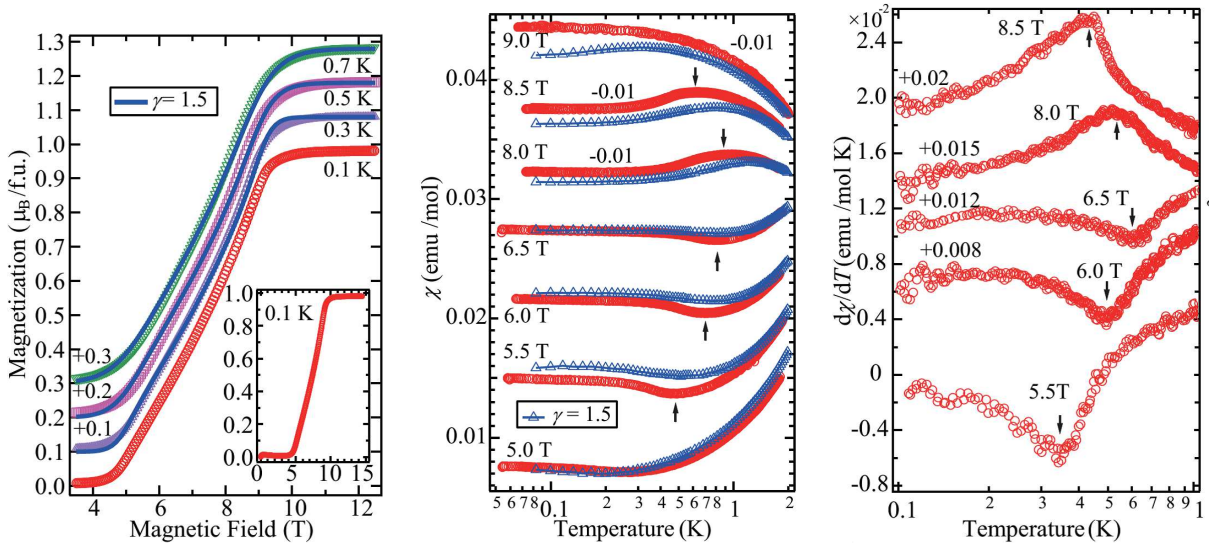

(a) Magnetic-field dependence of the magnetization. Solid lines denote the results of QMC calculations.

(b) Temperature dependence of the magnetic susceptibility $\chi = M/H$. Arrows denote broad dip or peak anomalies in χ. Triangles show the results of QMC calculations.

(c) Temperature derivative of χ. Arrows denote kink anomalies, indicating a 3D ordering.

Figure 4.2: Previous results of the magnetization measurements on 3-Br-4-F-V [50].

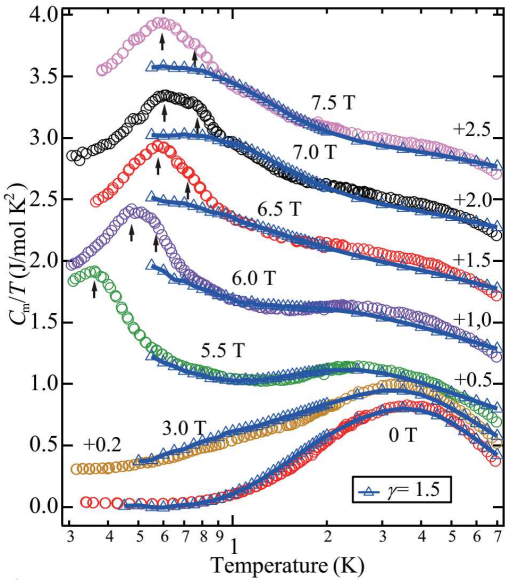

(a) Temperature dependence of the magnetic specific heat C_{mag}. Arrows for higher temperatures in the data from 6.0 T to 7.5 T denote anomalies indicating a partial ordering. The other arrows denote peak anomalies indicating a 3D ordering. Triangles show the results of QMC calculations.

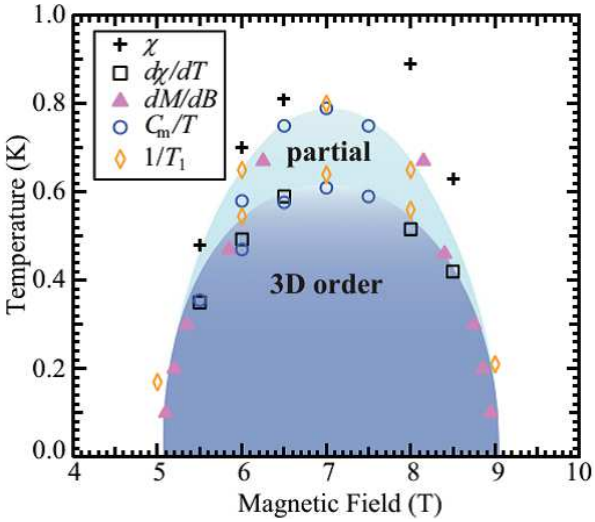

(b) H-T phase diagram of 3-Br-4-F-V. Crosses, squares, and circles correspond to the anomalies defined from the temperature dependence of χ (Fig. 4.2(b)), $d\chi/dT$ (Fig. 4.2(c)), and C_{mag}/T (Fig. 4.3(a)), respectively.

Figure 4.3: Previous results of the specific-heat measurements and phase diagram on 3-Br-4-F-V [50].

4.1.2 Motivation of the Present Study

Although detailed magnetic structures of these exotic ordering phases remain to be clarified, a 3D BEC is expected to be realized in this situation. The 3D ordering phase is indeed dome-like, in close resemblance to the other model compounds such as $BaCuSi_2O_6$ [28, 29] (see Fig. 1.6(a), p. 7). Moreover, spin couplings between verdazyl radical molecules are essentially isotropic [44], in favor of U(1) symmetry of their spin Hamiltonian, the condition of which is necessary for BEC in quantum magnets as described in Chapter 1, Section 1.3.2 (p. 5). Thus, we have expected that 3-Br-4-F-V would be a new model system for BEC in quantum magnets as a FM-leg ladder.

4.2 Experimental

Single-crystal samples of 3-Br-4-F-V were prepared in Hosokoshi lab at Osaka Prefecture University as reported in Ref. 44. Dc magnetization measurements were performed by means of the capacitance-Faraday method with the Al-type and Mg-type capacitors (Chapter 2) on a 7.42 mg sample (sample#1, Fig. 4.4(a)). Specific-heat measurements were carried out by

the standard quasi-adiabatic heat-pulse and relaxation methods (Chapter 2) on a 1.46 mg sample taken from the same batch (sample#2, Fig. 4.4(b)). In both measurements, a ^{3}He-^{4}He dilution refrigerator was used in the temperature ranges $0.1\,\mathrm{K} \leq T \leq 1\,\mathrm{K}$. In all the measurements, magnetic fields up to 9 T were applied perpendicular to the $\boldsymbol{a}$ axis (perpendicular to the leg direction).

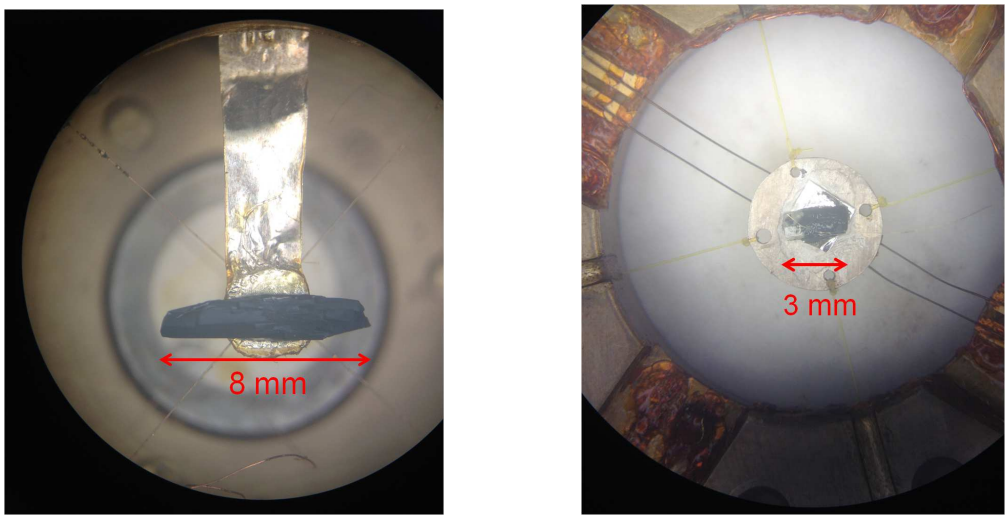

(a) Single-crystal sample used for dc magnetization measurements (7.42 mg, sample#1).

(b) Single-crystal sample used for specific-heat measurements (1.46 mg, sample#2).

Figure 4.4: Single-crystal samples of 3-Br-4-F-V.

4.3 Results and Discussion

4.3.1 Dc Magnetization Measurements

Figure 4.5(a) and Figure 4.6(a) show the temperature dependence of the magnetic susceptibility $\chi = M/H$ in several magnetic fields near the critical fields H_{c1} and H_{c2} (see also Appendices, Section A.1, p. 66). There exists a nontrivial minimum (maximum) in Fig. 4.5(a) (Fig. 4.6(a)), and the temperature at which the extremum appears ($T = T_{ex}$) increases (decreases) with increasing the magnetic field. Analogous behavior in χ has been observed in typical spin-1/2 two-leg spin ladders such as DIMPY [37]. Theoretically, such minimum or maximum in (quasi-)1D gapped spin systems could indicate a crossover to low-temperature TLL region, and a 3D ordering would be found slightly below T_{ex} with 3D interactions [14, 43]. In fact, the behavior of T_{ex} vs. H in the present measurements could indicate the TLL crossover as discussed later.

In the previous report [50], 3D ordering temperature, T_c, from χ-T was determined from a kink anomaly of the temperature derivative of χ, and it was in good agreement with T_c determined from a peak of the temperature dependence of the specific heat C (Fig. 4.3(b), Fig. 4.10). This correspondence is considered to be associated with Fisher's relation for

antiferromagnets,

$$C(T) \sim a\frac{\partial}{\partial T}(T\chi)\,, \tag{4.1}$$

which describes that the specific heat near a second-order AFM phase transition can be scaled with the temperature derivative of $T\chi$ (the coefficient a is a slowly varying function near the transition) [67]. Note that the most singular part in Eq. (4.1) arises from the temperature derivative of χ itself. This relation has been confirmed experimentally in several materials, e.g., Ref 68. In this sense, it would be the most plausible way to define T_c from $d\chi/dT$ or $d(T\chi)/dT$. As can be seen from Fig. 4.5(b) and Fig. 4.6(b), the temperature derivative of χ exhibits a kink anomaly below $T_{\rm ex}$ as reported previously. Here, we define the temperature at which the anomaly exists (minimum or maximum) in $d\chi/dT$ as T_c. We also applied a similar definition of T_c for $d(T\chi)/dT$ in Fig. 4.7 and find a dip (Fig. 4.7(a)) or peak (Fig. 4.7(b)) anomaly. We will discuss in Section 4.3.4 whether the difference of these definitions of T_c would affect the critical exponents of the 3D ordering phase boundary near the critical fields, H_{c1} and H_{c2}.

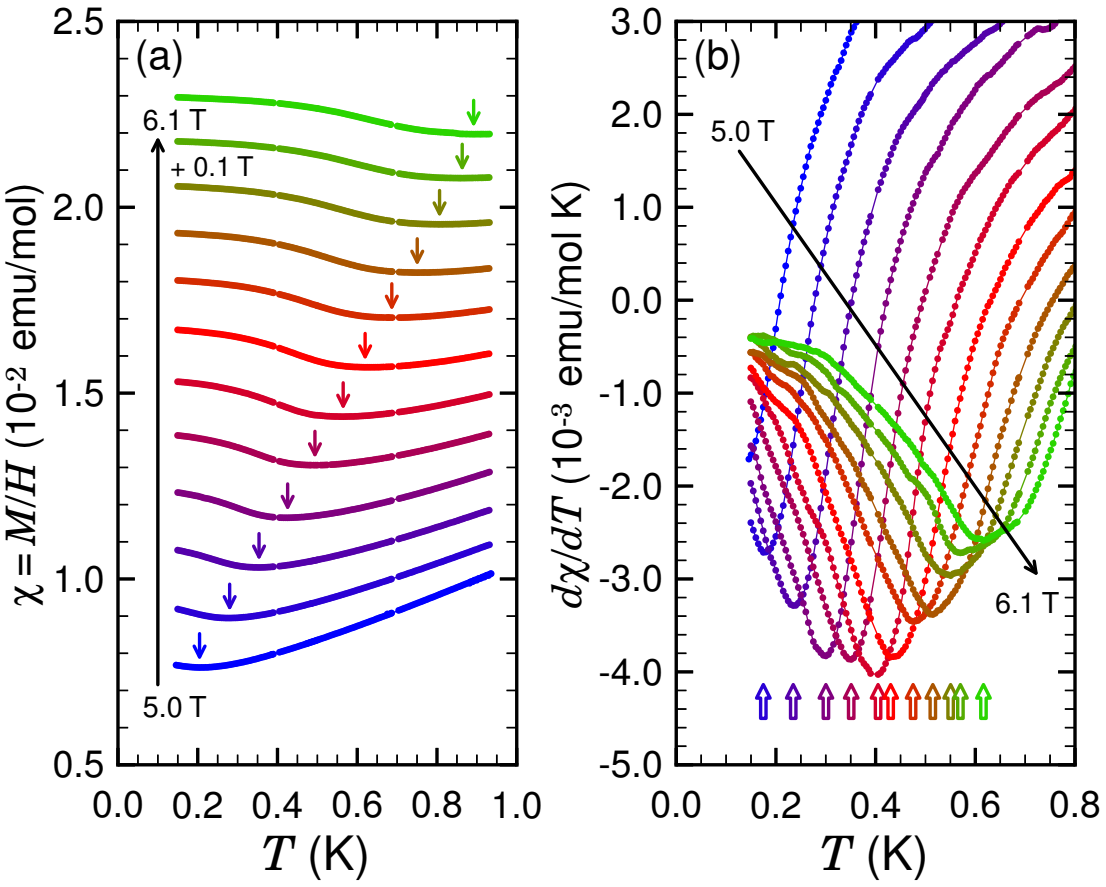

Figure 4.5: (a) Temperature dependence of the magnetic susceptibility $\chi = M/H$ in several magnetic fields between 5.0 T and 6.1 T. Arrows indicate the temperature $T_{\rm ex}$ at which χ takes the nontrivial minimum. (b) Temperature derivative of χ calculated from the data on (a). Open arrows show the transition temperature, T_c, defined from the minimum of the kink anomaly.

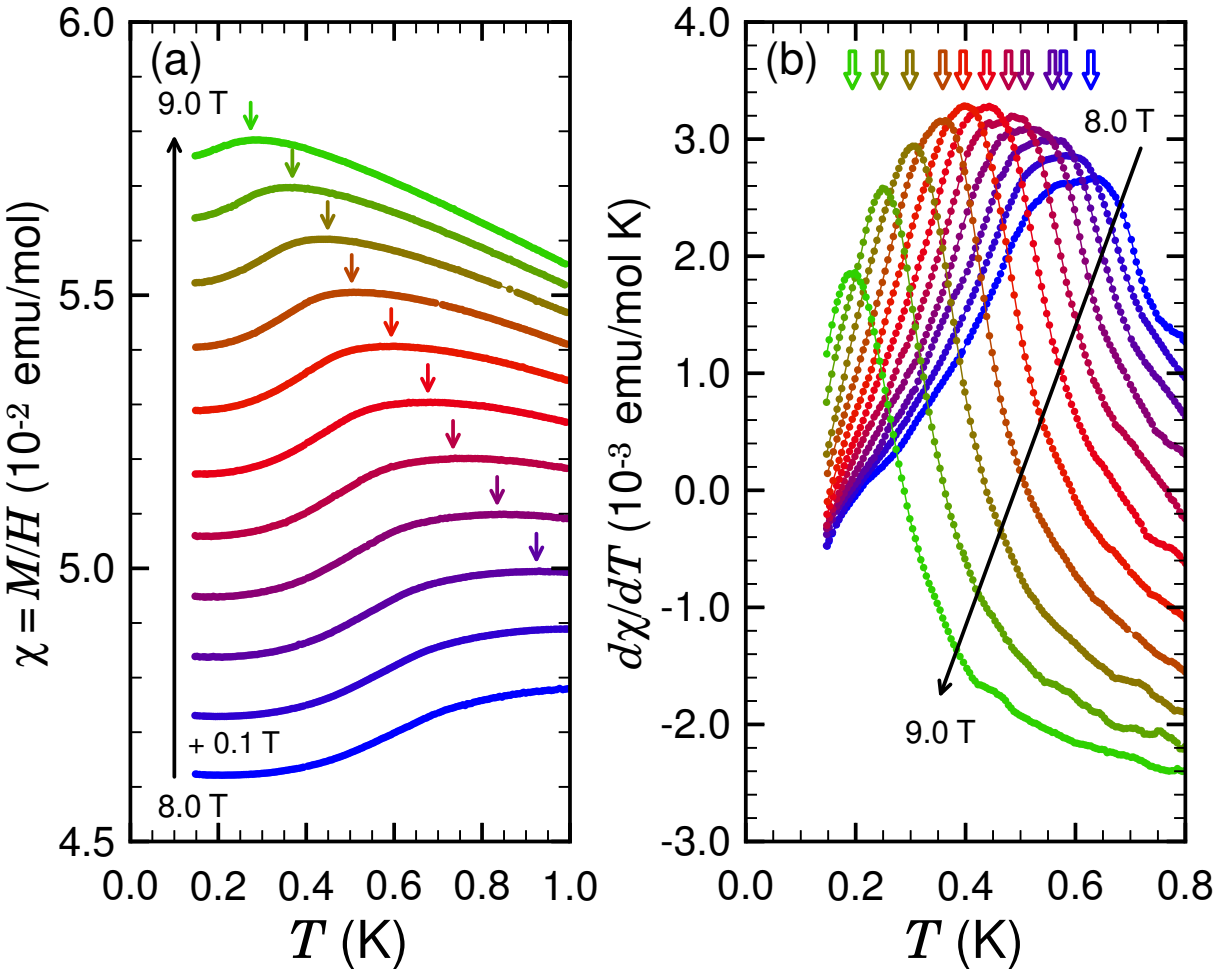

Figure 4.6: (a) Temperature dependence of the magnetic susceptibility $\chi = M/H$ in several magnetic fields between 8.0 T and 9.0 T. Arrows indicate the temperature $T_{\rm ex}$ at which χ takes the nontrivial maximum. (b) Temperature derivative of χ calculated from the data on (a). Open arrows show the transition temperature, T_c, defined from the maximum of the kink anomaly.

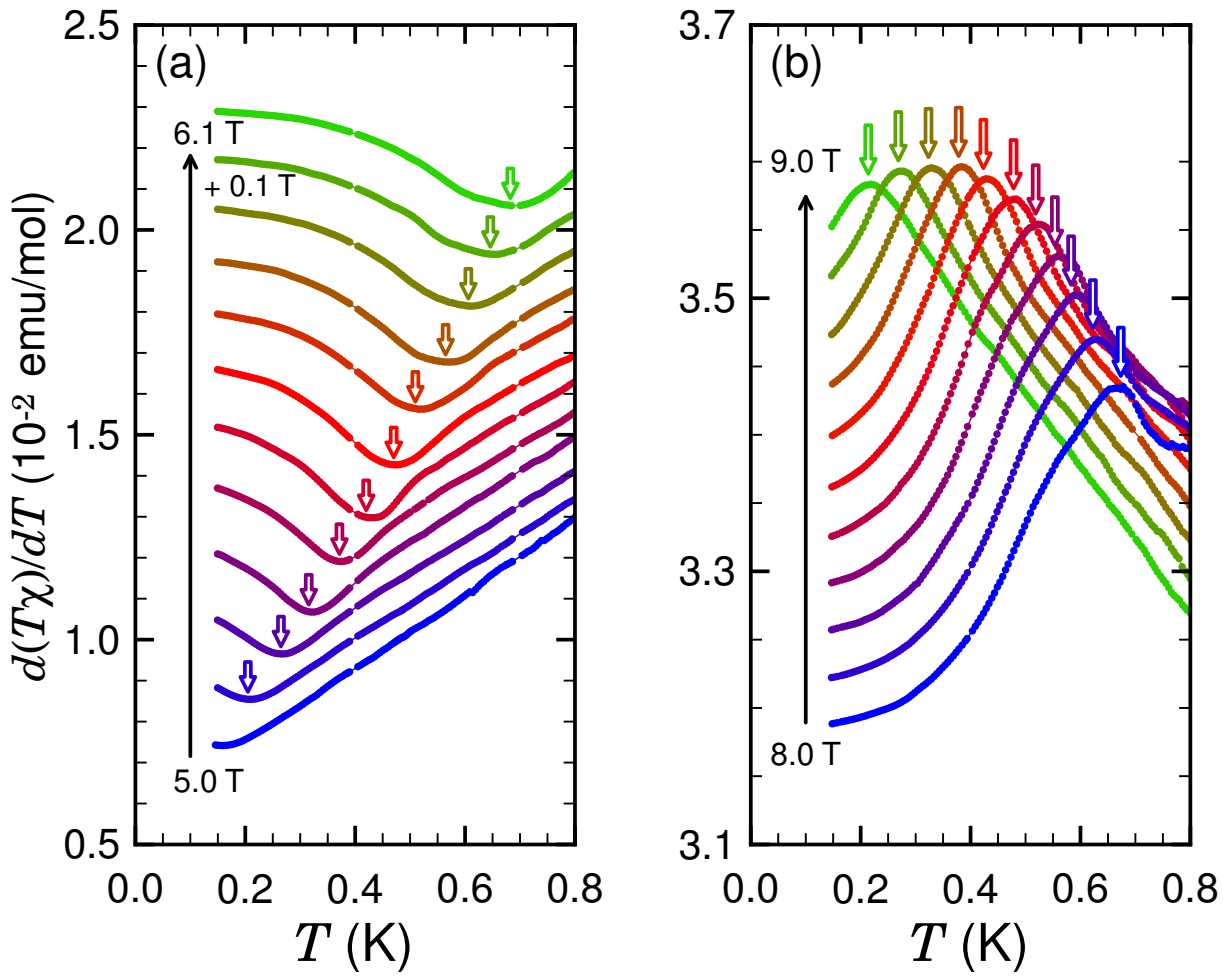

Figure 4.7: (a) Temperature derivative of $T\chi$ calculated from the data on Fig. 4.5(a). Open arrow shows the transition temperature defined from the minimum of the dip anomaly of each curve. (b) Temperature derivative of $T\chi$ calculated from the data on Fig. 4.6(a). Open arrow shows the transition temperature defined from the maximum of the peak anomaly of each curve.

4.3.2 Specific-heat Measurements

In Fig. 4.8(a) and (b), we show the magnetic heat capacity divided by temperature, $C_{\rm mag}/T$, in several magnetic fields near H_{c1} and H_{c2}, respectively. In these data, nuclear Schottky contributions from ^{1}H, ^{19}F, and ^{14}N are subtracted. The contributions are calculated from

$$C_{\rm nuc} = \frac{\hbar^2\gamma_n^2 I(I+1)H^2}{3k_{\rm B}T^2}, \tag{4.2}$$

where γ_n is a gyromagnetic ratio, and I is a nuclear spin (^{1}H: $\gamma_n/2\pi = 42.575\,$MHz/T, $I = 1/2$, ^{19}F: $\gamma_n/2\pi = 40.053\,$MHz/T, $I = 1/2$, and ^{14}N: $\gamma_n/2\pi = 3.076\,$MHz/T, $I = 1$ [55]). For example, as shown in Fig. 4.9, the upturn from nuclear Schottky contributions at 6 T below 0.2 K is well represented by the results of calculation, and it does not affect a sharp peak appearing at $\sim$0.4 K. The sharp peak indicates the 3D ordering as shown in the previous report [50]. On the other hand, the shoulder-like anomaly inferred in the previous report to be a partial ordering is weak (only the one at 7 T is indicated by an open arrow) or even indiscernible within the experimental resolution. This weakness of the partial ordering anomaly might be due to sample dependence discussed in the next section.

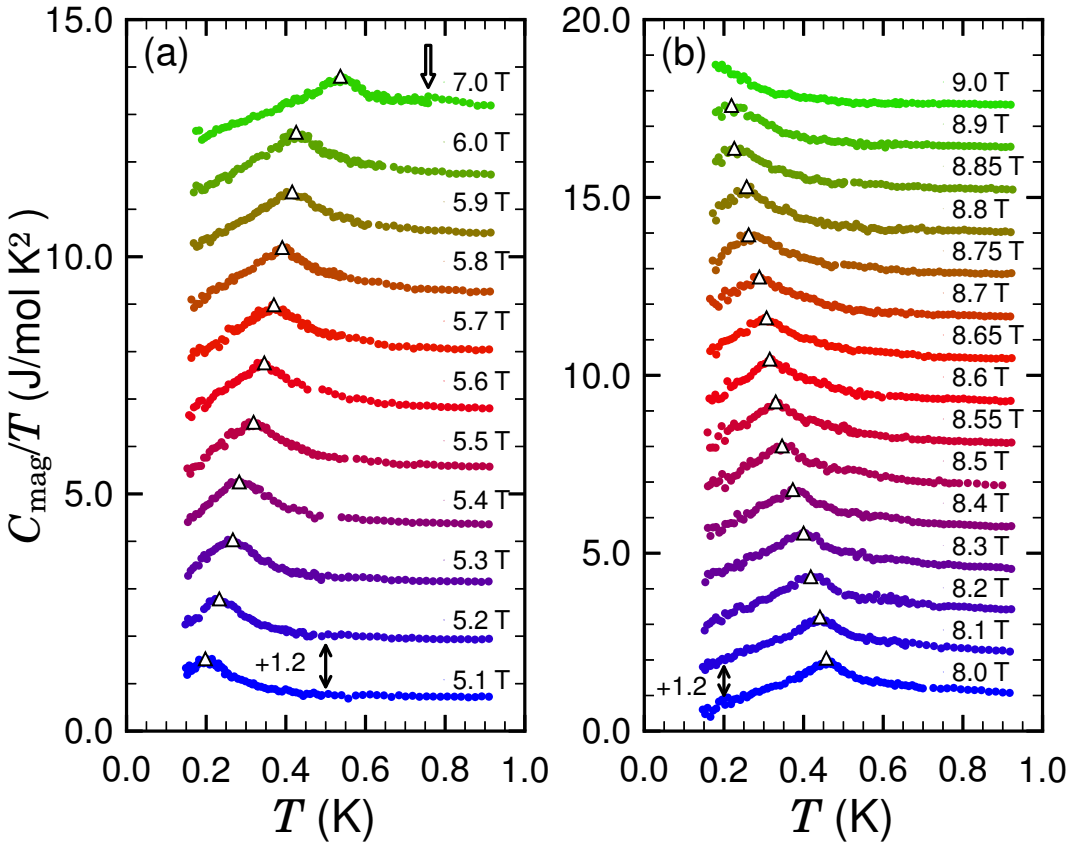

Figure 4.8: Temperature dependence of the magnetic specific heat (a) from 5.1 T to 7.0 T (b) from 8.0 T to 9.0 T. Each curve is shifted by +1.2 J/mol K^2 for clarity. Open arrow denotes the partial-ordering temperature at 7 T.

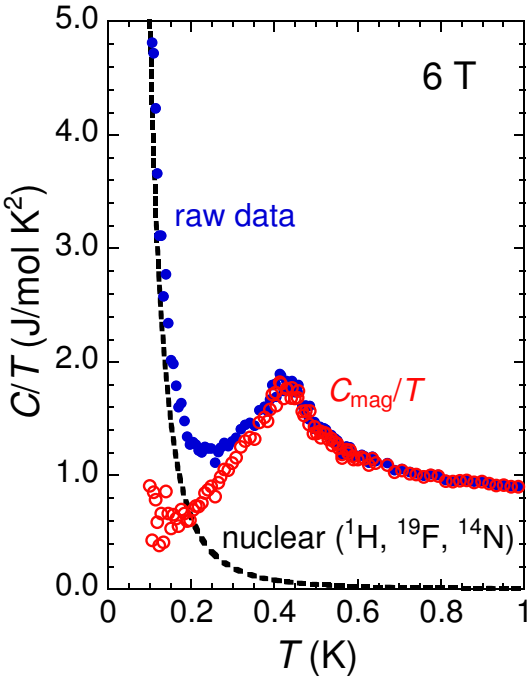

Figure 4.9: Closed symbols: raw data of the temperature dependence of the total specific heat at 6 T. Dashed line: calculated nuclear Schottky contribution from ^{1}H, ^{19}F, and ^{14}N at 6 T. Open symbols: the result of subtracting the nuclear Schottky contribution from the raw data.

4.3.3 Phase Boundary Determined from the Present Measurements

The 3D ordering temperatures observed in the present measurements are summarized in Fig. 4.10 together with the results reported previously [50]. A noticeable difference between the present and previous results is a disparity in the phase boundaries determined from $d\chi/dT$ and $C_{\rm mag}/T$; whereas in the previous study these two measurements yielded nearly the same transition temperature, the phase boundary defined from $d\chi/dT$ in the present experiment is higher in temperature than the one derived from $C_{\rm mag}/T$. It could be attributed to using the different samples for the magnetization and the heat capacity measurements in the present study. We ascribe this sample dependence to a high sensitivity of the interladder couplings to a strain in this system; the larger crystal used in the magnetization measurements could show slightly stronger interladder couplings. A cause of the weakness of the partial ordering anomaly in $C_{\rm mag}/T$ might also be due to such sample dependence since T_c determined by the present $C_{\rm mag}/T$ data is slightly lower than that obtained previously. From comparison with the previous results, the partial ordering region is expected to exist above T_c defined on each sample.

Note that all the phase boundaries can be well scaled to each other by T_c at 6 T, as shown in the inset of Fig. 4.10. This implies that the critical exponent ν of the phase boundary $T \sim |H_{c1,2}(T) - H_{c1,2}(0)|^{\nu}$ would not be affected by the sample characteristics and the different definitions of T_c on χ. We make analysis of the critical exponent of the phase

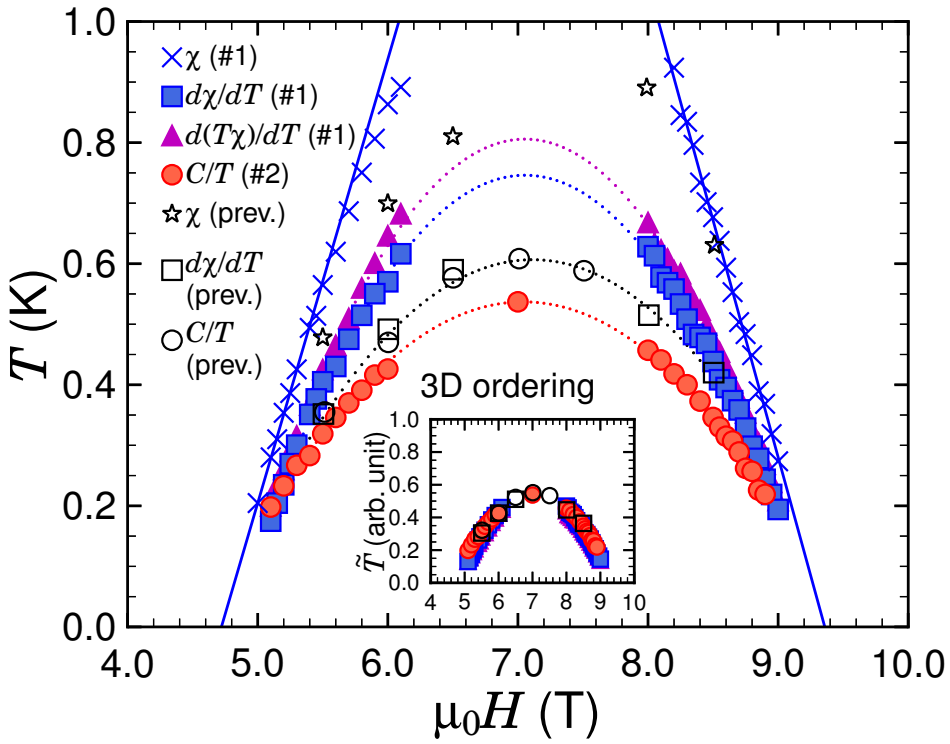

Figure 4.10: 3D ordering phase boundary determined from the present (previous, Ref. 50) measurements. Closed (open) circles and squares show T_c defined from the peak positions of $C_{\rm mag}/T$ and the kink anomalies of $d\chi/dT$, respectively. Triangles are defined from $d(T\chi)/dT$. Dotted lines are guides to the eye. Crosses (stars) denote the temperature $T_{\rm ex}$ at which the magnetic susceptibility χ takes extremum, and solid lines are a linear fit of $T_{\rm ex}$ at below 5.3 T and above 8.6 T for the present results. Inset: phase boundaries scaled by T_c at 6 T determined from the present data of $C_{\rm mag}/T$.

boundary for these differently defined T_c individually in the next section.

Another remarkable feature in Fig. 4.10 is the linear behavior of $T_{\rm ex}$ against the magnetic field near H_{c1} and H_{c2}. This behavior is reminiscent of a crossover to the TLL region in (quasi-)1D gapped spin systems [14]. Close to the critical field $H = H_c$, the crossover temperature $T_{\rm ex}$, at which the magnetization takes an extremum, is asymptotically expressed in the universal form

$$T_{\rm ex}(H) = c\,\frac{g\mu_{\rm B}}{k_{\rm B}}\,|H - H_{\rm c1,2}|\,, \tag{4.3}$$

where the coefficient $c = 0.762\,38$, and $k_{\rm B}$ is the Boltzmann constant. This linear relation has actually been observed on DIMPY [37] for the lower critical field, and the ideal spin-1/2 one-dimensional AFM chain CuPzN [15] for the saturation field. In the present case of 3-Br-4-F-V, a linear fit of the $T_{\rm ex}$ vs. H plot yields the absolute value of the linear coefficient 0.73±0.01 at fields below 5.3 T and 0.78±0.02 at fields above 8.6 T, both of which are smaller than the value determined from Eq. (4.3), $cg\mu_{\rm B}/k_{\rm B} = 1.0246$, assuming $g = 2$. Considering the fact that $T_{\rm ex}$ is relatively close to T_c in 3-Br-4-F-V compared with the above two examples, it is likely that the temperature region at which Eq. (4.3) can be applied is largely overlapped with the 3D ordering phase in 3-Br-4-F-V, although the linear relation between $T_{\rm ex}$ and H

can be ascribed to the quasi-one dimensionality of this compound.

4.3.4 Temperature-window Technique for the Critical Fields and Exponents

To extract the critical exponent ν of the 3D ordering phase boundary, we employ the temperature-window technique [27, 28, 69–71] in fitting the data by the power-law function $T \sim |H_{c1,2}(T) - H_{c1,2}(0)|^{\nu}$ with the least-squares method. Fortunately, the almost symmetric dome like phase diagram—in the boson language, this implies that the effect of quantum fluctuations on the boson effective mass at fields below H_{c1} is weak in this material [18]—enables us to replace the function with a quadratic form

$$T(h) = a\left(1 - h^2\right)^{\nu}, \tag{4.4}$$

by which the critical field can be determined more accurately [28]. In Eq. (4.4), a is a fitting coefficient, which is approximated as a constant, and the normalized field is defined as $h = [H_{c1,2}(T) - H_m]/|H_m - H_{c1,2}(0)|$, where H_m is the magnetic field centered in the 3D ordering dome (in this case, $\mu_0 H_m \sim 7\,\mathrm{T}$).

We first fit Eq. (4.4) to the data within the temperature window $0 \leq T \leq t_{\max}$ for several fixed ν's, where $t_{\max}$ is the maximum temperature of the window. Fig. 4.11 shows examples for the fitting method. The lowest value of $t_{\max}$ used is 0.27 and 0.28 K near $H_{c1}(h = -1)$ and $H_{c2}(h = 1)$, respectively, so that at least three data points are available for the fitting.

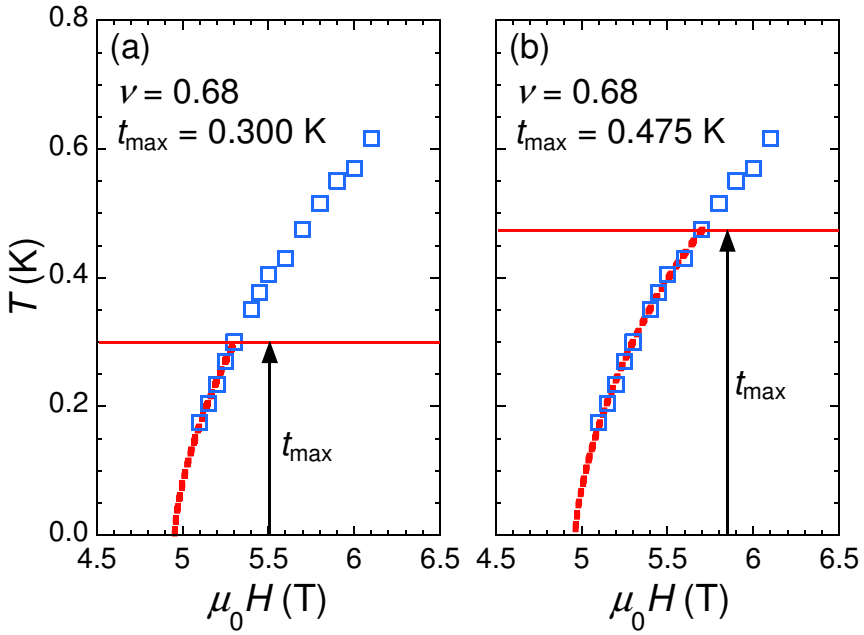

Figure 4.11: Examples of fitting Eq. (4.4) to the phase boundary determined from $d\chi/dT$ near H_{c1} with the fixed $\nu = 0.68$. Open squares are T_c from the kink anomalies of $d\chi/dT$. Dashed lines are fitting curves. The maximum temperature of the window is set at (a) $t_{\max} = 0.300\,\mathrm{K}$ (b) $t_{\max} = 0.475\,\mathrm{K}$.

For the given $t_{\rm max}$, the fitting parameters $H_{\rm c1,2}(0)$ are determined (referred to as $H_{\rm c1,2}(t_{\rm max})$). Iterating this procedure with increasing $t_{\rm max}$, we obtain $H_{\rm c1,2}(t_{\rm max})$ as a function of $t_{\rm max}$. The results of $H_{\rm c1}(t_{\rm max})$ and $H_{\rm c2}(t_{\rm max})$ determined from $d\chi/dT$ and $d(T\chi)/dT$ are shown in Fig. 4.12, and $H_{\rm c1}(t_{\rm max})$ and $H_{\rm c2}(t_{\rm max})$ from $C_{\rm mag}/T$ are shown in Fig. 4.13.

The zero-temperature limit $H_{\rm c1,2}(0)$ for each ν can be obtained by a linear extrapolation of the lowest few data points of $H_{\rm c1,2}(t_{\rm max})$. The number of points for fitting on each panel of Fig. 4.12 and Fig. 4.13 were selected so as to minimize the standard deviation of $H_{\rm c1,2}(0)$. As shown in Fig. 4.12 and Fig. 4.13, the linear fitting lines on each panel (dashed lines) converge on the narrow field region for a range of the ν values, analogous to the results of other compounds to which the same technique has been applied [28, 70, 71]. On fitting in Fig. 4.12, data points for 5.1 T and 9.0 T were eliminated since inclusion of these significantly prevented $H_{\rm c1,2}(0)$ from converging. Since χ itself shows weak anomalies at these fields, the anomalies in $d\chi/dT$ and $d(T\chi)/dT$ might become ambiguous. On fitting in Fig. 4.13(a) and (b), data points for 5.4 T, and 8.75 T, respectively, were eliminated because of similar non-

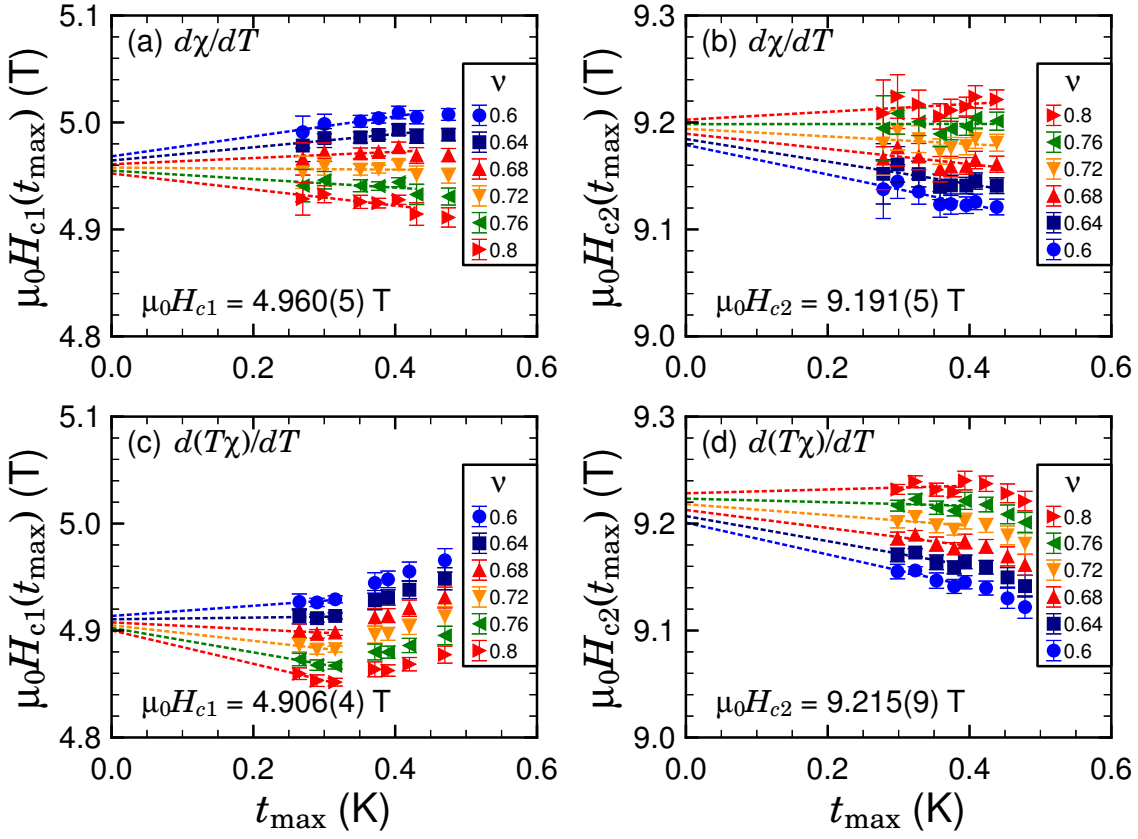

Figure 4.12: Fitting results of the temperature-window technique with Eq. (4.4), applied to the H-T phase diagram defined by $d\chi/dT$ and $d(T\chi)/dT$. As a function of the maximum temperature of the window, $t_{\rm max}$, for several fixed ν's, (a) $H_{\rm c1}$ and (b) $H_{\rm c2}$ from $d\chi/dT$, and (c) $H_{\rm c1}$ and (d) $H_{\rm c2}$ from $d(T\chi)/dT$ are shown. The dotted lines are linear fitting lines to a part of the data on each ν, used to determine $H_{\rm c1,2}(0)$ (see text). All the error bars represent fitting errors of the least-squares method.

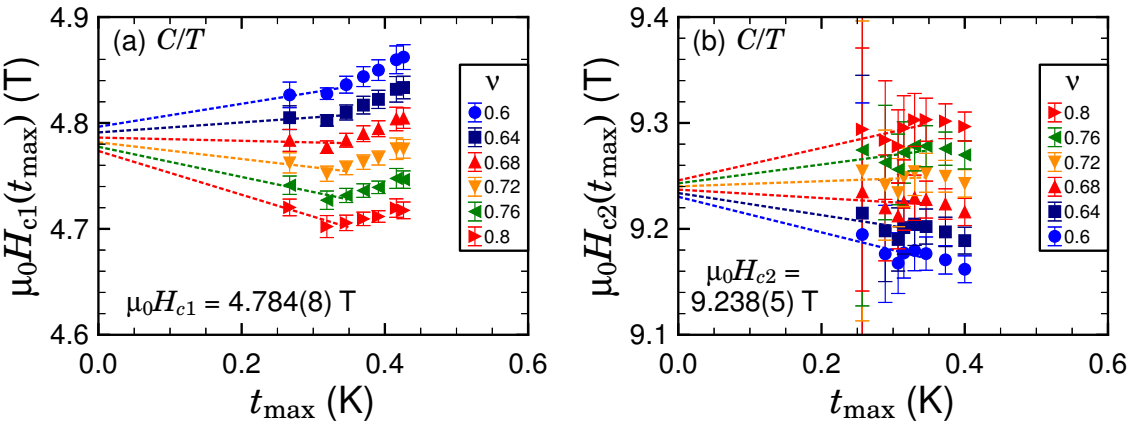

Figure 4.13: Fitting results of the temperature-window technique with Eq. (4.4), applied to the H-T phase diagram determined from $C_{\rm mag}/T$. As a function of the maximum temperature of the window, $t_{\rm max}$, for several fixed ν's, (a) $H_{\rm c1}$ and (b) $H_{\rm c2}$ from $C_{\rm mag}/T$ are shown. The dotted lines are linear fitting lines to a part of the data on each ν, used to determine $H_{\rm c1,2}(0)$ (see text). All the error bars represent fitting errors of the least-squares method.

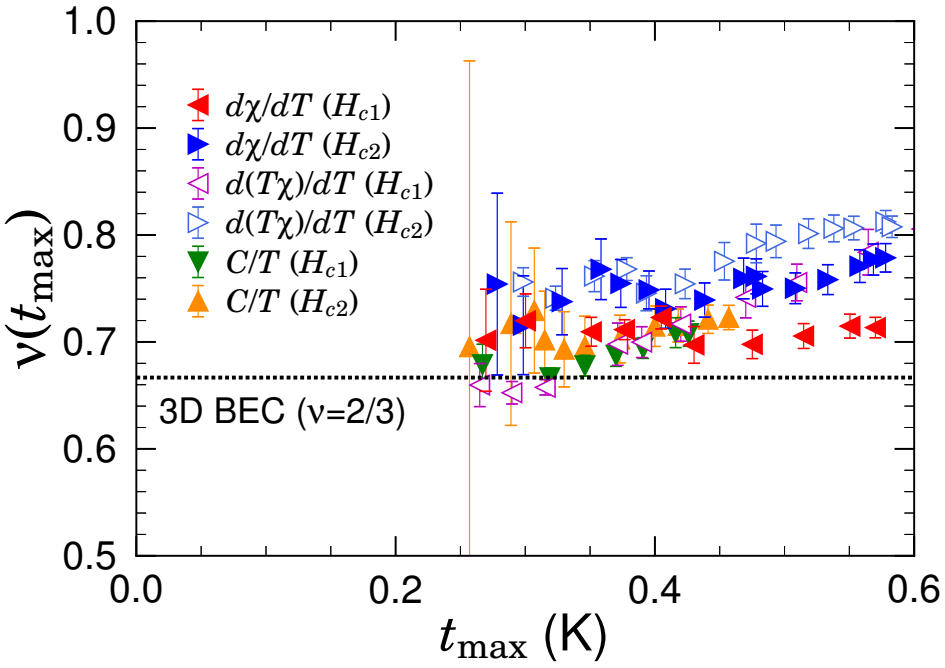

Figure 4.14: Critical exponent ν as a function of $t_{\rm max}$ with fixed $H_{\rm c1,2}(0)$ determined from Fig. 4.12 and Fig. 4.13. Closed (open) left and right triangles denote the results from $d\chi/dT$ ($d(T\chi)/dT$) near $H_{\rm c1}$ and $H_{\rm c2}$, respectively. Down and up triangles denote the results from $C_{\rm mag}/T$ near $H_{\rm c1}$ and $H_{\rm c2}$, respectively. The dashed line shows the critical exponent at the QCP that belongs to the 3D BEC universality class ($\nu = 2/3$). All the error bars represent fitting errors of the least-squares method.

convergence. We ascribe this non-convergence to that the partially ordering phase merges into the 3D ordering phase near the critical fields, which makes the anomalies obscure. Thus, irrespective for the particular ν value, the critical fields $H_{c1,2}(0)$ can be estimated to be $\mu_0 H_{c1} = 4.960(5)$ T (Fig. 4.12(a)) and $\mu_0 H_{c2} = 9.191(5)$ T (Fig. 4.12(b)) for $d\chi/dT$, and $\mu_0 H_{c1} = 4.906(4)$ T (Fig. 4.12(c)) and $H_{c2}(t_{max}) = 9.215(9)$ T (Fig. 4.12(d)) for $d(T\chi)/dT$. For C_{mag}/T, $\mu_0 H_{c1} = 4.784(8)$ T (Fig. 4.13(a)) and $H_{c2}(t_{max}) = 9.238(5)$ T (Fig. 4.13(b)).

Fixing $H_{c1,2}(0)$ to the values given above, the fitting of Eq. (4.4) to the data, in a similar manner but now ν being the fitting parameter, yields the critical exponent as a function of t_{max} (Fig. 4.14). As can be see in Fig. 4.14, all the $\nu(t_{max})$ plots thus obtained approach the value $\nu = 2/3$ of the 3D XY-AFM QCP at low temperatures, being definitely different from the 2D case $\nu = 1$ and the 3D Ising case $\nu = 0.5$ [18]. This tendency appears not to be dependent on the sample characteristics and the different definitions of T_c on χ, so that it could be universal behavior of the 3D ordering phase boundary of 3-Br-4-F-V. In the boson language, the result indicates that the field-induced QCPs of 3-Br-4-F-V belong to the 3D BEC universality class in the temperature range of the present measurements. This is the first observation of the 3D BEC exponent in a spin-1/2 ferro-leg ladder. Moreover, we emphasize that the critical exponent near H_{c2} is determined for the first time in gapped spin systems, most of which require more than tens of teslas to reach the saturation field and is difficult to examine the critical exponent.

4.4 Summary

We determined the critical exponents ν near the field-induced QCPs of the 3D ordering phase boundary on the spin-1/2 ferromagnetic-leg ladder 3-Br-4-F-V, using dc magnetization and specific-heat measurements. Near the lower critical field H_{c1} and the saturation field H_{c2}, the exponents obtained from the temperature-window fitting technique approach the value which belongs to the 3D BEC universality class, $\nu = 2/3$, at low temperatures. Although there is a split between the phase boundaries determined from the specific heat and the magnetization, which is attributed to different sample characteristics, the critical exponents at H_{c1} and H_{c2} seem not to be affected. This fact supports that the 3D BEC exponent is universal in the ordering phase of 3-Br-4-F-V. Of course the sample dependence of 3-Br-4-F-V remains to be clarified, but the results indicate that the verdazyl-radical-based FM-leg ladders are expected to be a model system to study BEC physics in quantum magnets.

Chapter 5

Unconventional Critical Exponent near the Saturation Field in the Spin-1/2 Ferromagnetic-leg Ladder 3-I-V

5.1 Introduction

5.1.1 Previous Studies of 3-I-V

3-I-V ($C_{20}N_4H_{16}I$) is a verdazyl-radical-based FM-leg ladder, similar to 3-Br-4-F-V (Chapter 4). The molecular packing is the same as 3-Br-4-F-V as shown in Fig. 4.1 (p. 30) [50], but the *ab initio* MO calculations have predicted that the spin ladder is of strong-leg type ($|J_{\rm rung}/J_{\rm leg}| < 1$) deriving from the difference of the chemical modification of the phenyl (Fig. 5.1). From comparison of QMC calculations with the magnetization curve, the coupling constants, $J_{\rm rung}$ and $J_{\rm leg}$, have been estimated to be 5.8 K and -11.6 K, respectively [44].

Unlike 3-Br-4-F-V, a 3D ordering has been observed even at zero magnetic field ($T_N = 1.4$ K, Fig. 5.2), i.e., there does not exist a zero-field spin gap predicted by the theory of FM-leg ladders with isotropic spin couplings [46–48]. The 3D ordering temperature determined from temperature dependences of the magnetic susceptibility and the specific heat (Fig. 5.3) are in good accordance with each other, and then neither a TLL state nor a partial ordering state such as 3-Br-4-F-V is observed [51], unlike the case of 3-Br-4-F-V. Meanwhile, the field dependence of the specific heat (the inset of Fig. 5.3) and the magnetization (Fig. 5.4) suggests an additional phase near the saturation field as indicated in Fig. 5.2.

Although the detailed properties of these phases have not been revealed yet, frustrated intra- and inter-ladder couplings evaluated by the MO calculations are likely to be a cause of the above characteristics of 3-I-V [51]. Schematic pictures of the evaluated couplings are shown in Fig. 5.5. In the intra-ladder couplings (Fig. 5.5(a)), $J_{\rm diag}$ is ferromagnetic, so that it makes geometrical frustration among the three couplings $J_{\rm leg}(<0)$, $J_{\rm rung}(>0)$, and $J_{\rm diag}(<0)$. The main inter-ladder couplings consist of a triangular unit formed by J_1, J_2, and J_3 as illustrated in Fig. 5.5(b) and (c). J_1, J_2, and J_3 have been evaluated as

antiferromagnetic, ferromagnetic, and ferromagnetic, respectively. It yields the same type of frustration as the intra-ladder couplings. The existence of the intra-ladder frustration has been considered to bring about the phase diagram different from 3-Br-4-F-V [51].

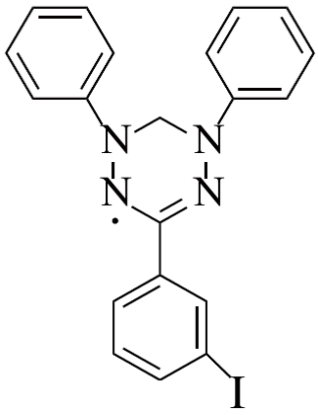

Figure 5.1: Structural formula of 3-I-V [51].

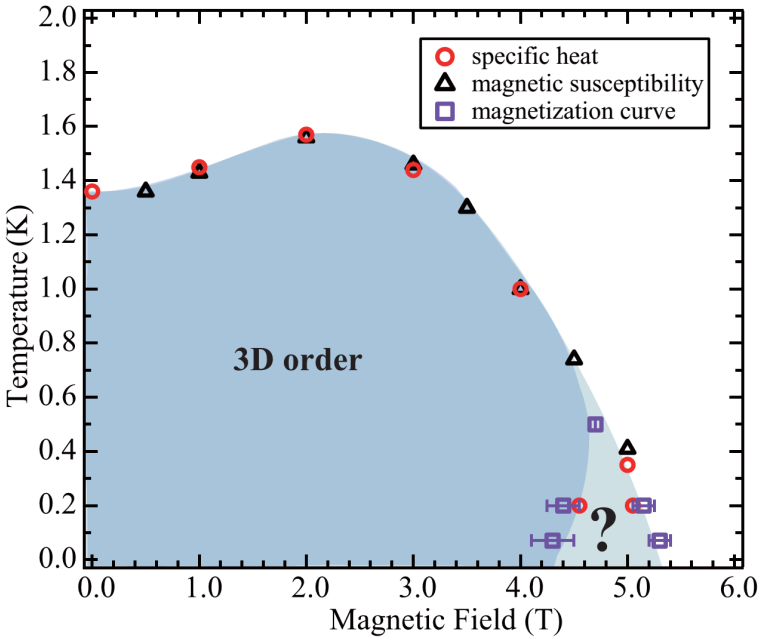

Figure 5.2: Previous result of phase diagram of 3-I-V, determined from the specific heat (circles), the magnetic susceptibility (triangles), and the magnetization curve (squares) [51].

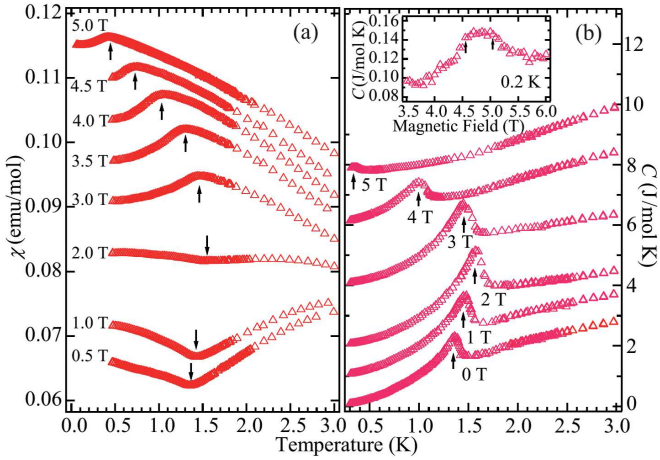

Figure 5.3: Previous results of temperature dependence of (a) the magnetization and (b) specific heat [51]. Inset: field-dependence of the specific heat. Arrows indicate 3D ordering transition points.

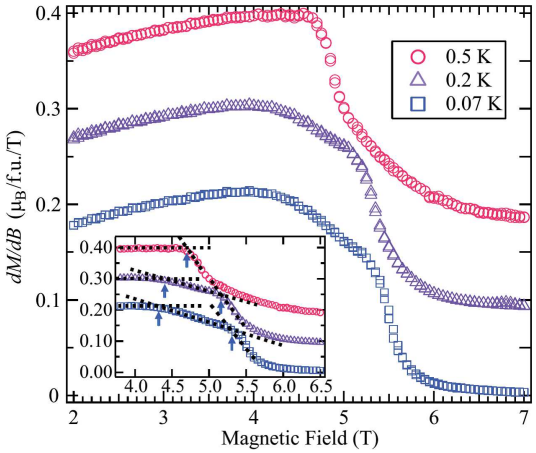

Figure 5.4: Previous results of the field derivative of the magnetization [51]. Inset: arrows indicate critical fields determined from the linear extrapolations (broken lines).

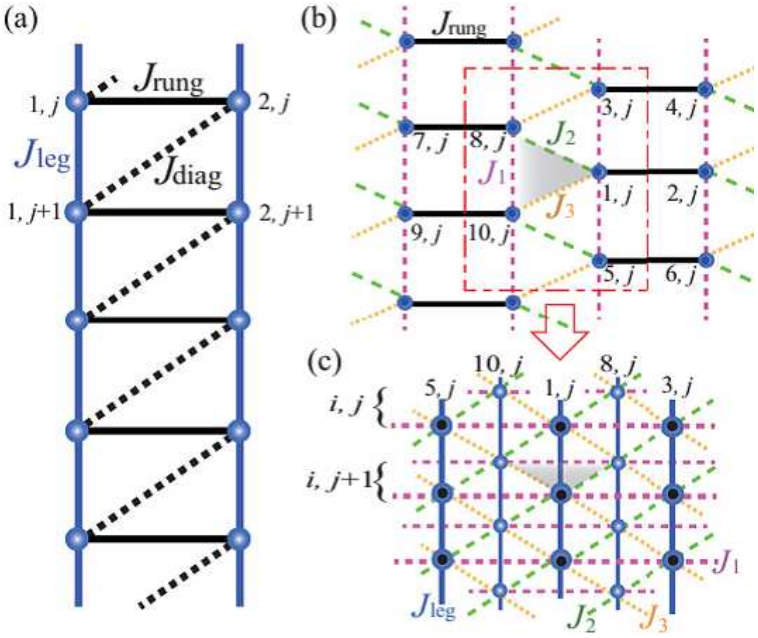

Figure 5.5: Schematic picture of frustrated intra- and inter-ladder couplings of 3-I-V, evaluated by the MO calculations [51]. (a) Intra-ladder couplings. $J_{\rm leg}(<0)$, $J_{\rm rung}(>0)$, and $J_{\rm diag}(<0)$ form a frustrated triangular unit. (b) Inter-ladder couplings viewed along the leg direction. $J_1(>0)$, $J_2(<0)$, and $J_3(<0)$ form a frustrated triangular unit. (c) Inter-ladder couplings viewed along the rung direction. Shadow triangles denote the same triangular unit.

5.1.2 Motivation of the Present Study

As indicated by the previous studies, 3-I-V has a remarkably different phase diagram from 3-Br-4-F-V although both of their spin models consist of the spin-1/2 FM-leg ladder. The distinction of these compounds could be attributed to the type of the FM-leg ladder, strong leg ($|J_{\rm rung}/J_{\rm leg}| < 1$ in 3-I-V) or strong rung ($|J_{\rm rung}/J_{\rm leg}| > 1$ in 3-Br-4-F-V), and the frustrated intra- and inter-ladder couplings. It is expected that these differences of the parameters might also affect the critical exponent near the saturation filed, giving an insight into the additional phase of 3-I-V. In the present study, we thus focused on the critical exponent of the phase boundary and re-examined the previously-reported additional phase by detailed dc magnetization and specific-heat measurements.

5.2 Experimental

Single-crystal samples of 3-I-V were prepared in Hosokoshi lab at Osaka Prefecture University as reported in Ref. 44, similar to 3-Br-4-F-V. Dc magnetization measurements were performed by means of the capacitance-Faraday method with the Mg-type capacitor (Chapter 2) on single crystals, the mass of which was 2.52 mg (Fig. 5.6). Specific-heat measurements were carried out by the standard quasi-adiabatic heat-pulse and relaxation methods (Chapter 2), using the same samples. In both measurements, a ^{3}He-^{4}He dilution refrigerator was used in the temperature ranges $0.1\,{\rm K} \leq T \leq 1\,{\rm K}$. In all the measurements, magnetic fields up to 8 T were applied perpendicular to the $\boldsymbol{a}$ axis (perpendicular to the leg direction).

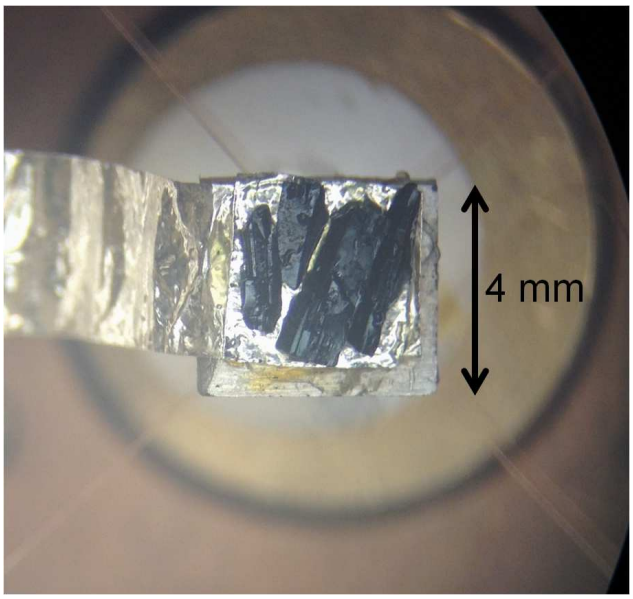

Figure 5.6: Single-crystal samples of 3-I-V on the capacitor. The same samples were also used in the specific-heat measurements.

5.3 Results and Discussion

5.3.1 Field Dependence of the Magnetization and the Specific Heat

Figure 5.7 shows the present result of the magnetization curve at 80 mK and the field derivative of the curve. In the previous report [51], two shoulder-like anomalies were observed in the field derivative of the magnetization, extracted by the linear extrapolations (Fig. 5.4). As can be seen in Fig. 5.7, the present result also indicates two shoulder-like anomalies near 4.0 T and 5.0 T. Since the previous definitions of the anomalies might be a bit obscure, we applied the second-order field derivative to the present data (d^2M/d^2H) as can be seen in Fig. 5.8. A sharp peak indicating the saturation can be observed at 5.38(1) T. A shoulder-like anomaly near 4.5 T can be associated with the phase boundary of the additional phase defined in the previous report, but it is to weak to be identified as a phase transition; it would be a crossover rather than a definite phase transition.

The present result of the field dependence of the specific heat as shown in Fig. 5.9 further demonstrates that "additional phase" is not completely independent of the main 3D ordering phase; there exists only a single sharp peak at about 5.1 T. Compared with the present data, the broad peak in the previous data seems to arise from a collapse of the sharp peak rather than an overlap of two phase transitions as discussed in Ref. 51. The difference of the peak heights could be attributed to a difference in the sample quality.

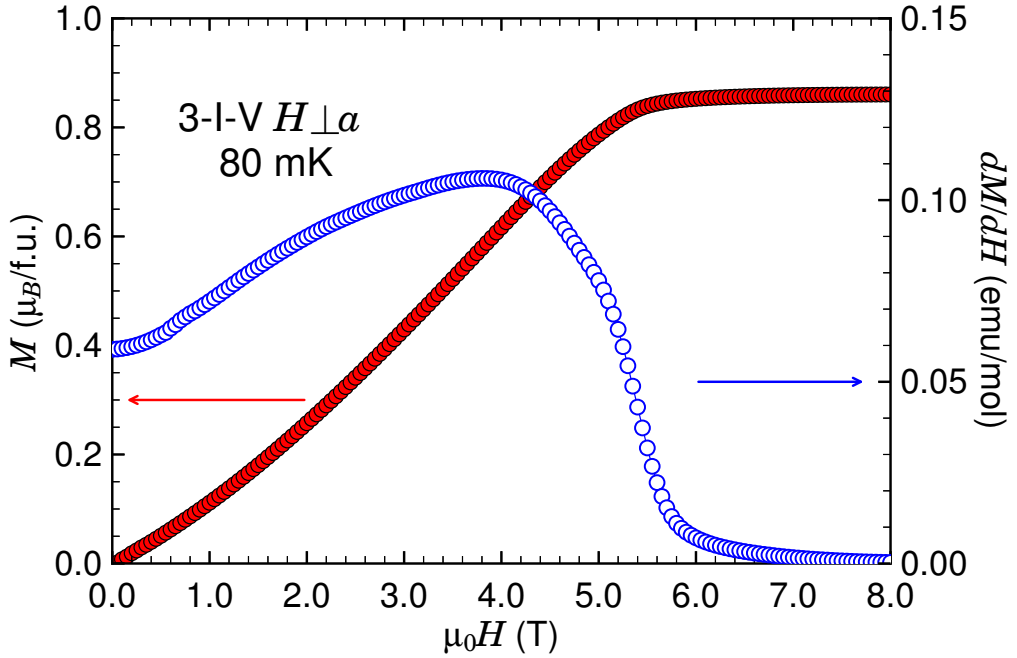

Figure 5.7: Present results of the magnetization curve at 80 mK (closed symbol), and the field derivative of the magnetization dM/dH (open symbol).

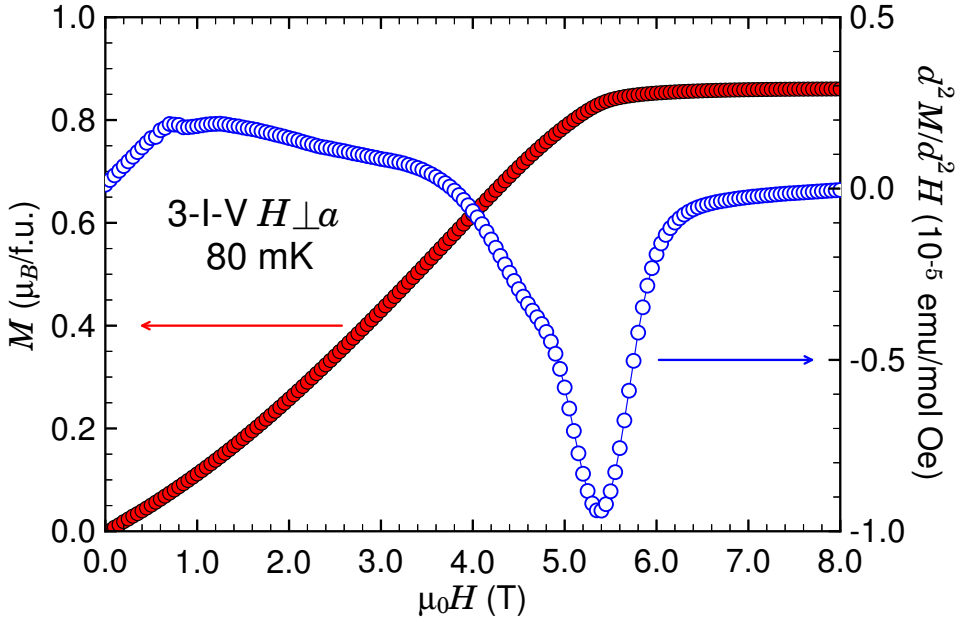

Figure 5.8: Present results of the magnetization curve at 80 mK (closed symbol), and the second-order field derivative of the magnetization d^2M/d^2H (open symbol).

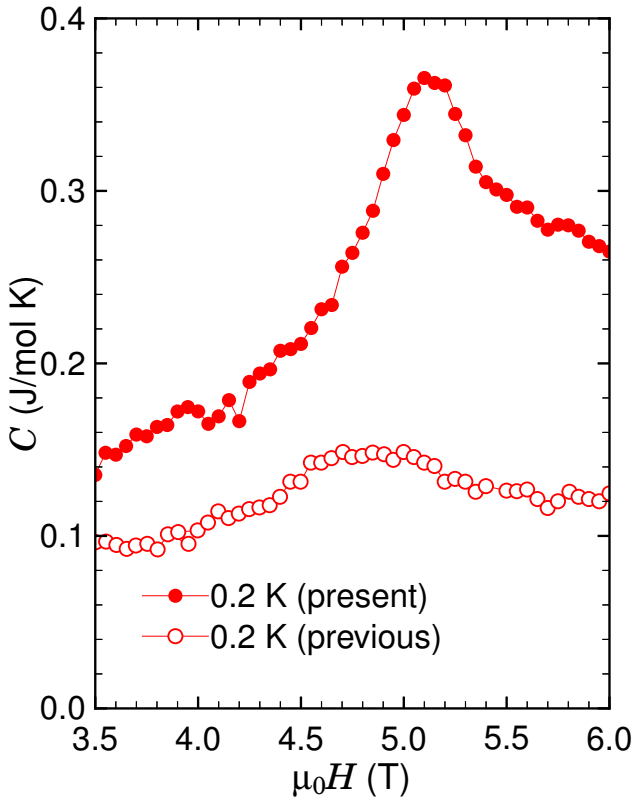

Figure 5.9: Present result of field dependence of the specific heat near the saturation (closed symbol), along with the previous one [51] (open symbol, extracted from the inset of Fig. 5.3).

5.3.2 Temperature Dependence of the Magnetic susceptibility and the Specific Heat

Figure 5.10 shows the present results of the temperature dependence of the magnetic susceptibility $\chi(T) = M(T)/H$ at several magnetic fields (see also Appendices, Section A.2, p. 69). There exists a cusp-like anomaly in each curve, the same as observed in the previous report [51]. The temperature at which the anomaly exists increases (decreases) with increasing the magnetic field at below (above) 2.2 T. Unlike 3-Br-4-F-V, a good coincidence between the cusp-like anomaly in $\chi(T)$ and the peak anomaly in the temperature dependence of the specific heat $C(T)$ (Fig. 5.2) has been obtained in the previous study. T_c may therefore be defined by the position of the cusp-like anomaly, which is the same definition in Ref. 51.

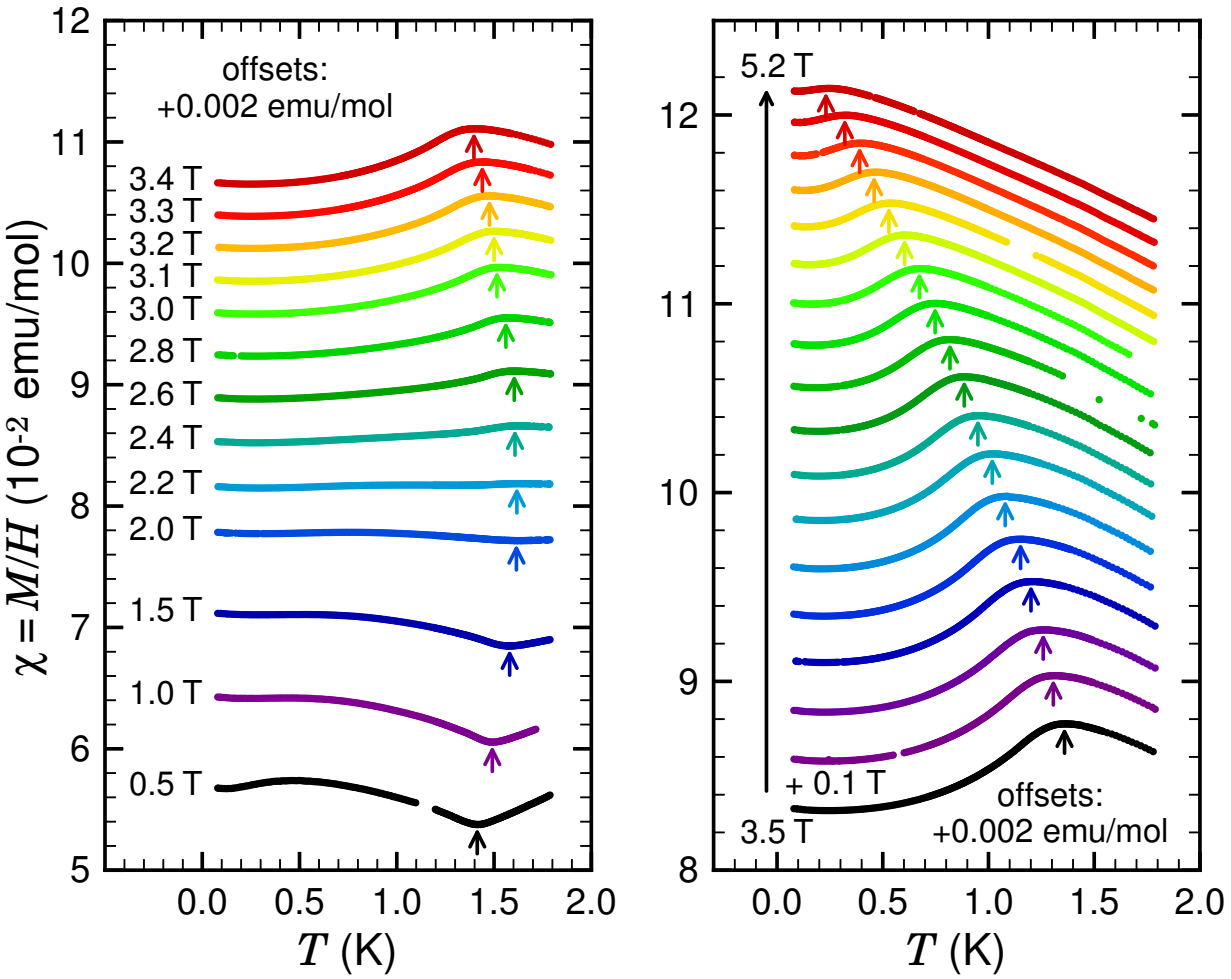

Figure 5.10: Temperature dependence of the magnetic susceptibility $\chi = M/H$ at several magnetic fields between 0.5 T and 3.4 T (left panel), and between 3.5 T and 5.2 T (right panel). For clarity, each curve is shifted by +0.002 emu/mol more than the one just below on each panel. Arrow denotes a minimum or maximum of cusp-like anomaly on each curve.

We also obtained $d(T\chi)/dT$ and $d\chi/dT$ as shown in Fig. 5.11 and Fig. 5.12, respectively, in order to check whether different definitions of T_c affect the results as has been done in 3-Br-4-F-V. $d(T\chi)/dT$ and $d\chi/dT$ show a dip or peak anomaly in each curve. The positions at which these anomalies exist are defined as T_c for $d(T\chi)/dT$ and $d\chi/dT$. These results are compared with each other in the next section.

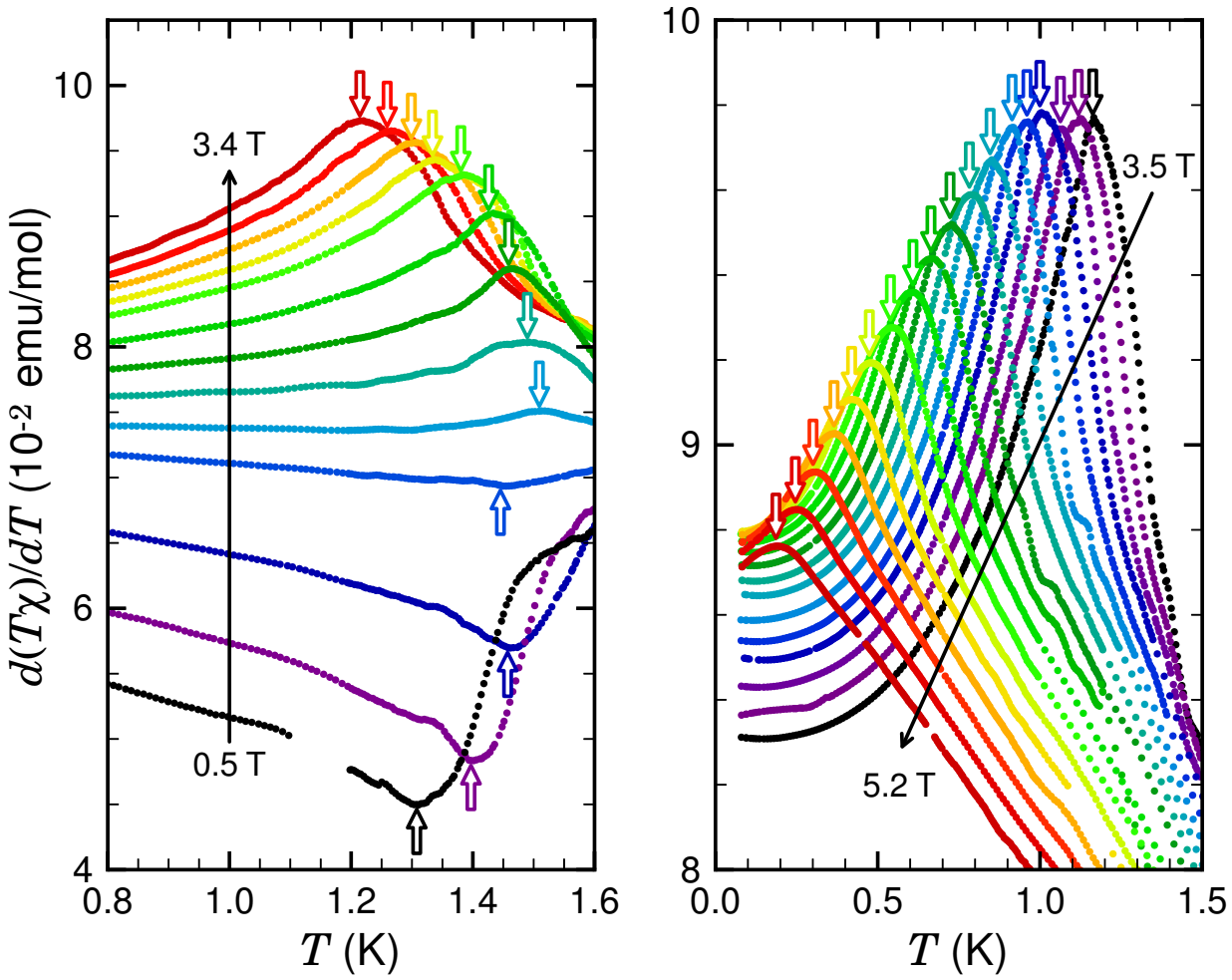

Figure 5.11: Temperature derivative of $T\chi$ obtained from the data on each panel of Fig. 5.10 ($d(T\chi)/dT$). Arrows denote dip or peak anomalies.

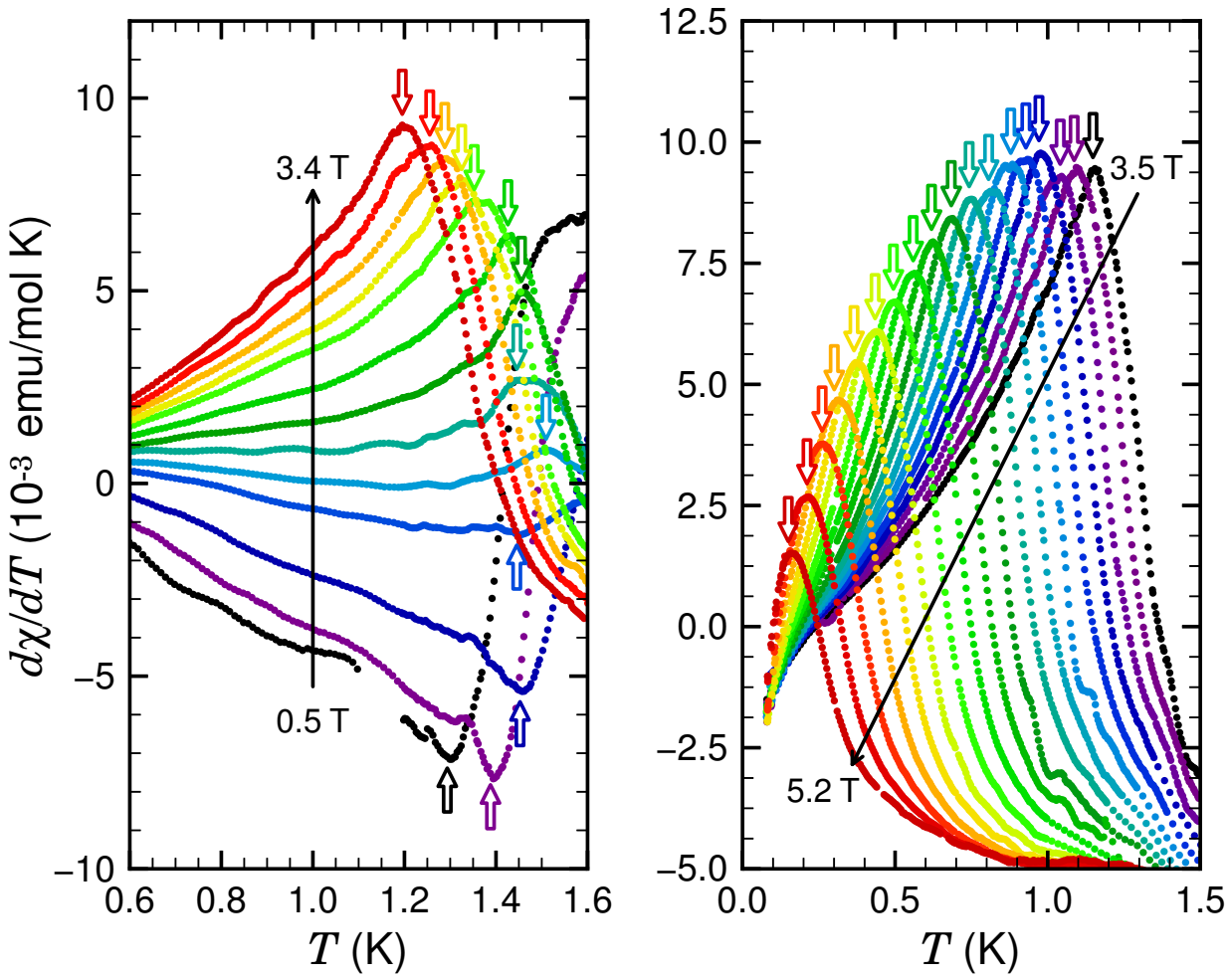

Figure 5.12: Temperature derivative of χ obtained from the data on each panel of Fig. 5.10 ($d\chi/dT$). Arrows denote dip or peak anomalies.

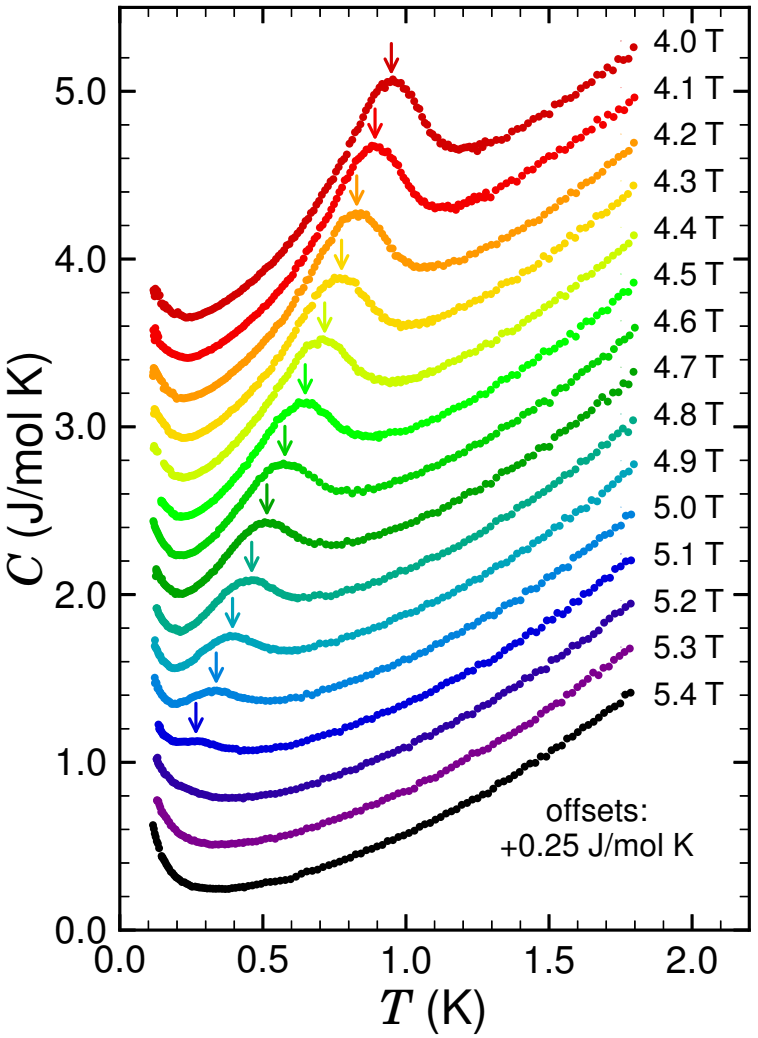

Figure 5.13: Temperature dependence of the specific heat at several magnetic fields between 4.0 T and 5.4 T. For clarity, each curve is shifted by +0.25 J/mol K more than the one just below. Arrows denote peak anomalies indicating the 3D ordering.

As can be seen in Fig. 5.13, temperature dependence of the specific heat $C(T)$ shows a peak anomaly (Fig. 5.13, see also Supplemental Materials, Section A.2, p. 72) as observed in the previous report (Fig. 5.3). $C(T)$ also shows a upturn at low temperatures in each magnetic field. The upturn would stem from nuclear Schottky contributions from ^{1}H, ^{127}I, and ^{14}N, but the simple calculation of the nuclear specific heat as used in 3-Br-4-F-V could not reproduce the upturn. Since ^{127}I has a relatively large nuclear spin $I = 5/2$, it may be that an effect of internal fields from ordered moments upon the nuclear quadrupole moments is non-negligible.

If the "additional phase" reported in Ref. 51 exists, some anomaly should be observed in the region around 4.5 T at below 0.6 K, which is clearly absent in the previous data of $\chi(T)$ and $C(T)$, as can be seen in Fig. 5.2. Indeed, no obvious sign of the additional transition can be observed in the present data of $\chi(T)$ and $C(T)$ as well as in the field dependence of

the specific heat. From these, the shoulder-like anomaly in d^2M/d^2H (Fig. 5.8) seems not to indicate a definite phase transition.

5.3.3 Phase Boundary Determined from the Present Measurements

The phase boundary determined from the present results of $\chi(T)$ and $C(T)$ is shown in Fig. 5.14, along with the previous one. Both are in good agreement with each other, implying the phase boundary is not sample dependent. As shown in Fig. 5.15, the boundary determined from $C(T)$ seems to be at slightly lower temperatures than that of $\chi(T)$. Since we used the same samples in both measurements of $\chi(T)$ and $C(T)$, different from the case in 3-Br-4-F-V, a cause of the slight disparity could be ascribed to a difference in the definitions of T_c.

In Fig. 5.15, the phase boundary defined from $d(T\chi)/dT$ is compared with the plots in Fig. 5.14 near the saturation field. The one from $d\chi/dT$ is also shown in Fig. 5.16. Compared with the results from $\chi(T)$ itself, the behavior of these boundaries defined from the derivative of χ are in better accordance with $C(T)$. In particular, T_c defined by $d(T\chi)/dT$ agrees with the one from $C(T)$ much better than that by $d\chi/dT$. We therefore make analysis of the critical exponent of the phase boundary for these differently defined T_c individually in the next section.

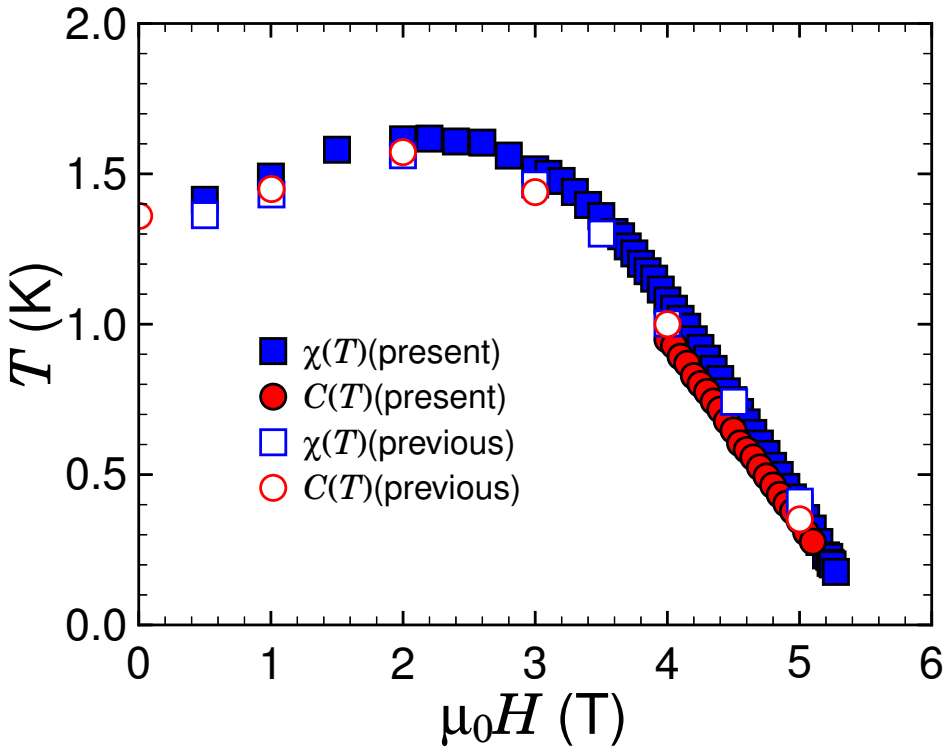

Figure 5.14: Phase boundary determined from the present results of temperature dependence of the magnetic susceptibility $\chi(T)$ (closed square) and the specific heat $C(T)$ (closed circle). Open symbols are the previous results [51] extracted from Fig. 5.2.

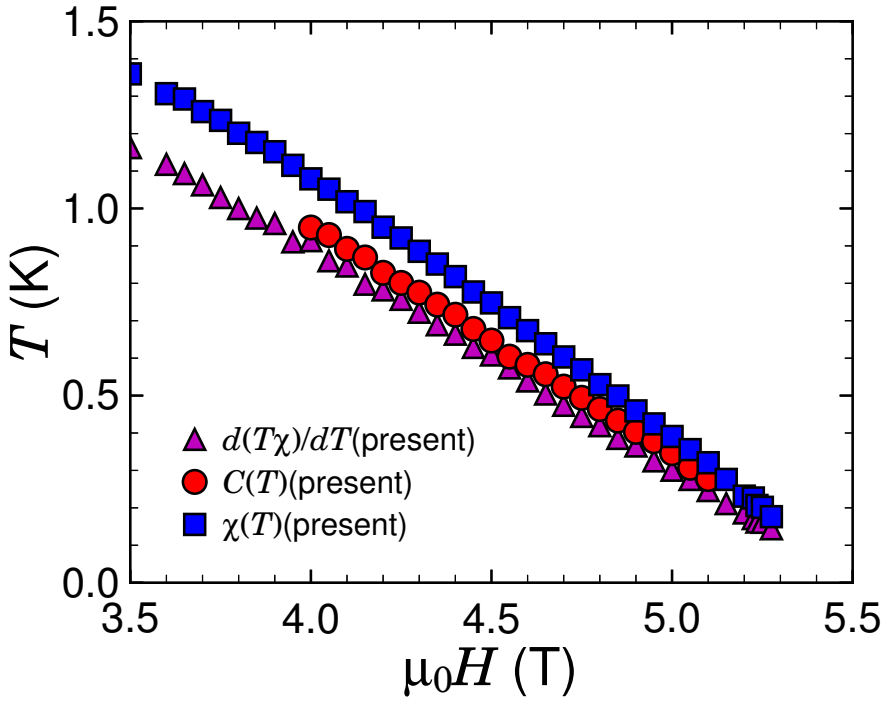

Figure 5.15: Enlarge plot of the phase boundary in Fig. 5.14 near the saturation, compared with the one defined from $d(T\chi)/dT$.

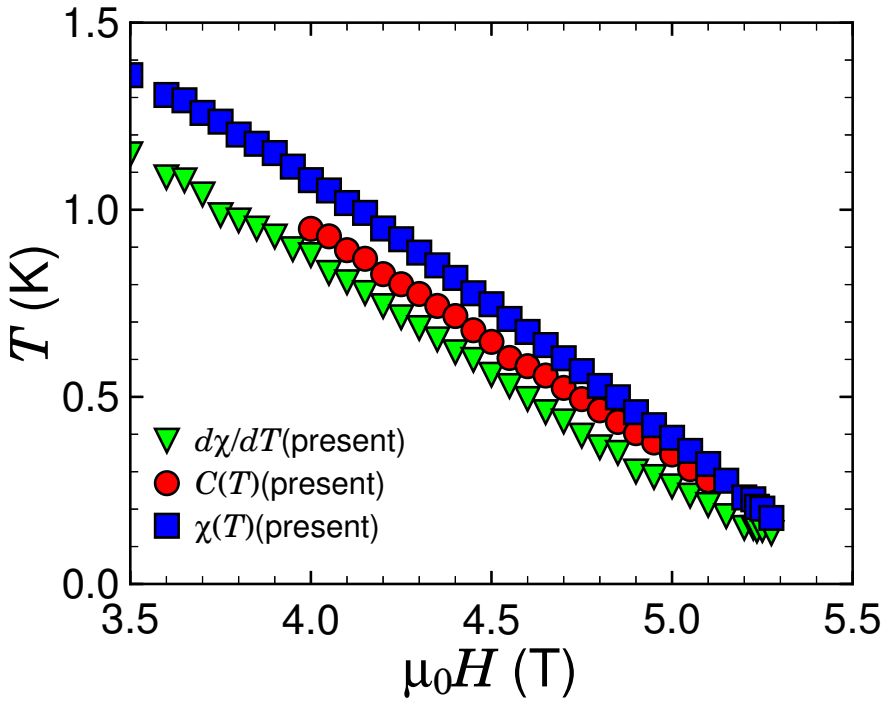

Figure 5.16: Enlarge plot of the phase boundary in Fig. 5.14 near the saturation, compared with the one defined from $d\chi/dT$.

5.3.4 Sliding-window Technique for the Critical Field and Exponent

In order to extract the critical field and exponent near the saturation field $H = H_c$, or the field-induced QCP, we employ the sliding-window technique as described in Ref. 29. The temperature-window technique as is used in 3-Br-4-F-V cannot be adapted in this case since the phase boundary has only one QCP and is not symmetric.

In the sliding-window technique, the power-law function $T \sim |H_c(T) - H_c(0)|^{\nu}$ is fitted with the data points on the phase boundary for various widths of the temperature window, ΔT by the least-squares method. Each temperature window is slided on the phase boundary, and then the fitting parameters, $H_c(0) = H_c$ and ν, can be obtained on various temperature regions. Fig. 5.17 shows two examples of the fitting results with $\Delta T = 0.3\,\mathrm{K}$ and $T_{\mathrm{win}} = 0.351\,\mathrm{K}$, and $\Delta T = 0.5\,\mathrm{K}$ and $T_{\mathrm{win}} = 0.779\,\mathrm{K}$, where T_{win} is the midpoint of the temperature window.

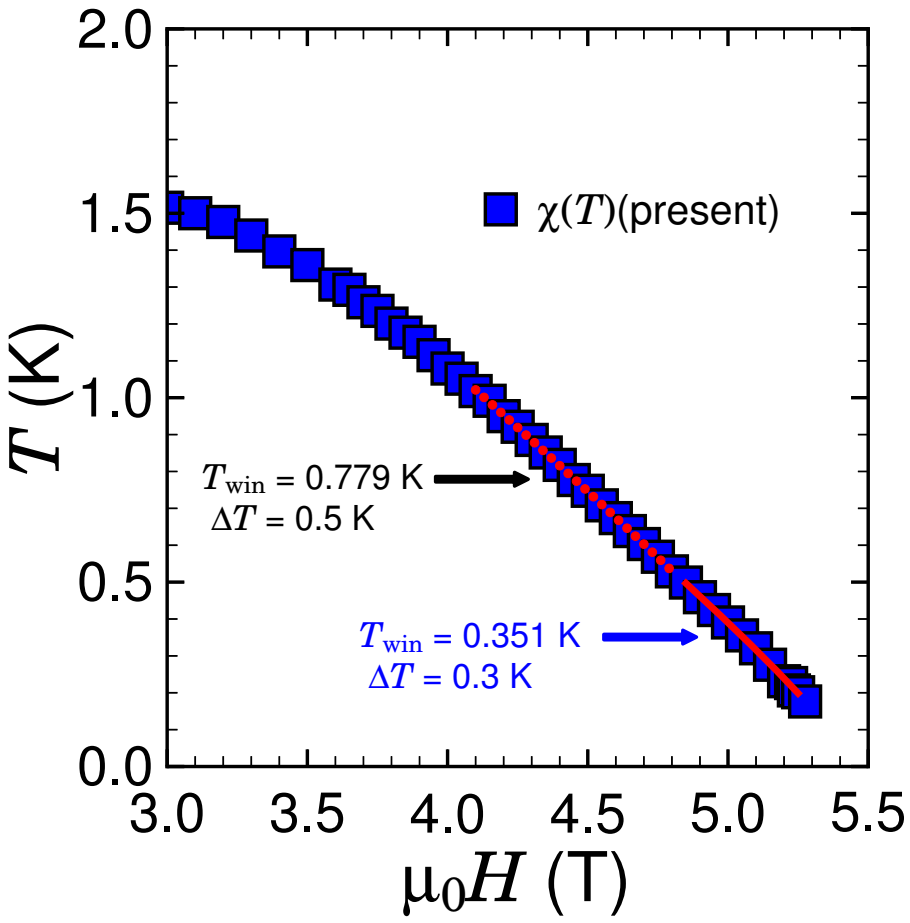

Figure 5.17: Examples of fitting results of the sliding-window technique, applied to the phase boundary determined from $\chi(T)$. Solid line is the fitting with the window parameters, $\Delta T = 0.3\,\mathrm{K}$ and $T_{\mathrm{win}} = 0.351\,\mathrm{K}$. Dotted line is the fitting with the window parameters, $\Delta T = 0.5\,\mathrm{K}$ and $T_{\mathrm{win}} = 0.779\,\mathrm{K}$ (see text).

With varying ΔT from 0.3 K to 1.1 K, we obtained the fitting parameters, H_c and ν as a function of $T_{\rm win}$ on the phase boundary determined from $\chi(T)$ as shown in Fig. 5.18. The critical field H_c approaches $H_c(0) = 5.4$ T in the limit of zero temperature (Fig. 5.18(a)). Interestingly, the critical exponent ν approaches $\nu = 1$ around $T_{\rm win} = 0.6$ K and then seems to approach $\nu = 2/3$ below $T_{\rm win} = 0.5$ K beyond the fitting error bars (Fig. 5.18(b)), i.e., it might indicate a crossover of the critical exponent from $\nu = 1$ to $\nu = 2/3$. Note that $T_{\rm win} = 0.5$ K is close to the temperature below which the "additional phase" was reported to exist in the previous study (cf. Fig. 5.2). The $\nu = 1$ behavior might thus be related to the shoulder-like anomaly in d^2M/d^2H.

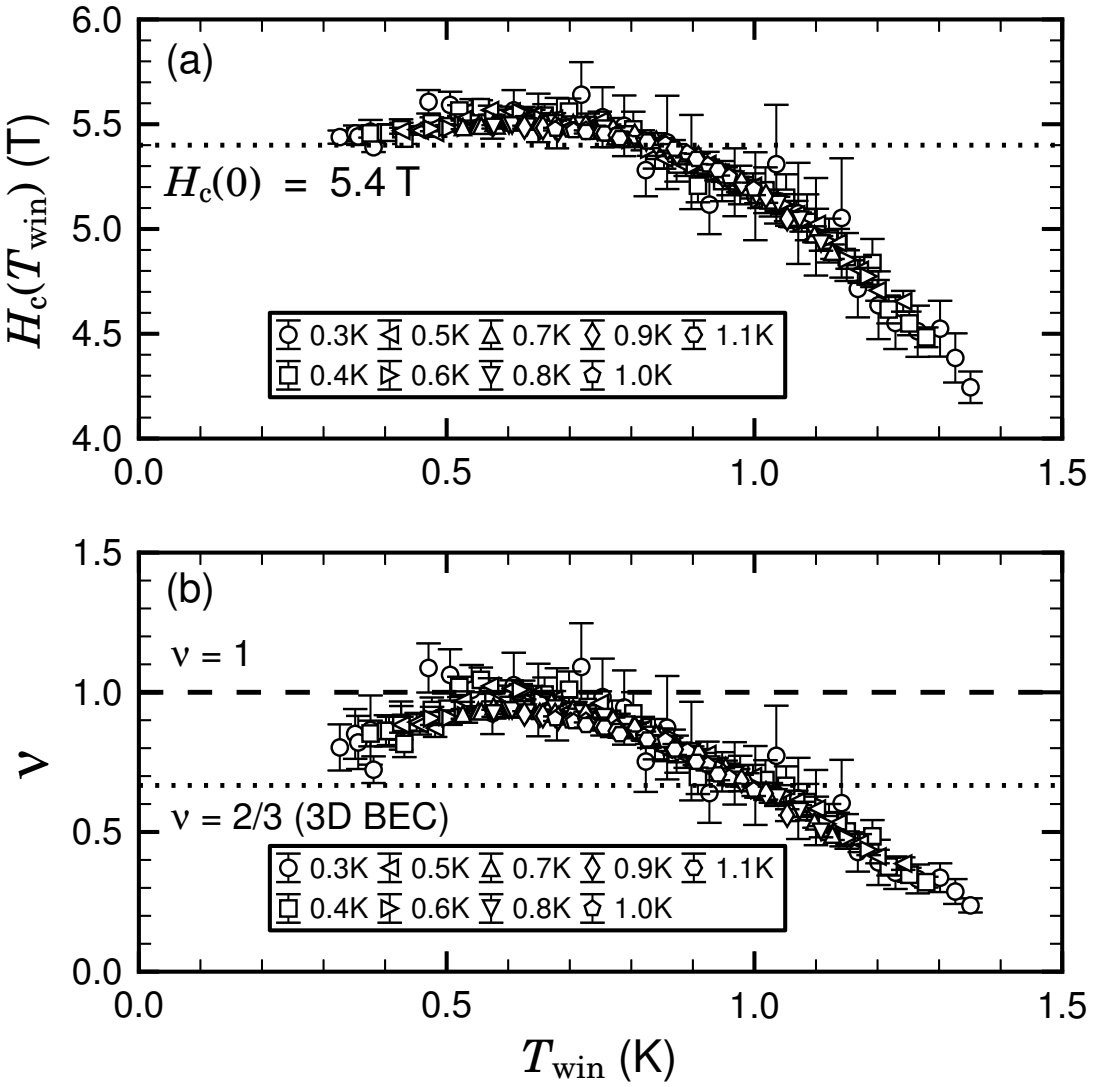

Figure 5.18: (a) The critical field H_c and (b) exponent ν, which are obtained from the sliding-window technique applied to the phase boundary from $\chi(T)$, vary with the midpoint of the temperature window $T_{\rm win}$. Different symbols denote the different temperature windows ΔT from 0.3 K to 1.1 K (see text). All the error bars represent fitting errors of the least squares method.

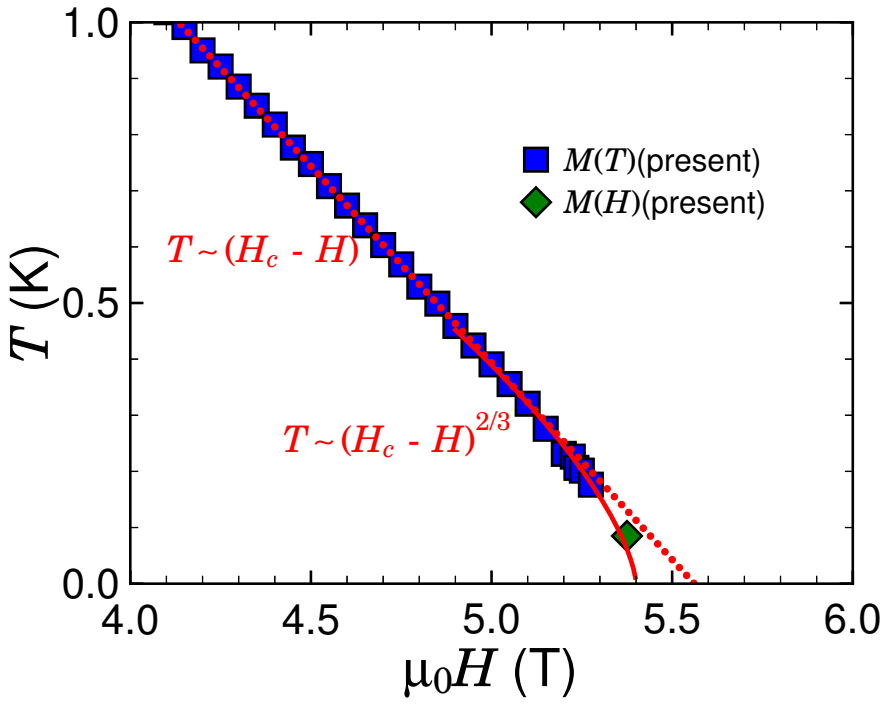

Figure 5.19: Dotted line denotes a linear fit of the phase boundary determined from $\chi(T)$ (square) between 0.5 K and 1 K, which yields the critical field $H_c = 5.561(5)$ T. The fitting curve $T = a(H_c - H)^{2/3}$ at $H_c = 5.4$ T (solid line) excellently reproduces the phase boundary at above 4.9 T. The critical field determined from d^2M/d^2H (diamond, see Fig. 5.8) at 80 mK is in good agreement with the fitting curve.

To check the behavior of the critical exponent of the phase boundary defined from $\chi(T)$, we refit the power-law function using the obtained parameters. As one can seen in Fig. 5.19, a linear fit can excellently reproduce the phase boundary from $\chi(T)$ between 0.5 K and 1 K (dotted line), and the extrapolated value of H_c at zero temperature is 5.561(5) T, which is consistent with the value around $T_{\rm win} = 0.6$ K in Fig. 5.18(a). On the other hand, the power-law function with $H_c = 5.4$ T and $\nu = 2/3$ can well reproduce the boundary below 0.5 K. Moreover, the critical field determined from d^2M/d^2H at 80 mK (Section 5.3.1) is in good agreement with the fitting curve derived only from the $\chi(T)$ data.

We applied a similar analysis to the phase boundaries defined by $d(T\chi)/dT$ and $d\chi/dT$. However, the critical exponents thus obtained behave differently from those obtained from the phase boundary defined by $d(T\chi)/dT$ and $d\chi/dT$ show different behavior obtained from $\chi(T)$ itself in the temperature region below $T_{\rm win} = 0.5$ K. As shown in Fig. 5.20, the critical exponent obtained from the $d(T\chi)/dT$ data levels off at $\nu = 1$ below $T_{\rm win} = 0.5$ K. On the other hand, the critical exponent obtained from $d\chi/dT$ data deviates from $\nu = 1$ and continues to increases below $T_{\rm win} = 0.5$ K (Fig. 5.21). We think the increase is not intrinsic since the peak anomaly of $\chi(T)$ on 3-I-V becomes very weak near $H_c(0)$, so that the calculation error in $d(T\chi)/dT$ or $d\chi/dT$ would increase near $H_c(0)$. Unfortunately, the crossover behavior below $T_{\rm win} = 0.5$ K remains controversial, but $\nu = 1$ region near $T_{\rm win} = 0.5$ K is common to all the definitions of T_c.

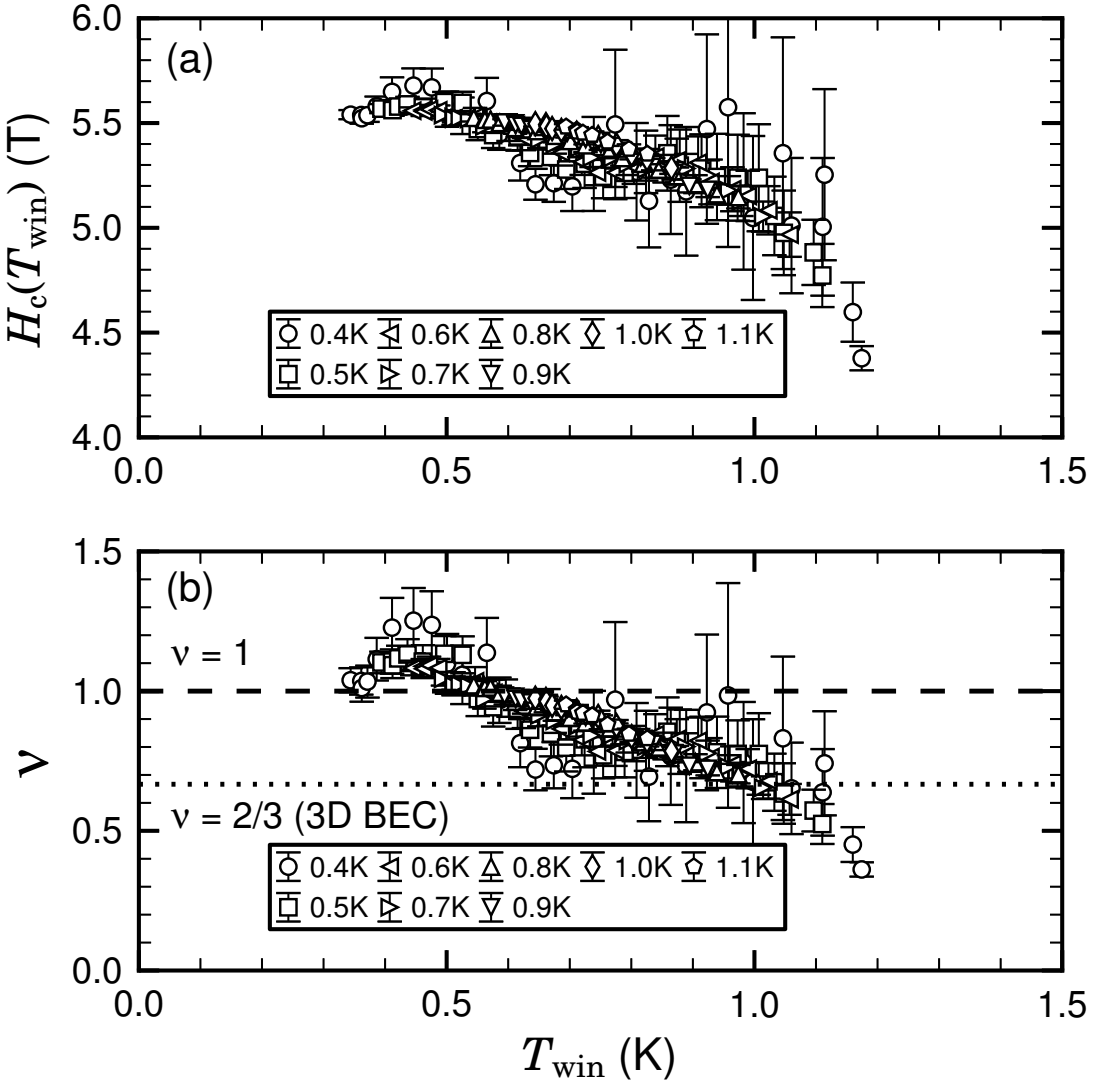

Figure 5.20: (a) The critical field H_c and (b) exponent ν, which are obtained from the sliding-window technique applied to the phase boundary from $d(T\chi)/dT$, vary with the midpoint of the temperature window $T_{\rm win}$. Different symbols denote the different temperature windows ΔT from 0.4 K to 1.1 K. All the error bars represent fitting errors of the least squares method.

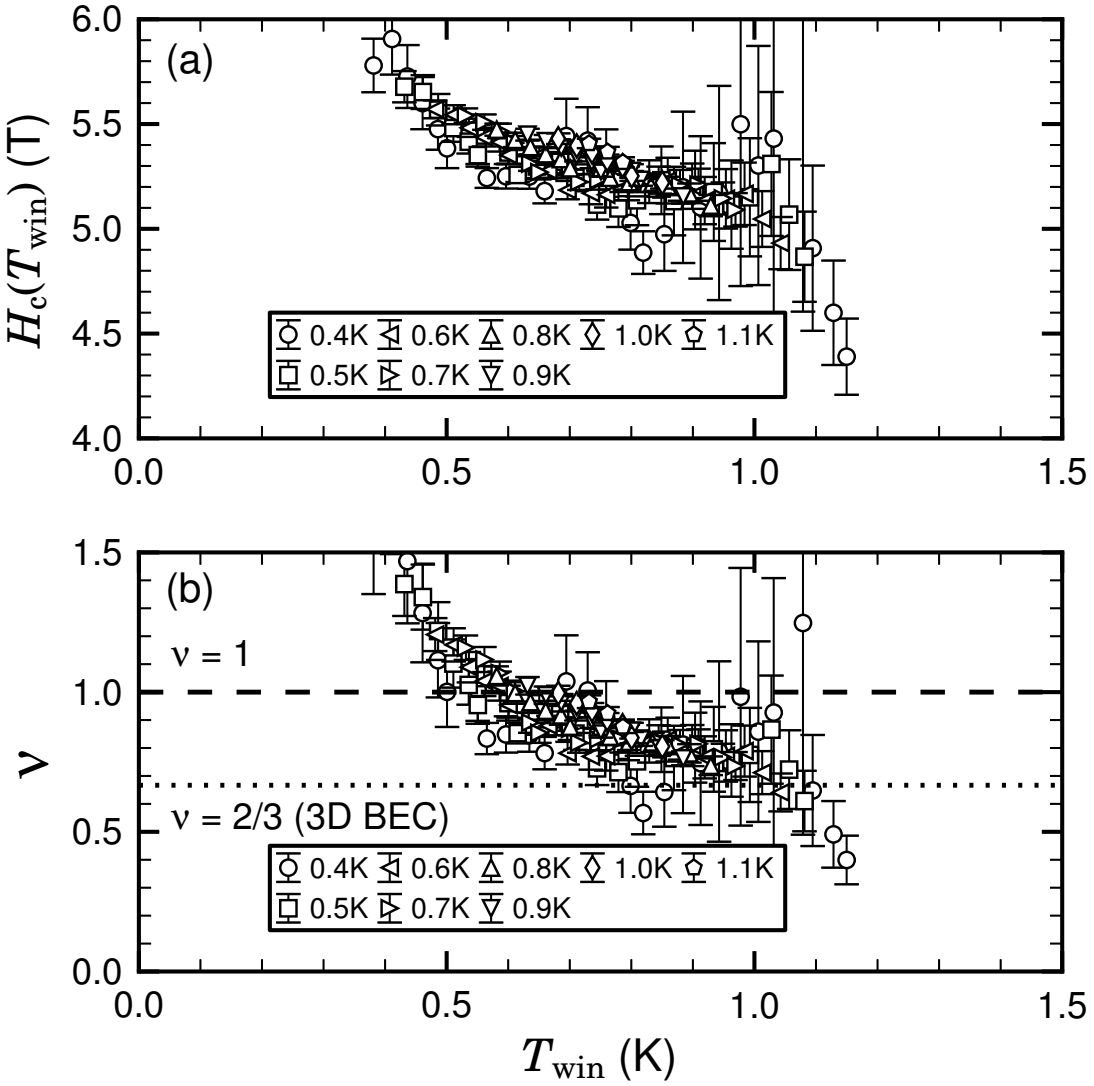

Figure 5.21: (a) The critical field H_c and (b) exponent ν, which are obtained from the sliding-window technique applied to the phase boundary from $d\chi/dT$, vary with the midpoint of the temperature window $T_{\rm win}$. Different symbols denote the different temperature windows ΔT from 0.4 K to 1.1 K. All the error bars represent fitting errors of the least squares method.

Figure 5.22 and Figure 5.23 show fitting results of the function $T = a(H_c - H)^{\nu}$ with the phase boundary defined from $d(T\chi)/dT$ and $d\chi/dT$, respectively, below 1 K. In Fig. 5.22, the best fitting yields $H_c = 5.51(2)$ T and $\nu = 0.99(2)$. In Fig. 5.23, the best fitting yields $H_c = 5.53(3)$ T and $\nu = 1.10(3)$. These results correspond to $\Delta T = 1$ K and $T_{\rm win} = 0.5$ K and reproduce the $\nu = 1$ region of the critical exponent. The critical field determined from d^2M/d^2H at 80 mK appears to be in line with these fitting curves, so that the crossover behavior for χ remains controversial in this sense.

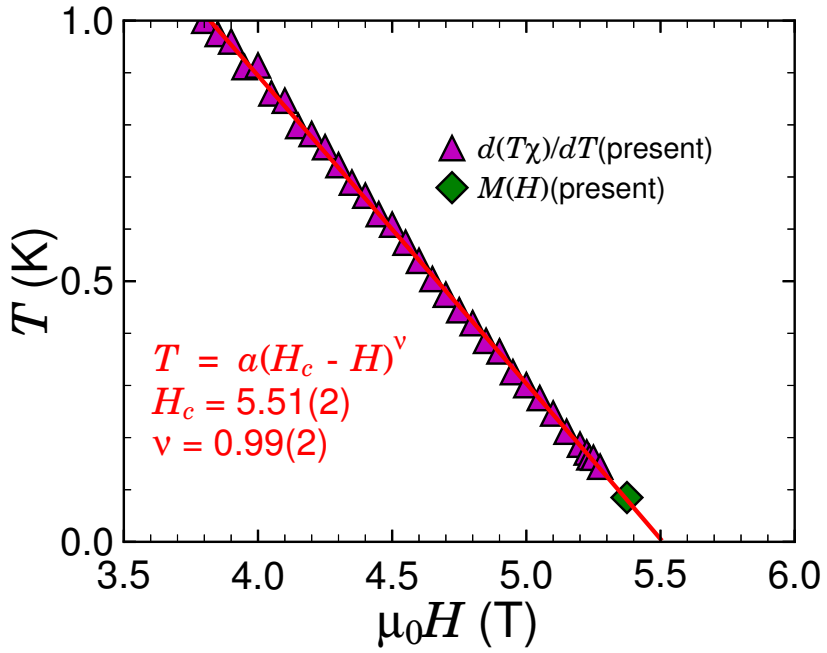

Figure 5.22: Fitting result of the function $T = a(H_c - H)^{\nu}$ with the phase boundary defined from $d(T\chi)/dT$ below 1 K (solid line). Best fitting yields $H_c = 5.51(2)$ T and $\nu = 0.99(2)$. Diamond is the critical field determined from d^2M/d^2H at 80 mK.

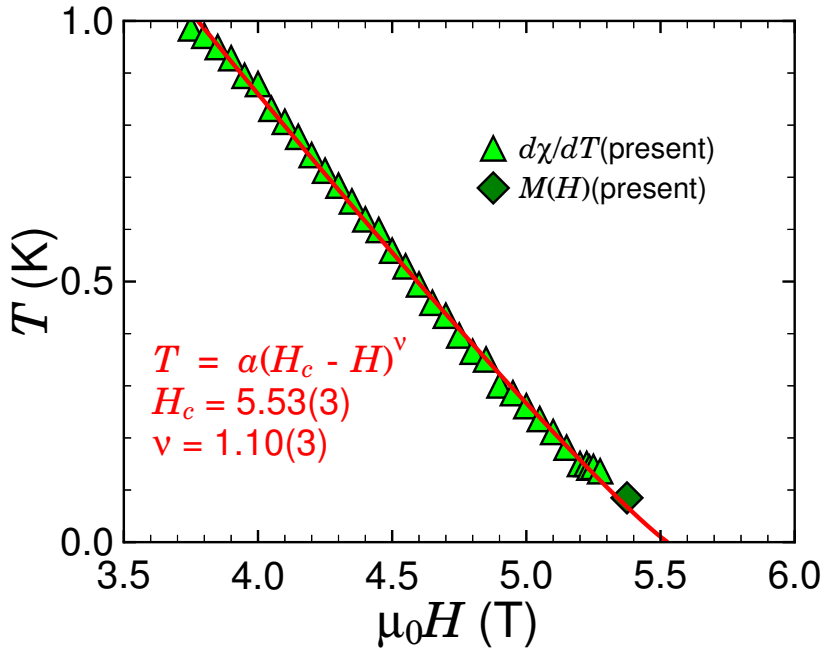

Figure 5.23: Fitting result of the function $T = a(H_c - H)^{\nu}$ with the phase boundary defined from $d\chi/dT$ below 1 K (solid line). Best fitting yields $H_c = 5.53(3)$ T and $\nu = 1.10(3)$. Diamond is the critical field determined from d^2M/d^2H at 80 mK.

The $\nu = 1$ behavior can also be observed on the phase boundary determined from $C(T)$. Figure 5.24 shows the obtained fitting parameters for $C(T)$, H_c and ν, with varying ΔT from 0.3 K to 0.6 K. Unfortunately, the error bars in the minimum window, $\Delta T = 0.3$ K, are relatively large probably because the fitting is done using only a few points of the data. However, it can be said that the whole behavior of the critical field and exponent is very similar to the one from the $\chi(T)$ data (Fig. 5.18) within the error bars.

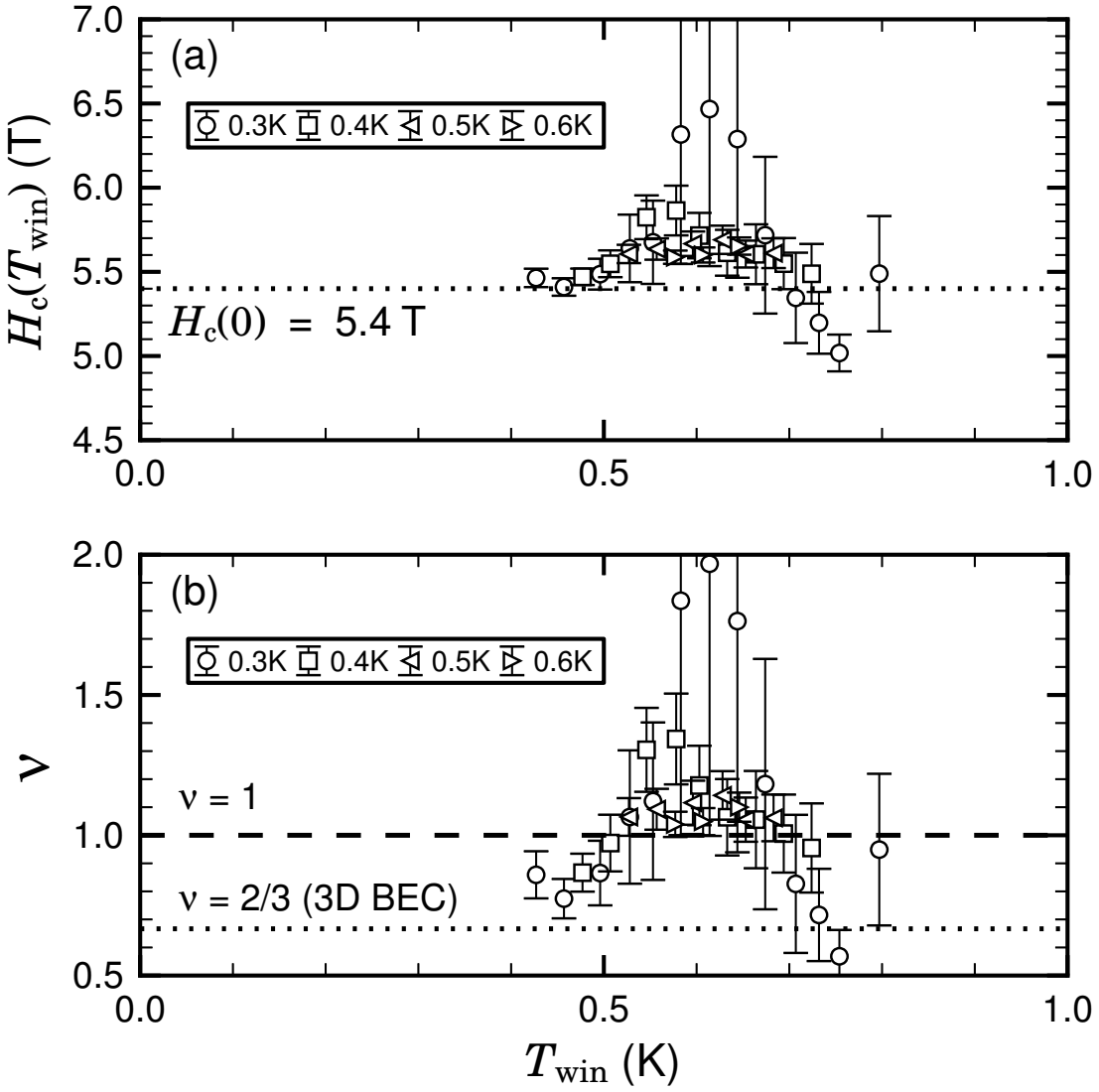

Figure 5.24: (a) The critical field H_c and (b) the exponent ν vary with the midpoint of the temperature window $T_{\rm win}$, which are derived from the sliding-window technique, applied to the phase boundary determined from $C(T)$. Different symbols denote the different temperature windows ΔT from 0.3 K to 0.6 K (see text). All the error bars represent fitting errors of the least squares method.

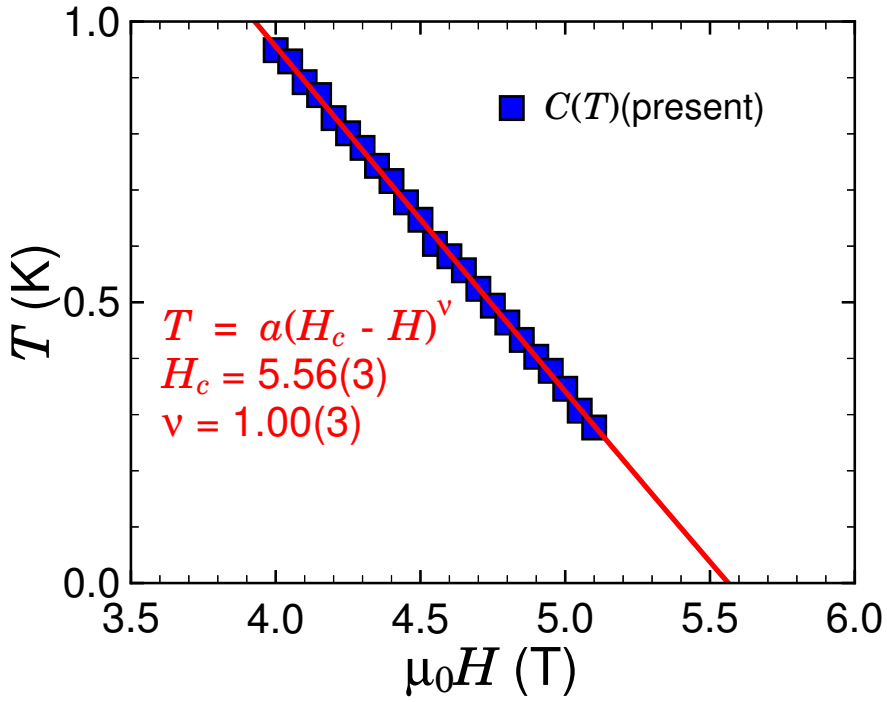

Figure 5.25: Fitting result of the function $T = a(H_c - H)^{\nu}$ with the phase boundary determined from $C(T)$ (solid line). Best fit yields $H_c = 5.56(3)$ T and $\nu = 1.00(3)$.

As shown in Fig. 5.25, the best fitting of the function $T \sim |H_c(T) - H_c(0)|^{\nu}$ to all the data of the phase boundary from $C(T)$ yields $H_c(0) = 5.56(3)$ T and $\nu = 1.00(3)$. These parameters are in excellently excellent agreement with the linear fit applied to the boundary from $\chi(T)$ between 0.5 K and 1 K as described above.

Judging from these analyses of the critical exponent, the $\nu = 1$ region is considered to be universal for the phase boundary of 3-I-V near the saturation field H_c. We will discuss possible causes of this $\nu = 1$ behavior in the next section.

5.3.5 Possible Cause of the $\nu = 1$ Behavior

As a cause of the nontrivial critical exponent $\nu = 1$, one may expect the Kosterlitz-Thouless (KT) transition [72, 73], which belongs to the 2D BEC universality class although the power law is subject to a logarithmic correction [18, 74]. In the case of the KT transition, it has been predicted that the specific heat has a large peak above T_c due to the unbinding of vortices, followed by only an weak anomaly at T_c [75–77]. This situation is not applicable to the case of 3-I-V because T_c determined from the peak anomaly of $C(T)$ is close to the one determined from the data of $\chi(T)$.

We notice that a theoretical study for quasi-one-dimensional ferromagnets with weak antiferromagnetic couplings predicts that a crossover of the critical exponent of a phase boundary from the conventional 3D BEC exponent $\phi = 3/2$ to $\phi = 1$ ($\phi = 1/\nu$) as moving away from the saturation field H_c [33]. For the $\nu = 1$ region to exist, inter-chain interactions, or effective interactions between magnons, must be small enough compared with intra-chain

couplings. This situation is analogous to the strong-leg type FM-leg ladder.

Although 3-I-V contains the relatively large antiferromagntic couplings, i.e., the rung interactions $J_{\rm rung} = 5.8\,{\rm K}$, between the ferromagnetic chains (legs) $J_{\rm leg} = -11.6\,{\rm K}$, it might be possible to satisfy the conditions discussed in Ref. 33 from two points of view. First, a spin-1/2 ferromagnetic-leg ladder can be mapped onto a spin-1/2 ferromagnetic chain with an easy-plane anisotropy in a certain condition [48]. This means that we would have to consider only the weak inter-ladder couplings. However, as discussed in Ref. 48, the mapping could be relevant in the case of strong rung type and near the lower critical field, where a spin gap is destroyed. It is then an open question whether the mapping can apply to strong leg type near the saturation field as 3-I-V. Second, the frustration of intra- and inter-ladder couplings in 3-I-V could make the effective interactions between the legs weaker. In particular, the intra-ladder coupling predicted by the MO calculations is ferromagnetic (Fig. 5.5), so that it could weaken the effective antiferromagnetic rung interactions (similar situation is considered in the case of CuPzN in Chapter 3, Section 3.1.2). Although these assumptions need theoretical supports, the unconventional critical exponent $\nu = 1$ in 3-I-V must reflect unique characteristics of the ferromagnetic-leg ladder.

5.4 Summary

We have determined the critical exponent ν of the 3D ordering phase boundary near the saturation field H_c on the spin-1/2 ferromagnetic-leg ladder 3-I-V, using dc magnetization and specific-heat measurements. Using the sliding-window fitting technique, we find the nontrivial critical exponent $\nu = 1$, different from the conventional 3D BEC exponent $\nu = 2/3$, on the phase boundary determined from $\chi(T)$ near H_c. The $\nu = 1$ region is also observed on the boundary determined from the temperature dependence of the specific heat $C(T)$. The nontrivial critical exponent $\nu = 1$ could be attributed to the 1D nature of the strong-leg-type ferromagnetic-leg ladder. 3-I-V would thus provide a new model to study novel BEC physics of magnons on quasi-1D systems containing ferromagnetic interactions.

Chapter 6

Conclusion

Quantum critical phenomena at magnetic-field-induced QCPs have been investigated on three (quasi-)1D quantum magnets, CuPzN, 3-Br-4-F-V, and 3-I-V, by means of dc magnetization and specific-heat measurements at low temperatures. In this chapter, obtained results are summarized with focusing on the characteristics of the QCPs on these materials.

In the practically perfect 1D spin-1/2 Heisenberg antiferromagnet CuPzN, we have performed the magnetization measurements near the saturation field $H_s = 13.97\,\mathrm{T}$ down to 39 mK, which is comparable to the predicted value of the inter-chain interactions $J' \sim 0.046\,\mathrm{K}$. Comparison of the obtained magnetization curves with the exact Bethe-ansatz calculations at zero temperature indicates that no effect of J' appears even at 39 mK. The obtained magnetization curves can also be scaled in wide temperature range by a universal relation derived from the phenomenological theory for 1D free fermion gas. These findings support the virtually perfect one dimensionality of CuPzN and confirm the validity of the phenomenological theory for real 1D magnets.

We have discussed the critical exponents ν near the critical field H_c, derived from the 3D ordering phase boundary $T \propto |H_c(T) - H_c(0)|^{\nu}$, on the spin-1/2 ferromagnetic-leg (FM-leg) ladders, 3-Br-4-F-V and 3-I-V, in the light of 3D Bose-Einstein condensation (BEC) universality and quasi-one dimensionality.

The strong-rung-type FM-leg ladder 3-Br-4-F-V has two QCPs, the lower critical field $H_{c1} \sim 5\,\mathrm{T}$ and the saturation field $H_{c2} \sim 9\,\mathrm{T}$. The 3D ordering phase boundary $T_c(H)$ near the QCPs has been defined from the temperature derivative of the magnetic susceptibility $d\chi(T)/dT$ or $d(T\chi(T))/dT$ and the temperature dependence of the specific heat $C(T)$. There exists a disparity between the phase boundaries obtained from $d\chi(T)/dT$ and $C(T)$ measured on different samples, which could be attributed to a difference in the strain condition within the samples. Nevertheless, the behavior of the critical exponents ν obtained from the temperature-window technique is found to show no sample dependence. The exponents near both sides of the QCPs are in good agreement with the 3D BEC universality class, $\nu = 2/3$, at low temperatures. The 3D BEC exponent is considered to be universal on the 3D ordering phase boundary of 3-Br-4-F-V. This is the first observation as a spin-1/2 FM-leg ladder and gives one of a few experimental tests for the critical exponent ν near H_{c2}.

The strong-leg-type FM-leg ladder 3-I-V has only one QCP, the saturation field $H_c \sim 5.5\,\mathrm{T}$, different from 3-Br-4-F-V. We have defined the 3D ordering phase boundary $T_c(H)$ near the QCP from the temperature dependence of the magnetic susceptibility $\chi(T)$ and the

temperature dependence of the specific heat $C(T)$. In order to check whether the difference of the definitions of $T_c(H)$ would affect the critical exponent ν, anomalies in $d\chi(T)/dT$ and $d(T\chi)/dT$ have also been examined. The critical exponent ν of 3-I-V has been obtained by the sliding-window technique. Irrespective of the definitions of $T_c(H)$, there exists nontrivial $\nu = 1$ region near 0.5 K slightly off the saturation field, different from the conventional 3D BEC $\nu = 2/3$. The difference of the critical exponent from the case of 3-Br-4-F-V could be attributed to the "degree" of one dimensionality, i.e., strong-rung (3-Br-4-F-V) or strong-leg (3-I-V) type, and the frustration of the intra- and inter-ladder couplings. This situation is analogous to the theoretical study for quasi-one-dimensional ferromagnets with weak antiferromagnetic couplings [33], which has predicted that a $\nu = 1$ region appears on the phase boundary as slightly moving away from H_c and strong one dimensionality is essential for the existence of the $\nu = 1$ region. Since the $\nu = 1$ region has never been found in the candidates mentioned in Ref. 33, 3-I-V is promising as a new candidate for the theoretical prediction.

Thus, CuPzN and 3-Br-4-F-V demonstrate the universality of the quantum critical phenomena predicted by a mapping of quantum spins onto quasi-particle gases; CuPzN is an ideal model compound for the phenomenological theory of 1D free fermion gas, and 3-Br-4-F-V is found to be a new model compound for 3D BEC in quantum magnets. On the other hand, 3-I-V demonstrates that FM-leg ladders could lead to a novel quantum criticality beyond the 3D BEC universality. These facts provide new insight into a role of one dimensionality in the quantum critical phenomena on various real quantum magnets including 3-Cl-4-F-V [44, 49], another FM-leg ladder synthesized to date.

Appendices

A.1 Temperature Dependence of the Magnetic Susceptibility of 3-Br-4-F-V

For clarity, Fig. 4.5 (p. 33), Fig. 4.6 (p. 34), and Fig. 4.7 (p. 35) show a part of the data used for determining the phase boundary in Fig. 4.10 (p. 38) (Chapter 4). The rest of the data is shown in Fig. A.1.1, Fig. A.1.2, and Fig. A.1.3.

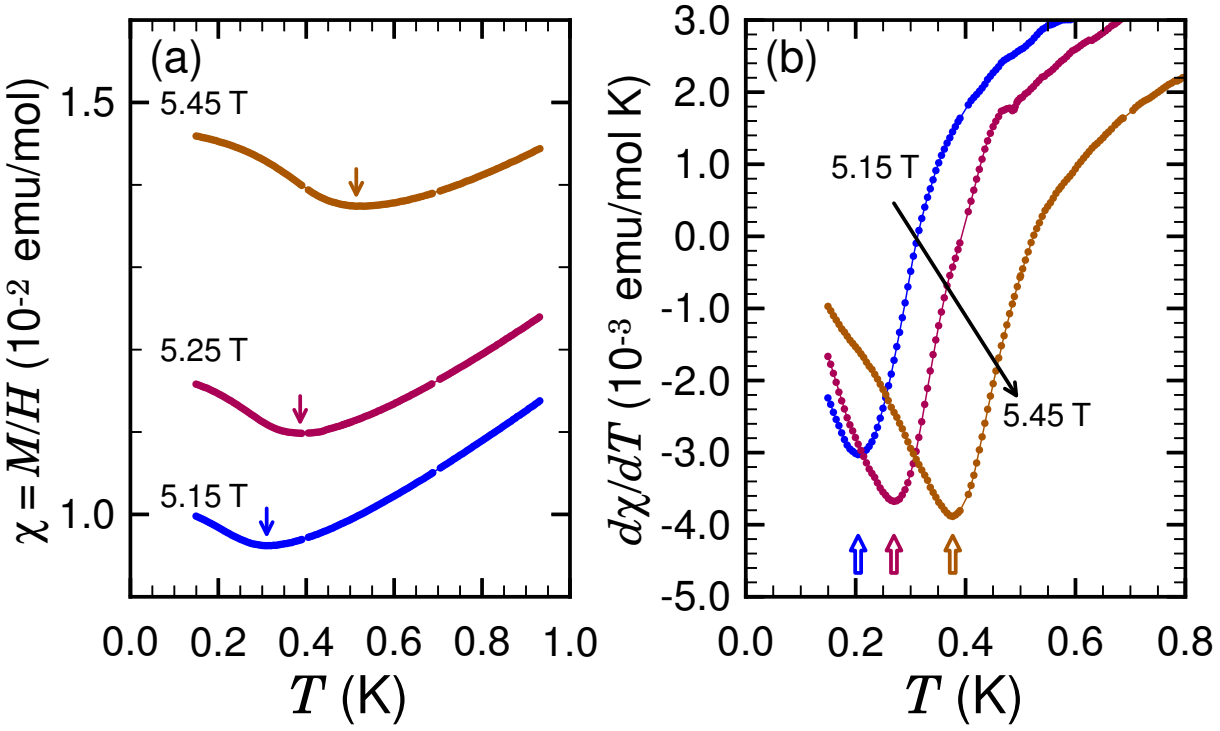

Figure A.1.1: (a) Temperature dependence of the magnetic susceptibility $\chi = M/H$ at 5.15 T, 5.25 T, and 5.45 T. Arrows indicate the temperature T_{ex} at which χ takes the nontrivial minimum. (b) Temperature derivative of χ calculated from the data on (a). Open arrows show the transition temperature, T_c, defined from the minimum of the kink anomaly.

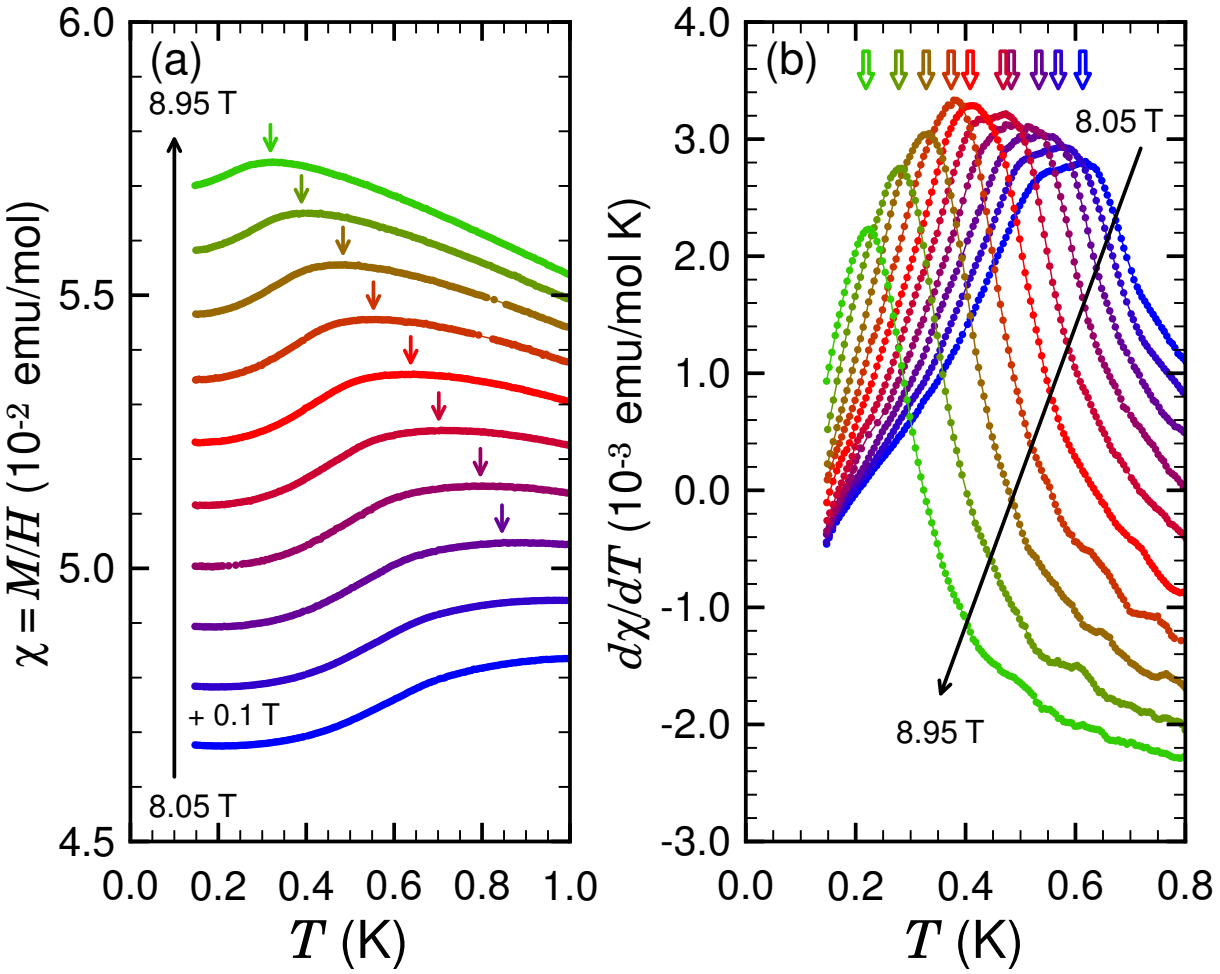

Figure A.1.2: (a) Temperature dependence of the magnetic susceptibility $\chi = M/H$ in several magnetic fields between 8.05 T and 8.95 T. Arrows indicate the temperature T_{ex} at which χ takes the nontrivial maximum. (b) Temperature derivative of χ calculated from the data on (a). Open arrows show the transition temperature, T_c, defined from the maximum of the kink anomaly.

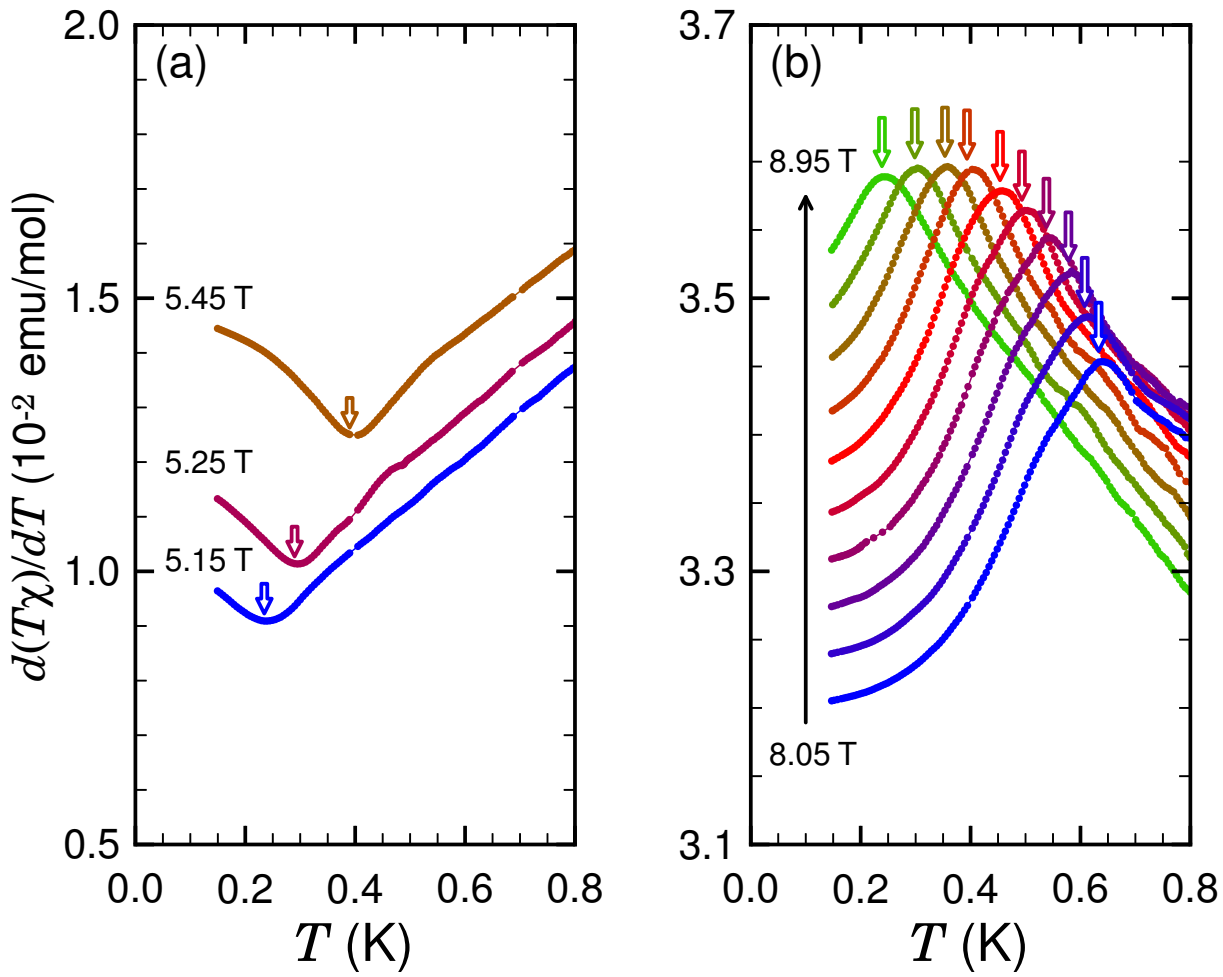

Figure A.1.3: (a) Temperature derivative of $T\chi$ calculated from the data on Fig. A.1.1(a). Open arrow shows the transition temperature defined from the minimum of the dip anomaly of each curve. (b) Temperature derivative of $T\chi$ calculated from the data on Fig. A.1.2(a). Open arrow shows the transition temperature defined from the maximum of the peak anomaly of each curve.

A.2 Temperature Dependence of the Magnetic Susceptibility and the Specific Heat of 3-I-V

For clarity, Fig. 5.10 (p. 49) and Fig. 5.13 (p. 52) show a part of the data used for determining the phase boundary in Fig. 5.14 (p. 53) (Chapter 5). Fig. 5.11 (p. 50) and Fig. 5.12 (p. 51) also show a part of the data for Fig. 5.15 (p. 54) and Fig. 5.16 (p. 54), respectively. The rest of the data is shown in Fig. A.2.4, Fig. A.2.5, Fig. A.2.6, and Fig. A.2.7.

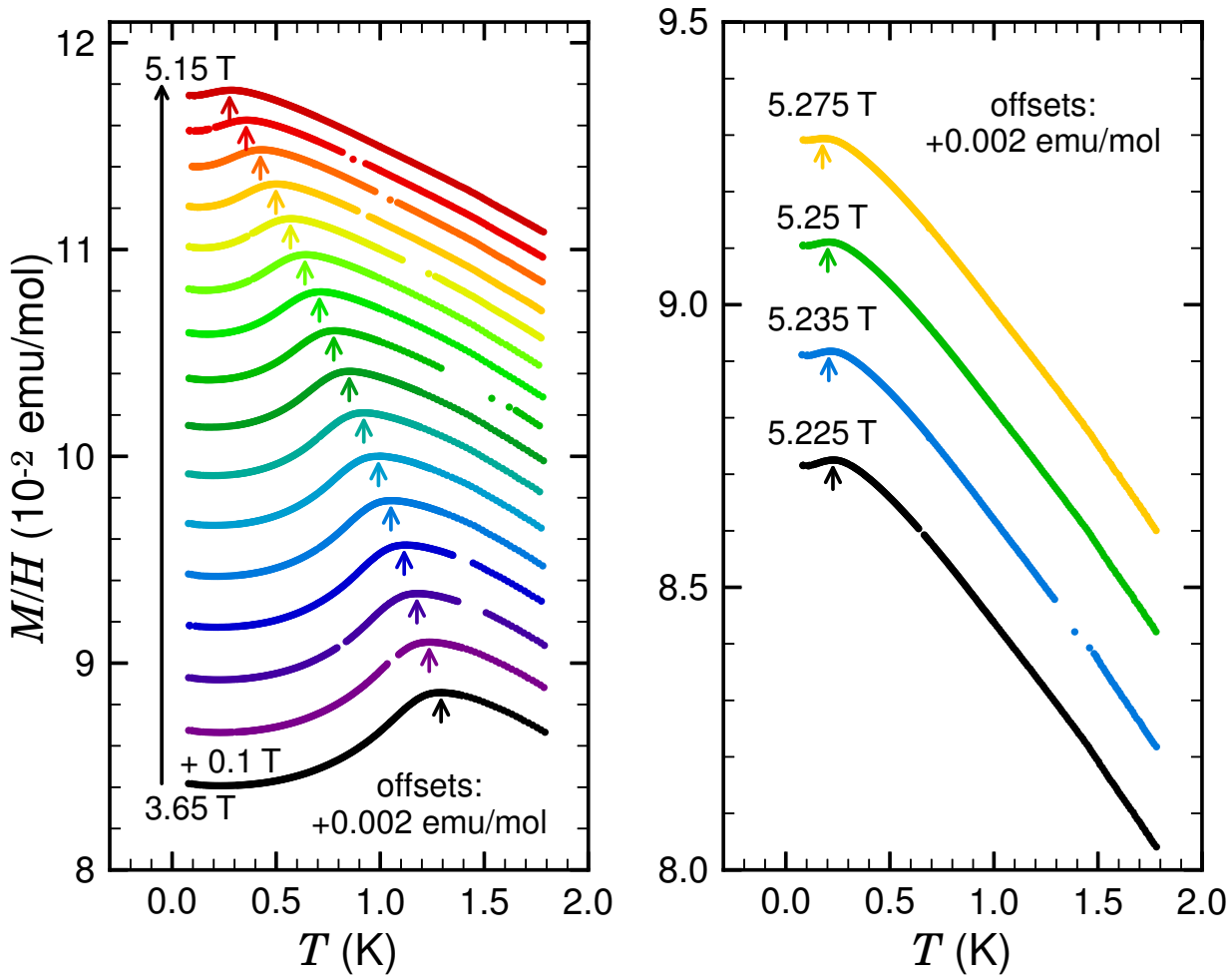

Figure A.2.4: Temperature dependence of the magnetic susceptibility M/H at several magnetic fields between 3.65 T and 5.15 T (left panel). Right panel shows the one near the saturation field H_c. For clarity, each curve is shifted by +0.002 emu/mol more than the one just below on each panel. Arrows denote cusp-like anomalies indicating the 3D ordering.

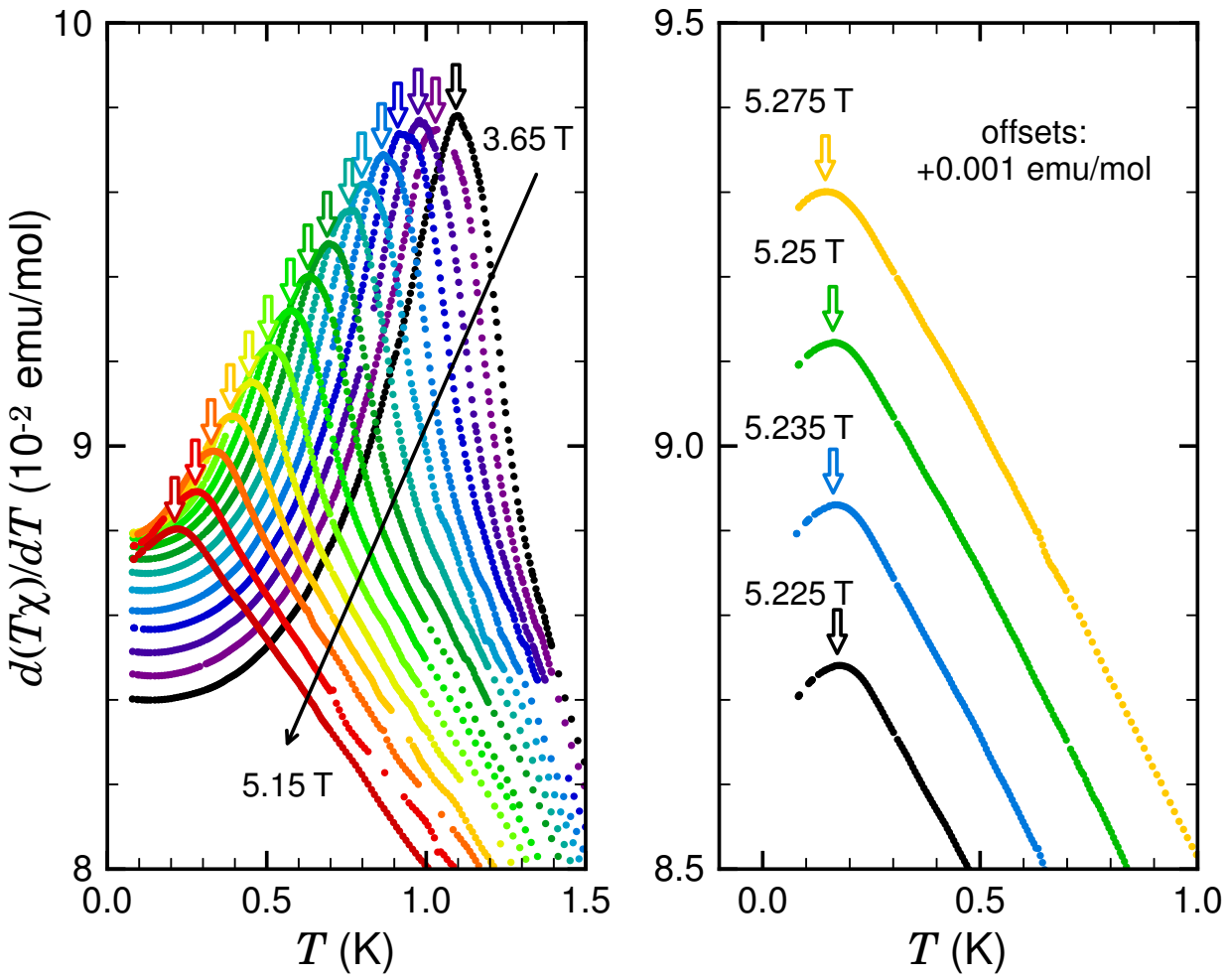

Figure A.2.5: Temperature derivative of $T\chi$ calculated from the data on each panel of Fig. A.2.4 ($d(T\chi)/dT$). Arrows denote peak anomalies.

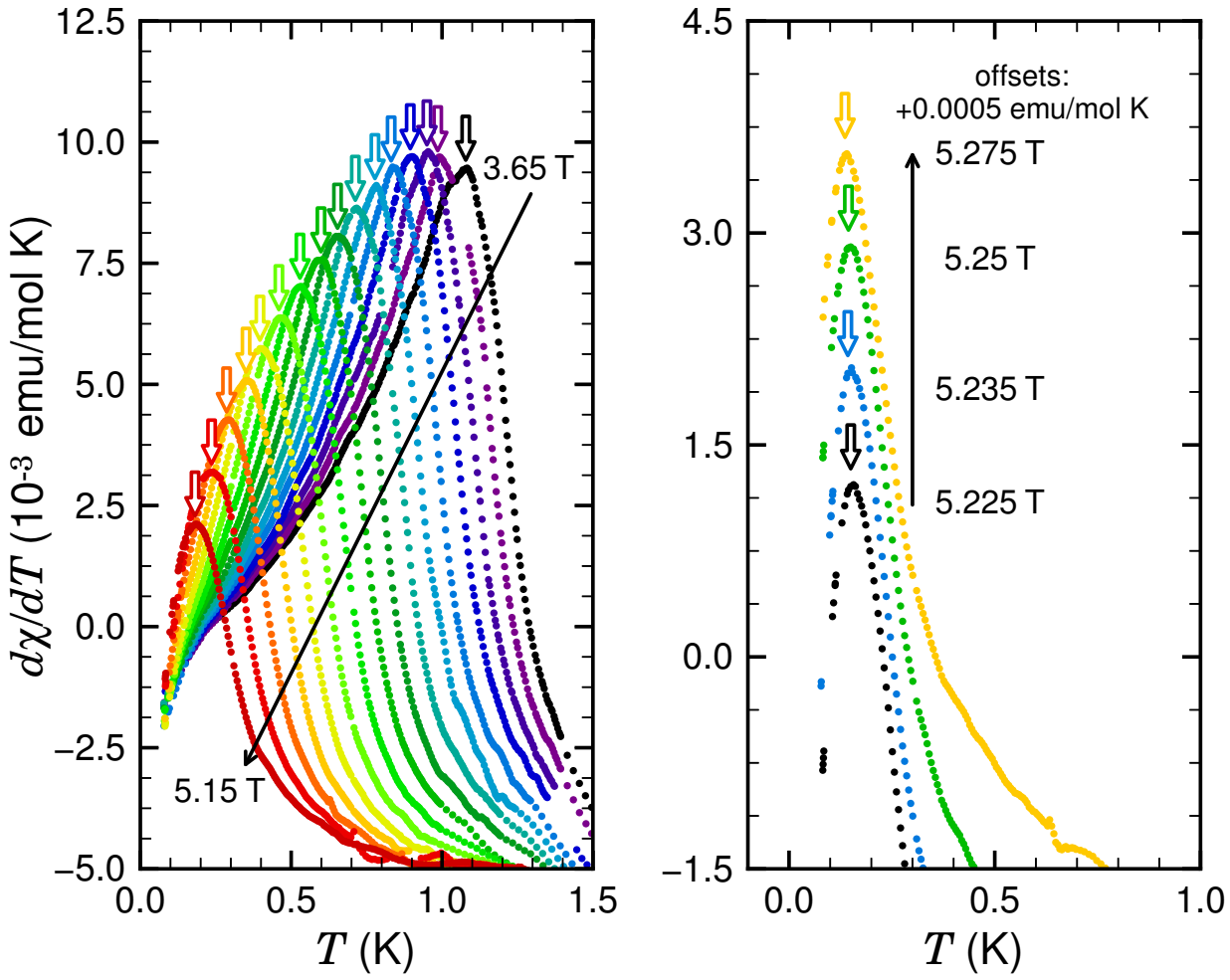

Figure A.2.6: Temperature derivative of χ calculated from the data on each panel of Fig. A.2.4 ($d\chi/dT$). Arrows denote peak anomalies.

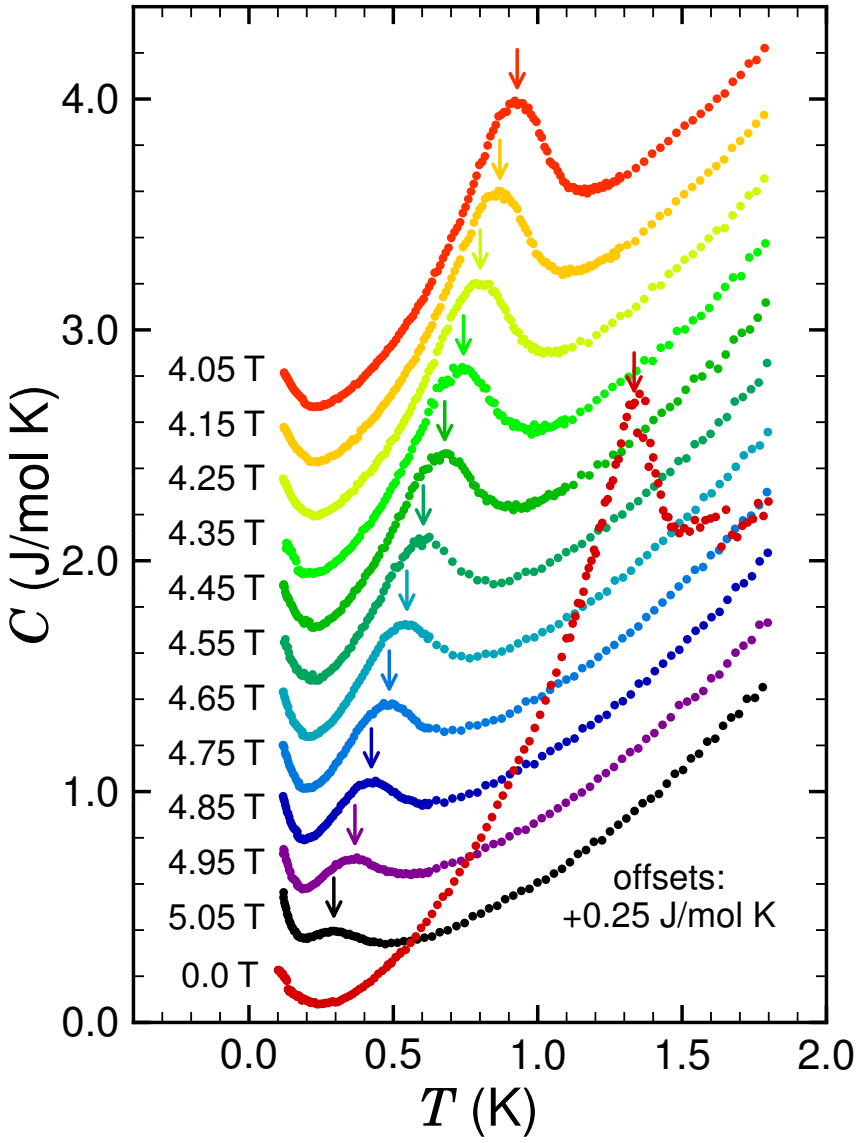

Figure A.2.7: Temperature dependence of the specific heat at 0 T and several magnetic fields between 4.05 T and 5.05 T. For clarity, each curve is shifted by +0.25 J/mol K more than the one just below. Arrows denote peak anomalies indicating the 3D ordering. The small jump near 1.7 K in the 0 T data is from the small difference of the quasi-adiabatic and relaxation methods.

A.3 Python Source Code for the Temperature-window Technique

In order to fit Eq. (4.4) to the phase boundary of 3-Br-4-F-V within the temperature window $0 \leq T \leq t_{\max}$ for several fixed ν's (Chapter 4, Section 4.3.4, p. 39), we employ the standard least-squares method with developing Python codes with the Numpy package as described below. Fitting for the critical exponent ν with fixing $H_{c1,2}(0)$ is also performed by similar source code.

```
#importing modules
import math, numpy as np ,scipy.optimize, re, os
from numpy import inf

#setting parameters
vlist=[0.6,0.64,0.68,0.72,0.76,0.8] #list of fixed critical exponents
Hm=7.0 #the magnetic field centered in the 3D ordering dome of 3-Br-4-F-V
parameter0=[0.536,4.9] #initial values for fitting

#definition of fitting function
def fit_funcHc(Hm,v):
    def _fitfuncHc(parameter,x,y):
        residual=parameter[0]*(1-((Hm-x)/(Hm-parameter[1]))**2)**v
        return residual-y
    return _fitfuncHc

#partial derivatives of the fitting function
def dfuncHc(Hm,v):
    def _dfuncHc(parameter,x,y):
        dev=[(1-((Hm-x)/(Hm-parameter[1]))**2)**v,-2*parameter[0]*v*((Hm-x)**2)*((
            Hm-parameter[1])**(-3))*(1-((Hm-x)/(Hm-parameter[1]))**2.)**(v-1)]
        return dev
    return _dfuncHc

#main
def main():

    #loading datafile which contains a pair of the magnetic field and the 3D ordering
        temperature
    dir = os.getcwd()
    tempdata=np.loadtxt(dir+<filename>,delimiter='\t')

    #sorting data
    if tempdata[0][0] < Hmax:
        tempdata=sorted(tempdata, key=lambda x:x[0])
```

```
34      else:
35          tempdata=sorted(tempdata, key=lambda x:x[0], reverse=True)
36
37      #fitting for the fixed critical exponents in the vlist array
38      for v in vlist:
39          #initializing values and arrays
40          i = 0
41          j = 0
42          param_output=[0.0 for i in range(len(tempdata))]
43          param_result=[0.0 for i in range(len(tempdata))]
44          covar_result=[0.0 for i in range(len(tempdata))]
45
46          #preparing inputfile
47          inputfile=<filename>
48          g = open(dir+inputfile, 'w')
49          g.write("#v={0}\n#tw (K)\t\'Hc\'\terror\n".format(v))
50
51          for i in range(2,len(tempdata)):
52          #preparing arrays of the data within the temperature window defined by the value i
53          # (tmax = tempdata[i][0])
54              Nx = np.array([tempdata[j][0] for j in range(0,i+1)],dtype=np.float64) #array of
                    the magnetic fields
55              Ny = np.array([tempdata[j][1] for j in range(0,i+1)],dtype=np.float64) #array of
                    the 3D ordering temperatures
56
57              #fitting by the least-squares method
58              param_output[i] = scipy.optimize.leastsq(fit_funcHc(Hmax,v), parameter0,args=(
                    Nx,Ny),Dfun=dfuncHc(Hmax,v),full_output=True,col_deriv=1,xtol=1.0e-9,
                    maxfev=1000)
59              param_result[i] = param_output[i][0] # results of fitting parameters
60              covar_result[i] = param_output[i][1] # covariant matrix
61
62              if (len(Ny) > len(parameter0)) and covar_result[i] is not None:
63                  s_sq = (fit_funcHc(Hmax,v)(param_result[i], Nx, Ny)**2).sum()/(len(Ny)-
                        len(parameter0))
64                  covar_result[i] = covar_result[i] * s_sq
65              else:
66                  covar_result[i] = inf
67
68              Hc=param_result[i][1] #result of the critical field for the temperature window
69
70              Hc_err=np.sqrt(covar_result[i][1][1]) #fitting error determined from the diagonal
                    component of the covariant matrix
71
72              #writing the fitiing results into the inputfile
```

```
73                g.write('%0.7g\t%0.7g\t%0.7g\n' % (tempdata[i][1],Hc,Hc_err))
74            g.close()
75
76    if __name__ == '__main__':
77        main()
```

A.4 Python Source Code for the Sliding-window Technique

In Chapter 5, Section 5.3.4 (p. 55), fitting of the power-law function $T \sim |H_c(T) - H_c(0)|^{\nu}$ with the phase boundary of 3-I-V by the sliding-window technique is performed with developing a Python code similar to Section A.3 as described below.

```
1   #importing modules
2   import math, numpy as np ,scipy.optimize, re, os
3   from numpy import inf
4
5   #setting parameters
6   windowlist=[0.3,0.4,0.5,0.6,0.7,0.8,0.9,1.0,1.1] #list of the temperature-window sizes
7   parameter0=[1.0,6.0,1.0] #initial values for fitting
8
9   #definition of fitting function
10  def fit_func(parameter,x,y):
11      residual=parameter[0]*(parameter[1]-x)**parameter[2]-y
12      return residual
13
14  #partial derivatives of the fitting function
15  def dfunc(parameter,x,y):
16      dev=[(parameter[1]-x)**parameter[2],parameter[0]*parameter[2]*(parameter[1]-x)**(
            parameter[2]-1),(parameter[0]*(parameter[1]-x)**parameter[2])*np.log(parameter
            [1]-x)]
17      return dev
18
19
20  #main
21  def main():
22      #loading datafile which contains a pair of the magnetic field and the 3D ordering
            temperature
23      dir = os.getcwd()
24      tempdata=np.loadtxt(dir+<filename>,delimiter='\t')
25
26      #sort data
27      tempdata=np.array(sorted(tempdata[tempdata[:,0]>2.8], key=lambda x:x[1]))
```

```
28
29      for win in windowlist:
30          #preparing inputfile
31          inputfile=<filename>
32          g = open(dir+'/'+inputfile, 'w')
33          g.write("#window={0} K\n#Twin (K)\ta\taerr\tHc\tHc_err\tv\tv_err\n".format(
                win))
34          i = 0
35          j = 0
36
37          for i in range(len(tempdata)):
38              #setting a temperature window at a certain temperature on the phase boundary
39              if tempdata[i][1]+win > tempdata[-1][1]: break
40              else:
41                  winarr= np.logical_and(tempdata[:,1] >= tempdata[i][1], tempdata[:,1] <=
                        tempdata[i][1]+win)
42
43                  #preparing arrays of the data within the temperature window
44                  Nx = tempdata[winarr,0]
45                  Ny = tempdata[winarr,1]
46
47                  #fitting by the least-squares method
48                  param_output = scipy.optimize.leastsq(fit_func, parameter0,args=(Nx,Ny),
                        Dfun=dfunc,full_output=True,col_deriv=1,xtol=1.0e-9,maxfev=1000)
49                  param_result = param_output[0] # results of fitting parameters
50                  covar_result = param_output[1] # covariant matrix
51
52                  if (len(Ny) > len(parameter0)) and covar_result is not None:
53                      s_sq = (fit_func(param_result, Nx, Ny)**2).sum()/(len(Ny)-len(
                            parameter0))
54                      covar_result = covar_result * s_sq
55                  else:
56                      covar_result = inf
57
58                  A=param_result[0]# result of the fitting coefficient
59                  B=param_result[1]# result of the critical field
60                  C=param_result[2]# result of the critical exponent
61
62                  #fitting error determined from the diagonal components of the covariant
                        matrix
63                  Aerr=np.sqrt(covar_result[0][0])
64                  Berr=np.sqrt(covar_result[1][1])
65                  Cerr=np.sqrt(covar_result[2][2])
66
67                  #writing the fitiing results into the inputfile
```

```
68                      g.write('%0.9g\t%0.9g\t%0.9g\t%0.9g\t%0.9g\t%0.9g\t%0.9g\n' % (
                            tempdata[i][1]+win/2,A,Aerr,B,Berr,C,Cerr))
69          g.close()
70
71  if __name__ == '__main__':
72      main()
```

Bibliography

[1] S. Sachdev, *Quantum Phase Transitions (Second Edition)* (Cambridge Univ. Press, Cambridge, UK, 2011).

[2] K. Kubo and H. Tanaka, *Magnetization I* (Asakura-shoten, Tokyo, Japan, 2008), [in Japanese].

[3] T. Giamarchi, *Quantum Physics in One Dimension* (Oxford University Press, Oxford, UK, 2004).

[4] H. Bethe, Z. Phys. **71**, 205 (1931).

[5] N. Bogoliubov, A. Izergin, and V. Korepin, Nucl. Phys. B **275**, 687 (1986).

[6] C.-N. Yang and C.-P. Yang, Phys. Rev. **150**, 321 (1966).

[7] R. B. Griffiths, Phys. Rev. **133**, A768 (1964).

[8] F. D. M. Haldane, J. Phys. C **14**, 2585 (1981).

[9] F. D. M. Haldane, Phys. Rev. Lett. **45**, 1358 (1980).

[10] G. Müller, H. Thomas, H. Beck, and J. C. Bonner, Phys. Rev. B **24**, 1429 (1981).

[11] F. D. M. Haldane, Phys. Rev. Lett. **47**, 1840 (1981).

[12] I. Affleck, Phys. Rev. B **43**, 3215 (1991).

[13] S. Sachdev, T. Senthil, and R. Shankar, Phys. Rev. B **50**, 258 (1994).

[14] Y. Maeda, C. Hotta, and M. Oshikawa, Phys. Rev. Lett. **99**, 057205 (2007).

[15] Y. Kono, T. Sakakibara, C. P. Aoyama, C. Hotta, M. M. Turnbull, C. P. Landee, and Y. Takano, Phys. Rev. Lett. **114**, 037202 (2015).

[16] T. Lancaster, S. J. Blundell, M. L. Brooks, P. J. Baker, F. L. Pratt, J. L. Manson, C. P. Landee, and C. Baines, Phys. Rev. B **73**, 020410(R) (2006).

[17] T. Matsubara and H. Matsuda, Prog. Theor. Phys. **16**, 569 (1956).

[18] V. Zapf, M. Jaime, and C. D. Batista, Rev. Mod. Phys. **86**, 563 (2014).

[19] T. Giamarchi, C. Rüegg, and O. Tchernyshyov, Nat. Phys. **4**, 198 (2008).

[20] M. Tachiki and T. Yamada, J. Phys. Soc. Jpn. **28**, 1413 (1970).

[21] T. Nikuni, M. Oshikawa, A. Oosawa, and H. Tanaka, Phys. Rev. Lett. **84**, 5868 (2000).

[22] N. Kawashima, J. Phys. Soc. Jpn. **73**, 3219 (2004).

[23] O. Nohadani, S. Wessel, B. Normand, and S. Haas, Phys. Rev. B **69**, 220402 (2004).

[24] M. Crisan, I. Ţifrea, D. Bodea, and I. Grosu, Phys. Rev. B **72**, 184414 (2005).

[25] T. Moriya, Phys. Rev. **120**, 91 (1960).

[26] H. Tanaka, F. Yamada, T. Ono, T. Sakakibara, Y. Uwatoko, A. Oosawa, K. Kakurai, and K. Goto, J. Magn. Magn. Mater. **310**, 1343 (2007).

[27] F. Yamada, T. Ono, H. Tanaka, G. Misguich, M. Oshikawa, and T. Sakakibara, J. Phys. Soc. Jpn. **77**, 013701 (2008).

[28] S. E. Sebastian, P. A. Sharma, M. Jaime, N. Harrison, V. Correa, L. Balicas, N. Kawashima, C. D. Batista, and I. R. Fisher, Phys. Rev. B **72**, 100404 (2005).

[29] S. E. Sebastian, N. Harrison, C. D. Batista, L. Balicas, M. Jaime, P. A. Sharma, N. Kawashima, and I. R. Fisher, Nature **441**, 617 (2006).

[30] C. D. Batista, J. Schmalian, N. Kawashima, P. Sengupta, S. E. Sebastian, N. Harrison, M. Jaime, and I. R. Fisher, Phys. Rev. Lett. **98**, 257201 (2007).

[31] O. Rösch and M. Vojta, Phys. Rev. B **76**, 180401 (2007).

[32] N. Laflorencie and F. Mila, Phys. Rev. Lett. **102**, 060602 (2009).

[33] A. V. Syromyatnikov, Phys. Rev. B **75**, 134421 (2007).

[34] H. Kawamura, J. Phys. Soc. Jpn. **55**, 2095 (1986).

[35] V. O. Garlea, A. Zheludev, K. Habicht, M. Meissner, B. Grenier, L.-P. Regnault, and E. Ressouche, Phys. Rev. B **79**, 060404 (2009).

[36] M. B. Stone, C. Broholm, D. H. Reich, O. Tchernyshyov, P. Vorderwisch, and N. Harrison, Phys. Rev. Lett. **96**, 257203 (2006).

[37] K. Ninios, T. Hong, T. Manabe, C. Hotta, S. N. Herringer, M. M. Turnbull, C. P. Landee, Y. Takano, and H. B. Chan, Phys. Rev. Lett. **108**, 097201 (2012).

[38] M. Jeong, H. Mayaffre, C. Berthier, D. Schmidiger, A. Zheludev, and M. Horvatić, Phys. Rev. Lett. **111**, 106404 (2013).

[39] B. C. Watson, V. N. Kotov, M. W. Meisel, D. W. Hall, G. E. Granroth, W. T. Montfrooij, S. E. Nagler, D. A. Jensen, R. Backov, M. A. Petruska, G. E. Fanucci, and D. R. Talham, Phys. Rev. Lett. **86**, 5168 (2001).

[40] C. Rüegg, K. Kiefer, B. Thielemann, D. F. McMorrow, V. Zapf, B. Normand, M. B. Zvonarev, P. Bouillot, C. Kollath, T. Giamarchi, S. Capponi, D. Poilblanc, D. Biner, and K. W. Krämer, Phys. Rev. Lett. **101**, 247202 (2008).

[41] M. Greven, R. J. Birgeneau, and U. J. Wiese, Phys. Rev. Lett. **77**, 1865 (1996).

[42] T. Giamarchi and A. M. Tsvelik, Phys. Rev. B **59**, 11398 (1999).

[43] S. Wessel, M. Olshanii, and S. Haas, Phys. Rev. Lett. **87**, 206407 (2001).

[44] H. Yamaguchi, H. Miyagai, T. Shimokawa, K. Iwase, T. Ono, Y. Kono, N. Kase, K. Araki, S. Kittaka, T. Sakakibara, T. Kawakami, K. Okunishi, and Y. Hosokoshi, J. Phys. Soc. Jpn. **83**, 033707 (2014).

[45] A. K. Kolezhuk and H. J. Mikeska, Phys. Rev. B **53**, R8848 (1996).

[46] T. Vekua, G. I. Japaridze, and H.-J. Mikeska, Phys. Rev. B **67**, 064419 (2003).

[47] K. Hijii, A. Kitazawa, and K. Nomura, Phys. Rev. B **72**, 014449 (2005).

[48] T. Vekua, G. I. Japaridze, and H.-J. Mikeska, Phys. Rev. B **70**, 014425 (2004).

[49] H. Yamaguchi, K. Iwase, T. Ono, T. Shimokawa, H. Nakano, Y. Shimura, N. Kase, S. Kittaka, T. Sakakibara, T. Kawakami, and Y. Hosokoshi, Phys. Rev. Lett. **110**, 157205 (2013).

[50] H. Yamaguchi, H. Miyagai, M. Yoshida, M. Takigawa, K. Iwase, T. Ono, N. Kase, K. Araki, S. Kittaka, T. Sakakibara, T. Shimokawa, T. Okubo, K. Okunishi, A. Matsuo, and Y. Hosokoshi, Phys. Rev. B **89**, 220402 (2014).

[51] H. Yamaguchi, H. Miyagai, Y. Kono, S. Kittaka, T. Sakakibara, K. Iwase, T. Ono, T. Shimokawa, and Y. Hosokoshi, Phys. Rev. B **91**, 125104 (2015).

[52] T. Sakakibara, H. Mitamura, T. Tayama, and H. Amitsuka, Jpn. J. Appl. Phys. **33**, 5067 (1994).

[53] Y. Shimura, Ph.D. thesis, The University of Tokyo, Tokyo, Japan (2013).

[54] T. Sugiyama, Master's thesis, The University of Tokyo, Tokyo, Japan (2012), [in Japanese].

[55] NINS, National Astronomical Observatory of Japan, ed., *Chronological Scientific Tables* (MARUZEN, Tokyo, Japan, 2016), http://www.rikanenpyo.jp/, [in Japanese].

[56] S. Kittaka, *Textbook of J-Physics Summer School* (J-Physics: Physics of Conductive Multipole Systems, Koyasan Univ., Japan, 2016), p. 67, [unpublished, in Japanese].

[57] Scientific Instruments, Inc., http://www.scientificinstruments.com/product-detail/model-ro-6001k-ruthenium-oxide-rtd/, (January 2017).

[58] A. Santoro, A. D. Mighell, and C. W. Reimann, Acta Crystallogr. **B26**, 979 (1970).

[59] P. R. Hammar, M. B. Stone, D. H. Reich, C. Broholm, P. J. Gibson, M. M. Turnbull, C. P. Landee, and M. Oshikawa, Phys. Rev. B **59**, 1008 (1999).

[60] G. Mennenga, L. De Jongh, W. Huiskamp, and J. Reedijk, J. Magn. Magn. Mater. **44**, 89 (1984).

[61] A. Klümper, Z. Phys B **91**, 507 (1993).

[62] A. Klümper, Eur. Phys. J. B **5**, 677 (1998).

[63] O. A. Starykh, H. Katsura, and L. Balents, Phys. Rev. B **82**, 014421 (2010).

[64] J. Jornet-Somoza, M. Deumal, M. Robb, C. Landee, M. Turnbull, R. Feyerherm, and J. Novoa, Inorg. Chem. **49**, 1750 (2010).

[65] K. Gloos, C. Mitschka, F. Pobell, and P. Smeibidl, Cryogenics **30**, 14 (1990).

[66] M. Jeong and H. M. Rønnow, Phys. Rev. B **92**, 180409 (2015).

[67] M. E. Fisher, Philos. Mag. **7**, 1731 (1962).

[68] E. E. Bragg and M. S. Seehra, Phys. Rev. B **7**, 4197 (1973).

[69] T. Radu, H. Wilhelm, V. Yushankhai, D. Kovrizhin, R. Coldea, Z. Tylczynski, T. Lühmann, and F. Steglich, Phys. Rev. Lett. **95**, 127202 (2005).

[70] T. Radu, H. Wilhelm, V. Yushankhai, D. Kovrizhin, R. Coldea, Z. Tylczynski, T. Lühmann, and F. Steglich, Phys. Rev. Lett. **96**, 189704 (2006).

[71] V. S. Zapf, D. Zocco, B. R. Hansen, M. Jaime, N. Harrison, C. D. Batista, M. Kenzelmann, C. Niedermayer, A. Lacerda, and A. Paduan-Filho, Phys. Rev. Lett. **96**, 077204 (2006).

[72] J. M. Kosterlitz and D. J. Thouless, J. Phys. C: Solid State Phys. **6**, 1181 (1973).

[73] J. M. Kosterlitz, J. Phys. C: Solid State Phys. **7**, 1046 (1974).

[74] D. S. Fisher and P. C. Hohenberg, Phys. Rev. B **37**, 4936 (1988).

[75] S. Miyashita, H. Nishimori, A. Kuroda, and M. Suzuki, Prog. Theor. Phys. **60**, 1669 (1978).

[76] J. Tobochnik and G. V. Chester, Phys. Rev. B **20**, 3761 (1979).

[77] H.-Q. Ding and M. S. Makivić, Phys. Rev. B **42**, 6827 (1990).

Publication List

First Author

1. Y. Kono, T. Sakakibara, C. P. Aoyama, C. Hotta, M. M. Turnbull, C. P. Landee, and Y. Takano, *"Field-Induced Quantum Criticality and Universal Temperature Dependence of the Magnetization of a Spin-1/2 Heisenberg Chain"*, Phys. Rev. Lett. **114**, 037202 (2015).

2. Y. Kono, S. Kittaka, T. Sakakibara, H. Yamaguchi, and Y. Hosokoshi, *"Low temperature magnetic properties of a new quasi-one-dimensional organic magnet α-2-Cl-4-F-V"*, Phys. Procedia **75**, 679 (2015).

3. Yohei Kono, Toshiro Sakakibara, Christopher Aoyama, Mark M. Turnbull, Christopher Landee, Yasumasa Takano, *"Magnetization Study of the Quantum Critical Behavior of the One Dimensional Spin-1/2 Heisenberg Antiferromagnet CuPzN"*, JPS Conf. Proc. **3**, 012015 (2014).

Co-author

1. H. Takatsu, S. Onoda, S. Kittaka, A. Kasahara, Y. Kono, T. Sakakibara, Y. Kato, B. Fâk, J. Ollivier, J. W. Lynn, T. Taniguchi, M. Wakita, H. Kadowaki, *"Quadrupole Order in the Frustrated Pyrochlore $Tb_{2+x}Ti_{2-x}O_{7+y}$"*, Phys. Rev. Lett. **116**, 217201 (2016).

2. H. Yamaguchi, Y. Shinpuku, Y. Kono, S. Kittaka, T. Sakakibara, M. Hagiwara, T. Kawakami, K. Iwase, T. Ono, and Y. Hosokoshi, *"Unconventional S=2 alternating chain realized by a metal-radical hybrid-spin approach"*, Phys. Rev. B **93**, 115145 (2016).

3. H. Mitamura, R. Watanuki, N. Onozaki, Y. Amou, Y. Kono, S. Kittaka, Y. Shimura, I. Yamamoto, K. Suzuki, T. Sakakibara, *"Field-induced phase transitions and magnetoferroelectricity in the perfect triangular lattice antiferromagnet $RbFe(MoO_4)_2$ in a vertical magnetic field"*, J. Magn. Magn. Mater. **400**, 70 (2016).

4. M. Yokoyama, H. Mashiko, R. Otaka, Y. Sakon, K. Fujimura, K. Tenya, A. Kondo, K. Kindo, Y. Ikeda, H. Yoshizawa, Y. Shimizu, Y. Kono, and T. Sakakibara, *"Pauli-limited superconductivity and antiferromagnetism in the heavy-fermion compound $CeCo(In_{1-x}Zn_x)_5$"*, Phys. Rev. B **92**, 184509 (2015).

5. Yukio Yasui, Noriaki Hamachi, Yohei Kono, Shunichiro Kittaka, Toshiro Sakakibara, *"First-order ferromagnetic transition of quantum spin ice system $Yb_2Ti_2O_7$"*, SPIN **05**, 154002 (2015).

6. H. Yamaguchi, H. Miyagai, Y. Kono, S. Kittaka, T. Sakakibara, K. Iwase, T. Ono, T. Shimokawa, Y. Hosokoshi, *"Quantum phase near the saturation field in the S=1/2 frustrated spin ladder"*, Phys. Rev. B **91**, 125104 (2015).

7. Hironori Yamaguchi, Yasuhiro Shinpuku, Tokuro Shimokawa, Kenji Iwase, Toshio Ono, Yohei Kono, Shunichiro Kittaka, Toshiro Sakakibara, Yuko Hosokoshi, *"S=1/2 ferromagnetic-antiferromagnetic alternating Heisenberg chain in a zinc-verdazyl complex"*, Phys. Rev. B **91**, 085117 (2015).

8. Hironori Yamaguchi, Hirotsugu Miyagai, Tokuro Shimokawa, Kenji Iwase, Toshio Ono, Yohei Kono, Naoki Kase, Koji Araki, Shunichiro Kittaka, Toshiro Sakakibara, Takashi Kawakami, Kouichi Okunishi, and Yuko Hosokoshi, *"Fine-Tuning of Magnetic Interactions in Organic Spin Ladders"*, J. Phys. Soc. Jpn. **83**, 033707 (2014).

9. Makoto Yokoyama, Kenji Fujimura, Sara Ishikawa, Masashi Kimura, Takeshi Hasegawa, Ikuto Kawasaki, Kenichi Tenya, Yohei Kono, and Toshiro Sakakibara, *"Possible Evolution of Antiferromagnetism in Zn-Doped Heavy-Fermion Superconductor $CeCoIn_5$"*, J. Phys. Soc. Jpn. **83**, 033706 (2014).

10. Kenji Iwase, Hironori Yamaguchi, Toshio Ono, Yuko Hosokoshi, Tokuro Shimokawa, Yohei Kono, Shunichiro Kittaka, Toshiro Sakakibara, Akira Matsuo, and Koichi Kindo, *"Quasi-one-dimensional S=1/2 Heisenberg antiferromagnetic chain consisting of the organic radical p-Br-V"*, Phys. Rev. B **88** (2013) 184431.

11. H. Yamaguchi, T. Okubo, K. Iwase, T. Ono, Y. Kono, S. Kittaka, T. Sakakibara, A. Matsuo, K. Kindo, and Y. Hosokoshi, *"Various regimes of quantum behavior in an S=1/2 Heisenberg antiferromagnetic chain with fourfold periodicity"*, Phys. Rev. B **88** (2013) 174410.

Acknowledgments

First of all, I am deeply indebted to Prof. T. Sakakibara for his appropriate guidance of experimental techniques, writing techniques of papers, and stimulating discussion of condensed matter physics. I am sure that my dissertation writing would have not been possible without his continuous and warm support for my Ph. D. study.

I am extremely grateful to Prof. M. Takigawa for invaluable discussion and kind support as the chief examiner of my dissertation. I sincerely thank Prof. M. Ogata, Prof. H. Fukuyama, Prof. K. Kindo, and Prof. S. Murakawa as the sub-chief examiners for their insightful comments and suggestions, by which my dissertation can have been refined.

I would like to express my gratitude to all the collaborators of this work. I sincerely thank Prof. Y. Takano (University of Florida) for giving me an opportunity to study the exciting material CuPzN. His advices for the published paper of CuPzN and stimulating discussion of condensed matter physics are invaluable. I would also like to thank Dr. C. P. Aoyama for his support for a part of experimental data of CuPzN. I owe an important debt to Prof. C. P. Landee and Prof. M. M. Turnbull (Clark University) for providing me with single crystals of CuPzN and insightful discussion. I sincerely appreciate the theoretical support and numerical calculations for the study of CuPzN offered by Prof. C. Hotta (the University of Tokyo). I sincerely thank Prof. Y. Hosokoshi and Prof. H. Yamaguchi (Osaka Prefecture University) for providing me with single crystals of 3-Br-4-F-V and 3-I-V. Especially, discussion with Prof. H. Yamaguchi about quantum spin systems has been illuminating. I would also like to thank Prof. H. Tsunetsugu and Prof. M. Oshikawa (ISSP) for valuable discussion about one-dimensional systems.

I would like to offer my special thanks to the members of Sakakibara lab. I sincerely appreciate Dr. H. Mitamura for teaching physics of spin chirality and experimental techniques. I would like to show my greatest appreciation to Dr. S. Kittaka for teaching experimental techniques of specific-heat measurements, writing techniques of papers, and stimulating discussion in many aspects. I sincerely appreciate Ms. Y. Hishinuma for clerical and moral support. I would like to thank Dr. Y. Sun for valuable discussion. I sincerely appreciate Mr. S. Nakamura for useful help and valuable discussion. I would also like to express my gratitude to the former members of Sakakibara lab, Dr. Y. Shimizu, Dr. K. Araki, Dr. N. Kase, Dr. Y. Shimura, Mr. Y. Aoki, and Mr. A. Kasahara for invaluable discussion and useful help in many aspects. Including Prof. M. Yokoyama (Ibaraki University), Prof. Y. Yasui (Meiji University), Dr. H. Takatsu (Kyoto University), and Dr. Y. Matsumoto (Nagoya Institute of Technology), I greatly appreciate many people, who have visited Sakakibara lab for joint research program, for stimulating discussion.

A part of this work was supported by Grants-in-Aid for Scientific Research from the Japan

Society for the Promotion of Science (JSPS). I appreciate JSPS for financially support as a JSPS Research Fellow.

Lastly, I would like to express the deepest appreciation to my parents for giving me an opportunity to study in doctor course.